Silicon Photonic Devices and Their Applications

Ying Li

Submitted in partial fulfillment of the

requirements for the degree of

Doctor of Philosophy

in the Graduate School of Arts and Sciences

COLUMBIA UNIVERSITY

2016

ABSTRACT

Silicon Photonic Devices and Their Applications

Ying Li

Silicon photonics is the study and application of photonic systems, which use silicon as an optical medium. Data is transferred in the systems by optical rays. This technology is seen as the substitutions of electric computer chips in the future and the means to keep tack on the Moore's law.

Cavity optomechanics is a rising field of silicon photonics. It focuses on the interaction between light and mechanical objects. Although it is currently at its early stage of growth, this field has attracted rising attention. Here, we present highly sensitive optical detection of acceleration using an optomechanical accelerometer. The core part of this accelerometer is a slot-type photonic crystal cavity with strong optomechanical interactions. We first discuss theoretically the optomechanical coupling in the air-slot mode-gap photonic crystal cavity. The dispersive coupling g_{om} is numerically calculated. Dynamical parametric oscillations for both cooling and amplification, in the resolved and unresolved sideband limit, are examined numerically, along with the displacement spectral density and cooling rates for the various operating parameters. Experimental results also demonstrated that the cavity has a large

optomechanical coupling rate. The optically induced spring effect, damping and amplification of the mechanical modes are observed with measurements both in air and in vacuum. Then, we propose and demonstrate our optomechanical accelerometer. It can operate with a resolution of 730 ng/$Hz^{1/2}$ (or equivalently 40.1 aN/$Hz^{1/2}$) and with a transduction bandwidth of ≈ 85 kHz.

We also demonstrate an integrated photonics device, an on-chip spectroscopy, in the last part of this thesis. This new type of on-chip microspectrometer is based on the Vernier effect of two cascaded micro-ring cavities. It can measure optical spectrum with a bandwidth of 74nm and a resolution of 0.22 nm in a small footprint of 1.5 mm^2.

Contents

List of Tables

List of Figures

Figure 4.6 | DC acceleration signal detection. a, Backaction RF transduction at 370 μW drive powers under different accelerations, from 6.7 μg to 154.8 μg. Accelerations applied on the device pointing outwards from rotation center. Mechanical RF frequency decreases by 146 Hz. Each curve is offset by 2 dBm along *y*-axis for illustration. The overall fit to the detection sensitivity is at 2.31 μg/Hz. The resolution *R* is determined from $R = 14.5\ \mu g/Hz^{1/2}$, pre-oscillation. **b,** DC accelerometer driven into self-sustained oscillation mode, with optical drive power exceeding the intrinsic mechanical damping, with up to 30th harmonic observed (top panel). Zoom-in of fundamental oscillation mode at 85.3 kHz in this device, with the sidebands arising from coupling to out-of-plane modes. **c,** Tracked RF spectra of oscillation-mode DC acceleration sensing at ≈ 500 μW drive powers. Accelerations applied are from 6.5 μg to 26.3 μg pointing outwards from rotation center, with device mounted with reduction of slot width *s*. Mechanical resonance frequency increases by ≈ 98 Hz. Each curve is offset by 3 dBm along the power spectra for visual clarity. Inset: comparison RF spectra under 6.53, 14.68 and 26.34 μg (from left to right) respectively. **d,** RF resonance of the backaction transduction in oscillation-driven mode under different accelerations. Solid red line is the overall fit of the sensitivity *S* at 196.3 ng/Hz (shaded grey region represents the least-squares regression estimate at 95% confidence interval). The resolution is determined from the frequency noise

Acknowledgements

First of all, I would like to express my gratitude to Professor Keren Bergman and Professor Chee Wei Wong for their support and guidance. I appreciate that Professor Wong believed in me and gave me the chance to work with him when I was still an undergraduate student and was looking for an opportunity to explore his cutting-edge research. I am also grateful that he guided me to the growing and very exciting field of cavity optomechanics right after I joined his group. His enthusiasm and passion for research and education have inspired me greatly.

My deep appreciation also goes to my current advisor, Professor Keren Bergman. I have really enjoyed our work together and interactions since I joined her group. She cares about her students and has provided me with valuable guidance in both my research and my life. I also want to thank her, as well as Professor Jeffrey Kysar and Dean Mary C. Boyce for supporting me in my desire to continue my research at Columbia University when Professor Wong left, and I had to transfer to another research group.

I would also like to acknowledge Professor Kysar and my other committee members, Professor Arvind Narayanaswamy, Professor Qiao Lin and Professor Irving P. Herman for helpful discussions. In addition, I thank Professor Tony Heinz for his wisdom and encouragement at critical times, which made it possible for me to take very important steps in my work. I will never forget that.

All the members of the Optical Nanostructures Laboratory have contributed

significantly to this thesis. I would particularly like to thank Jiangjun Zheng, who taught me the first experiment step by step and kindly shared all his research experiences with me. Jie Gao, Zhenda Xie and James F. McMillan, without any doubt, are great scientists like all of the other member of the lab, and they are always willing to share their knowledge regarding equipments and experiment details. I also have had the pleasure of working closely with Di Wang, Xingsheng Luan, and Yongjun Huang on our optomechanical projects. I also want to thank all the other current and former members of the group for sharing many thoughts with me. Pin-Chun, Tingyi, Serdar, Jing, Shu-Wei, Felice, Mehmet, Charlton, Jinghui, Xinan, Xuesi, Ali, Francesco, Matthew, Demi, Catvu, Jeff, and Andrzej were excellent friends, and I appreciate that a lot.

I would also like to acknowledge all the members of the Lightwave Research Laboratory. I want to thank all the inspiring discussions with and warm help from Qi, Lee, Christine, and Cathy. I have been very lucky to work with these very talented and motivated people.

I greatly enjoyed the collaboration between our group and many other groups both inside and outside of Columbia. They were certainly critical for the completion of this thesis. I want to thank Luozhou, Xinwen, and Xuetao from Professor Dirk Englund's group and the administrative staff: Rebecca, Sandra. I want to acknowledge Dr. Ming Lv from Brookhaven International Lab for training me in nanofabrication skills. I also want to give my appreciation to Yang from Coriant Advanced Technology Group for the collaboration and discussion on the on-chip OSA project.

Finally, I would like to thank my family and my friends. My parents have devoted their lives to the education of their only child, and I feel extremely lucky to be that person. They never planned out a future for me but instead have always loved, encouraged, and supported me at every moment in my life. I also would like to thank all my friends for all the enjoyable time we spent together. Life would be less colorful and meaningful without you.

Chapter 1

Introduction

1.1 A Brief Introduction of Cavity Optomechanics

Optomechanics is the optical and mechanical degree of freedom coupling via optical radiation or gradient force. The idea of cavity optomechanics can be explained by using a Fabry-Perot cavity with one of its mirrors attached to a spring. The cavity supports many optical modes with frequencies down to the fundamental mode of frequency $\nu_0 = c/2L$, where L is the length of the cavity. For a displacement of one of the mirrors, δx, the frequency of the optical mode will shift by $\nu_0 \delta x/L = \delta\nu_0$. This is the essence of optomechanical coupling: a mechanical displacement of the cavity induces a change in the state of the light [1-4].

One of the factors that drives the rapidly growing interests in cavity optomechanics is the highly sensitive optical detection of small forces, displacements, masses and accelerations. In order to realize the highly sensitive detection, people need to make a very small system that can manage to maintain high quality optical and mechanical resonances [5]. The photonic crystal cavity is one of such systems. They have unique advantageous to do optomechanical coupling from their strong light confinement and enhanced light-matter interaction [6-10]. Previous studies have demonstrated that the slot-type photonics crystal cavities have high quality optical factors in small mode volumes [11].

1.2 Thesis organization

One of the most important applications of cavity optomechanics, the high precision sensing has been demonstrated. The design is based on the high optical quality factor and small mode volume photonics crystal cavities. The optomechanical coupling in the cavities has been analyzed in terms of theory, numerical simulations and experimental characterization in this thesis. An on-chip high performance optical spectrum analyzer has also been demonstrated in the last part of the thesis.

In Chapter 2, the strong optomechanical dynamical interactions in ultrahigh-Q/V slot-type photonic crystal cavities are described. The dispersive coupling is based on the mode-gap photonic crystal cavities with light localization in an air mode with $0.02(\lambda/n)^3$ mode volumes while preserving optical cavity Q up to 5×10^6. The mechanical mode is modeled to have fundamental resonance $\Omega_m/2\pi$ of 460 MHz. For this slot-type optomechanical cavity, the dispersive coupling g_{om} is numerically computed at up to 940 GHz/nm (L_{om} of 202 nm) for the fundamental optomechanical mode. Dynamical parametric oscillations for both cooling and amplification, in the resolved and unresolved sideband limit, are examined numerically, along with the displacement spectral density and cooling rates for the various operating parameters.

In Chapter 3, the optomechanical properties of fabricated samples are experimentally demonstrated. With a large optomechanical coupling rate, the optical induced spring effect, damping and amplification of the mechanical modes are observed with measurements in air. Behaviors above the parametric instability threshold are shown. The phase noise of the optomechanical oscillator is analyzed.

In Chapter 4, we demonstrate the optomechanical accelerometer with DC

resolution at 730 ng/Hz$^{1/2}$ (or equivalently 40.1 aN/Hz$^{1/2}$), with a transduction bandwidth of ≈ 85 kHz. Driven into the optomechanical sustained-oscillation mode, the slot photonic crystal cavity provides a radio-frequency (RF) readout of the optically-driven transduction with an enhanced sensitivity of 196 ng per Hz of RF shift. Measuring the optomechanically-stiffened oscillation, instead of optical transmission shift, provides a 125.1× resolution enhancement over pre-oscillation mode detection due to strong optomechanical transduction and readout in the optical domain. This DC acceleration measurements operate at the thermal limit and 3.7× the quantum backaction noise, with a 23.5 dB dynamic range, supported by our theory and numerical modeling.

In Chapter 5, a high resolution, broadband on-chip optical spectrum analyzer (OSA) based on two cascaded tunable ring resonators is demonstrated. Heaters are integrated with the rings and used to continuously tune the resonances. The measured spectral response of the spectrometer shows a resolution of 0.22 nm over an operating bandwidth of 70 nm around 1550 nm center wavelength. The footprint of the spectrometer is less than 1.5 mm^2. The device is integrated on silicon on insulator (SOI) substrate together with a Germanium photodetector and traveling-wave Mach-Zehnder modulator. By using the on-chip modulator and a lock-in amplifier to extract the signal from noise, the power sensitivity of the device reaches -31.2 dBm. The dynamic range of the spectrometer is -31.7 dB at 1.0 nm.

Finally in Chapter 6, we discuss how these optomechanical devices can be useful for mass sensing and other technological applications.

1.3 Publications

The key results from thesis have been published in the following papers;

- Y. Li, D. Wang, N. Goldberg, J. Zheng, M. Lu, L. Churchill, M. Kutzer, D. Rogers, and C. W. Wong, A chip-scale optomechanical DC accelerometer, under review (2015)
- Y. Li+, J. Zheng+, M. S. Area, Aaron Stain, Ken L. Shepard, and C.W.Wong, Parametric optomechanical oscillations in 2D slot-type high-Q photonic crystal cavities, Appl. Phys. Lett. 100, 211908 (2012)
- Y. Li, J. Zheng, J. Gao, J. Shu, M. S. Aras, and C. W. Wong, Design of dispersive optomechanical coupling and cooling in ultrahigh-Q/V slot-type photonic crystal cavities, Optics Express 18, 23844 (2010).
- Y. Li, Yang Liu, Qi Li, Tom Baehr-Jones, Michael Hochberg and Keren Bergman, A broadband on-chip OSA based on the Vernier effect of dual ring resonators, in preparation

Bibliography

[1] F. Marquardt and S. M. Girvin, Optomechanics, *Physics* 2, 40 (2009).

[2] T. J. Kippenberg and K. J. Vahala, Cavity Opto-Mechanics, *Opt. Express* 15, 17172 (2007).

[3] T. J. Kippenberg and K. J. Vahala, Cavity Optomechanics: Back-Action at the Mesoscale, *Science* 321, 1172 (2008).

[4] D. Van Thourhout and J. Roels, Optomechanical device actuation through the optical gradient force, *Nature Photonics* 4, 211 (2010).

[5] I. Favero and K. Karrai, Optomechanics of deformable optical cavities, *Nature Photonics* 3, 201 (2009).

[6] T. Yoshie, A. Scherer, J. Hendrickson, G. Khitrova, H. M. Gibbs, G. Rupper, C. Ell, O. B. Shchekin, and D. G. Deppe, Vacuum Rabi splitting with a single quantum dot in a photonic crystal nanocavity, *Nature* 432, 200 (2004).

[7] O. Painter, R. K. Lee, A. Scherer, A. Yariv, J. D. O'Brien, P. D. Dapkus, I. Kim, Two-dimensional photonic band-gap defect mode laser, *Science* 284,1819 (1999).

[8] S. Noda, A. Chutinan and M. Imada, Trapping and emission of photons by a single defect in a photonic bandgap structure, *Nature* 407, 608 (2000).

[9] T. Baba, Photonic crystals: Remember the light, *Nature Photonics* 1, 11 (2006).

[10] T. Tanabe, M. Notomi, E. Kuramochi, A. Shinya, and H. Taniyama, Trapping and delaying photons for one nanosecond in an ultrasmall high-Q photoniccrystal nanocavity, *Nature Photonics* 1, 49 (2007).

[11] J. Gao, J. F. McMillan, M.-C. Wu, J. Zheng, S. Assefa, and C. W. Wong,

Demonstration of an air-slot mode-gap confined photonic crystal slab nanocavity with ultrasmall mode volumes, *Appl. Phys. Lett.* 96, 051123 (2010).

Chapter 2

Design of optomechanical coupling in slot-type photonic crystal cavities

2.1 Introduction

The basis of cavity optomechanics is the radiation pressure forces, which rises from the momentum of light. The first study of radiation pressure forces can be traced back to the 17th century. Kepler first postulated the radiation pressure forces from his observation of comets when he noted that the dust tails of the comets pointing away from the sun during a comet transit [1]. About 250 years later, Maxwell's theory of electromagnetic radiation put this conjecture on solid theoretical grounds. However, the first experimental demonstrations of the radiation pressure force that in agreement with Maxwell's predictions were not observed until the beginning of the 20th century. The experiments were carried out by Lebedew in Russia [2] and Nichols and Hull in the United States [3]. In 1909, Einstein derived the statistics of the radiation pressure force fluctuation acting on a moveable mirror [4].

One of an extraordinarily critical technique realized by using the radiation pressure force is laser cooling. Hansch and Schawlow [5] and Dehmelt and Wineland [6] first pointed out the non-conservative nature of the radiation pressure force in 1975. Arthur Ashkin later demonstrated that focused lasers beams could be used to trap and control dielectric particles [7, 8]. Then, laser cooling arose great interests and gradually became an important technique [9]. Many applications has also been enabled by laser cooling, from optical atomic clocks, precision measurements of the gravitational field to systematic studies of quantum many-body physics in trapped clouds of atoms [10, 11].

Also in the 1970s, Braginsky and his team started to investigate the ability of radiation force of cooling larger objects. One of the initial efforts examines macroscopic movable mirrors in the Laser Interferometer Gravitational Wave Observatory (LIGO) project [12-13]. After that, people started to explore theories of quantum cavity optomehcanical system in the 1990s [14-16]. Experimental demonstrations of optomechanical coupling were reported in the new century. Several classes of cavity optomechanical systems have been explored. Based on the micro- and nano-fabrication techniques, optomechanical resonators such as mirror coated AFM-cantilevers [17], movable micromirrors [18-19], vibrating microtoroids [20-21], and nano-membranes [22-23] have been examined recently. Nowadays, the field of cavity optomechanics develops very fast [24-28]. Recent studies cover a vast span of applications [17-20, 29-41]. In addition to the radiation-pressure dynamic backaction, another class of optomechanical devices, such as photonic crystal cavities, utilizes optical gradient forces [42-47] based on near-field effects. Compared to radiation-pressure based optomechanical cavities, these devices can achieve wavelength-scale effective optomechanical coupling lengths due to the strong transverse evanescent-field coupling between the adjacent cavity elements [32, 38, 39, 42, 43, 47].

Photonic crystal membranes can be a very good candidate platform with great design flexibility [48-43], with photonic crystal cavities offering an ultrahigh optical quality factor with a small volume [54-56]. The internal optical intensity is very high and sensitive to the geometrical changes. However, to make these cavities support

mechanical cavity modes with strong coupling with the optical modes, special design considerations are needed. Current reported geometries are either in-plane in side-by-side configuration [57-58] or vertically superimposed in face-to-face configuration [59]. Both configurations are recently examined experimentally to be promising for cavity optomechanical applications.

In this chapter, we theoretically investigate the large dispersive optomechanical coupling between the mechanical and optical modes of a tuned air-slot mode-gap photonic crystal cavity [60]. First, the optical modes are shown to exhibit high optical quality factor (Q) with ultra-small mode volumes (V) [61-65], from three-dimensional finite-difference time-domain (FDTD) numerical simulations. The mechanical modes and properties are then modeled using finite element methods. Based on first-order perturbation theory [66-67] and parity considerations, the respective optomechanical modes are then examined numerically. The dynamical backaction of slot-type photonic crystal cavities is studied, including the optically-induced stiffening, optical cooling and amplification, and radio-frequency spectral densities, for various laser-cavity detuning, pump powers and other operating parameters. We also note that the slot-type photonic crystal cavity can operate in the resolved-sideband limit, which makes it possible to cool the mechanical motion to its quantum mechanical ground state.

2.2 Optical design of slot-type photonic crystal

We have taken our initial parameters from our previous study [24] and varied t, r. The slot-type optomechanical cavity is based on the air-slot mode-gap optical cavities

recently demonstrated experimentally for gradual width-modulated mode-gap cavities [60] or heterostructure lattices [45], and theoretical proposed earlier in Ref. [56]. A non-terminated air-slot [64] is added to width-modulate line-defect photonic crystal cavities to create ultrasmall mode volume cavities. To better understand the various modes existing in the air-slot mode-gap cavities, the modes in the slotted photonic crystal waveguide with W1 line-defect width and their dispersion properties are first investigated and shown in Fig. 2.1(a) for the three localized waveguide modes. Mode I and II can be traced back to the W1 waveguide fundamental even mode and high-order odd mode respectively inside the photonic band gap, while mode III can be understood as arising from the second index-guided mode (as shown in Ref. [68]) below the projected bulk modes. We produce the cavities by locally shifting the air holes away from the center of waveguide – thus the cavity mode resonances are created below the transmission band of the slotted waveguide. Two of the possible modes in the cavities are shown in Fig. 2.1(b). Confirmed from the mode frequency and symmetry, cavity mode I is due to the mode gap of slotted waveguide mode I [Fig. 2.1(b)] and is expected to have both high Q and sub-wavelength V. Cavity mode II [Fig. 2.1(c)] represents the mode with the same odd symmetry as mode II in slotted waveguide.

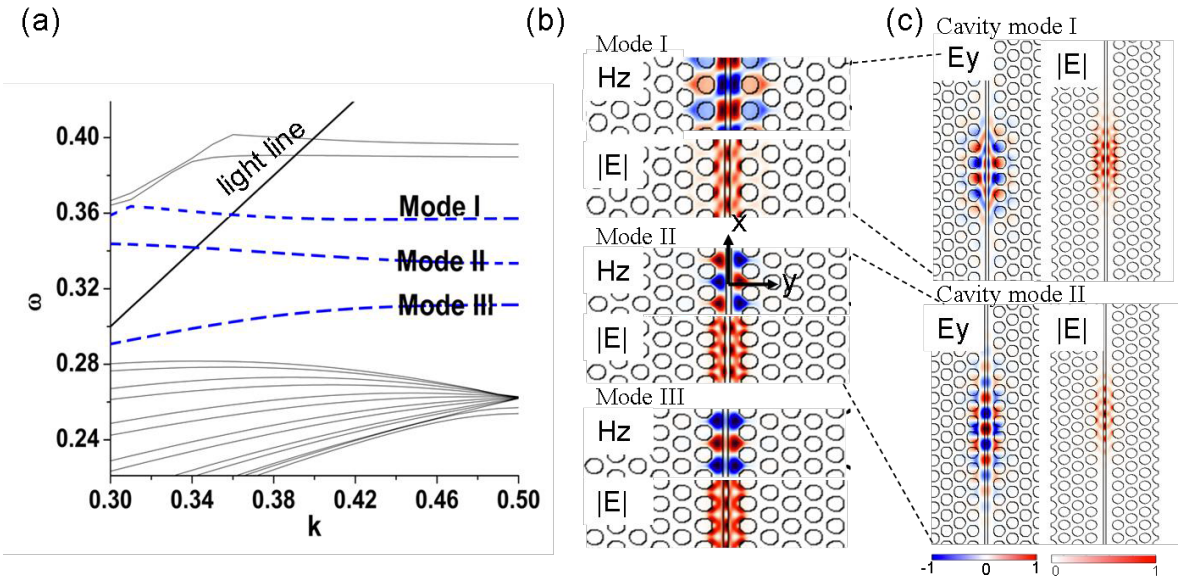

Figure 2.1 | Band diagram and optical field of the photonic crystal cavity. a, Photonic band structure of slotted PhCWG with s = 80 nm. The blue lines show the three modes in the slotted PhCWG. **b**, *H*-field and energy distribution of waveguide modes I, II and III. **c**, *E*-field and energy distribution of the first (above) and the second (below) cavity modes.

A scanning electron micrograph (SEM) image of the cavity is illustrated in Fig. 2.2(a) with a = 490 nm, r = 0.34a, t = 0.449a, n_{si} = 3.48, s = 80 nm, d_A = 0.0286a, d_B = 0.019a and d_C = 0.0095a. FDTD simulation is performed to numerically evaluate the properties of the cavity mode. Fig. 2.2(b) shows the measured radiation spectrum of the cavity. For s = 80 nm, the air-slot mode-gap confined PCS photonic crystal nanocavity supports a high Q localized even mode [Fig. 2.1(c)] with Q factor up to 5×10^5 and a mode volume V of 0.02 $(\lambda/n_{air})^3$ from numerical simulations [56, 60]. 2D Fourier transform of the electric field shows few leaky components inside the light cone, supporting the high Q character of this air-confined mode. From Fig. 2.1(c), the optical field is mainly distributed in cavity region, and the simulation results also show that the minimum number of lateral lattice rows next to the cavity to maintain the high Q is ~ three lateral lattice rows. We therefore designed each beam into three lines with eight holes in each line, l = 8a.

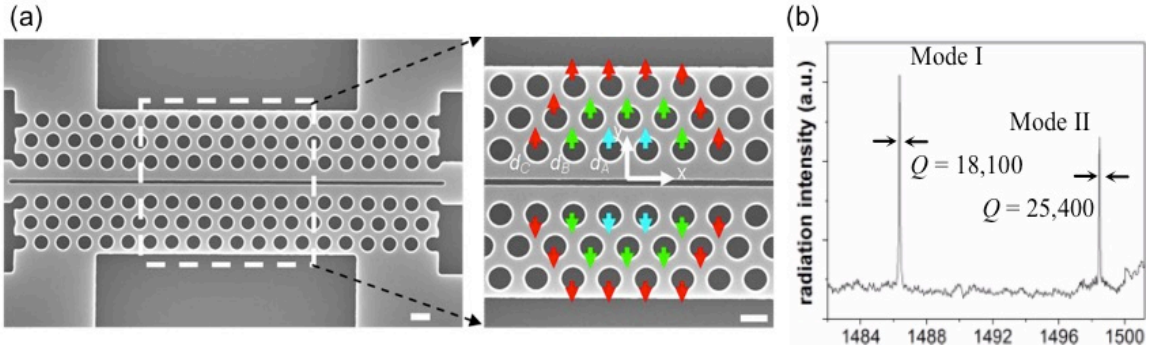

Figure 2.2 | SEM images and optical modes. a, Example SEMs of the air-slot mode-gap optomechanical cavity. The holes shifts are shown in the right panel with d_A = 0.0286a (red), d_B = 0.019a (blue) and d_C = 0.0095a (green), where a is the crystal lattice constant, for increasing the intrinsic cavity Q. Scale bar: 400 nm. **b**, Measured cavity radiation for the first two optical modes, with loaded Q at 25,400 for the second mode and 18,100 for the first mode respectively.

2.3 Mechanical design

The mechanical modes are examined numerically via finite-element-method (FEM) simulations (COMSOL Multiphysics) for the dynamical motion of the suspended beams. The cavity mechanical modes can be categorized into common and differential modes of in-plane and out-of-plane motion [57] as well as compression and twisting modes of the two beams. The displacement fields *Q(r)* of the first eight mechanical modes are shown in Fig. 2.3. In the numerical simulations, the beams are clamped at both ends using fixed boundary conditions at the two ends (x = ±1.96 um) of the beam, meanwhile limiting motion in the x-y plane (in boundary condition constraint of z = ±110 nm has a standard notion displacement in R_z = 0 nm and R_x = 0 nm, where R_z (R_x) is the deformation along z(x) axis), with silicon material properties: Young's modulus E of 130 GPa normal to [110] silicon crystallographic in-plane direction, thermal expansion coefficient α of 4.15×10^{-6} K, specific heat capacity c of 703 J/(kg·K), thermal conductivity κ of 156 W/(m·K) and density ρ of 2330 kg/m^3. We choose the triangular mesh configuration, with an average mesh element volume of ~ 9×10^{-4} μm^3, with the eigenfrequency and modal analysis for the first eight mechanical modes [Fig. 2.3], with eigenfrequencies ranging from 460 MHz to 2.16 GHz. Only mechanical modes with parity p_x, = p_y = p_z = +1 can coupled to the optical slot cavity modes due to the symmetry of the optical field, as described in Ref. [52]. Among the first eight mechanical modes, five of them (illustrated in grayscale in Fig. 2.3) do not couple to the optical modes due to parity

considerations – *b* and *f* do not have the right parity in the *x* direction while *d*, *e* and *g* modes cannot be excited because of asymmetry of the optical gradient force along the *y* direction. In this slot cavity, therefore, only the first, third and eighth mechanical modes (depicted in color) have strong dispersive coupling to the localized optical modes. These are in-plane differential modes with modal frequencies $\Omega_m/2\pi$ at 459 MHz, 1.36 GHz and 2.16 GHz respectively for a suspended beam length *L* of 3.92 um. The effective mass of each mode is computed from $m_{eff} = \int dV \frac{(r - r_0)^2}{(r - r_0)_m^2} \rho$, integrated over the computational space with ρ defined as the mass density, *r* the position from a fixed origin r_0 and $(r - r_0)_m$ defined as the maximum displacement. The effective mass of the first, third, and eighth mechanical modes are computed to be 2 pg, 1 pg, and 0.3 pg respectively in our specific implementation with 3.92 um beam length, width of 1.7 um, and membrane thickness of 220 nm.

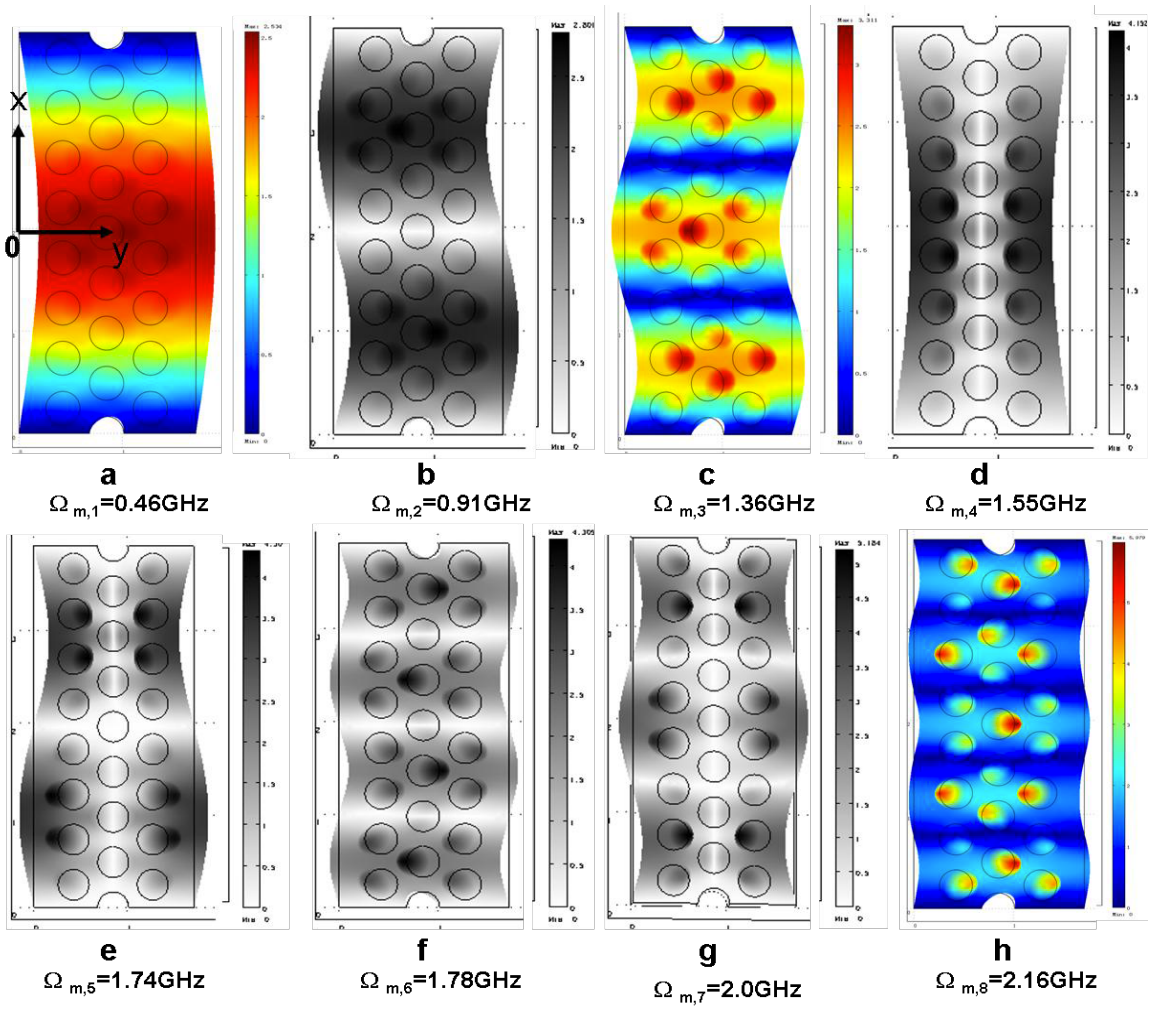

Figure 2.3 | Example Mechanical displacement profile of the first eight mechanical modes. Modes in color (*a*, *c*, *h*) are allowed by parity considerations to couple to the optical modes; modes in grayscale (*b*, *d*, *e*, *f*, *g*) are forbidden by parity for sizable optomechanical coupling. Red (blue) denotes maximum (minimum) displacement and plotted on a linear scale.

There are a number of possible dissipative processes where mechanical vibrational energy is dissipated into heat, either inside the structure or via interaction with its surroundings. These processes include squeezed film damping due to air viscosity [69], clamping losses which are due to the radiation of elastic waves into the substrate through the supports of the oscillator [70], internal viscous damping in the silicon structure, and thermoelastic damping [71]. Thermoelastic losses often set a lower ballpark estimate of the attainable Q_m in a vibrating beam element, where $Q_{m,Zener}$ of the fundamental mechanical mode is expressed by [72, 73]: $Q_{m,Zener} = \frac{c\rho}{E\alpha^2 T_R}\frac{1+(\omega\tau_z)^2}{\omega\tau_z}$, where T_R is the ambient reservoir temperature, τ_z is the thermal relaxation time defined by $\frac{b^2}{\pi^2\chi}$, $\chi = \frac{\kappa}{c\rho}$, and b is the width of the beam. With silicon material properties, T_R at 300 K, and b at 1.7 μm, Q_m is found to be in the range of 12,000 for the fundamental mode, and 40,000 and 60,000 for the third and eighth mechanical modes respectively.

2.4 Optomechanical properties

Cavity optomechanics involves the mutual coupling of two modes in the same spatially co-located oscillator: one optical (characterized by its optical eigenfrequency and electromagnetic fields) and one mechanical (characterized by its mechanical eigenfrequency and displacement fields) degrees-of freedom. The perturbed cavity optical resonance, modified by small displacement about equilibrium displacement α,

can be given by its Taylor expansion around $\omega_o(\alpha)$. If we consider the first-order expansion, and also set $\omega_0(\alpha) = \omega_0\big|_{\alpha=a_0}$ as the equilibrium resonance of the optical mode, then the first order $g_{om} = d\omega_o/d\alpha$ can be defined as optomechanical coupling rate. g_{om} also represents the differential frequency shift of the cavity resonance (ω_o) with mechanical displacement (α) of the slot cavity beams. One can parameterize the interaction strength between optical and mechanical degrees-of-freedom by an effective coupling length L_{om} [51] described by: $L_{om}^{-1} = \frac{1}{\omega}\frac{d\omega}{d\alpha}$, with a corresponding optomechanical coupling frequency g_{om} defined by $g_{om} \equiv \omega_o/L_{om}$.

2.4.1 Perturbation theory

Perturbation theory for Maxwell's equations with shifting material boundaries was used to calculate the coupling length L_{om} [66, 67]. With the parameter $\Delta\alpha$ characterizing the perturbation, the Hellman-Feynman theorem [74] provides an exact expression for the derivative of ω in the limit of infinitesimal $\Delta\alpha$, $\frac{d\omega}{d\alpha} = -\frac{\omega^{(0)}}{2}\frac{\left\langle E^{(0)}\left|\frac{d\varepsilon}{d\alpha}\right|E^{(0)}\right\rangle}{\left\langle E^{(0)}|\varepsilon|E^{(0)}\right\rangle}$, where the terms with the (0) superscripts denote the unperturbed terms. With shifting material boundaries, the discontinuities in the E-field or the eigenoperator are overcome with anisotropic smoothening which gives the following expression for the integral in the numerator [66], $\left\langle E^{(0)}\left|\frac{d\varepsilon}{d\alpha}\right|E^{(0)}\right\rangle = \int dA \frac{dh}{d\alpha}\left[\Delta\varepsilon_{12}\left|E_{\parallel}^{(0)}\right|^2 - \Delta(\varepsilon_{12}^{-1})\left|D_{\perp}^{(0)}\right|^2\right]$, for first-order

perturbation of the cavity resonance. The integral is performed across the entire boundary surfaces of the optomechanical cavity, with *h* the displacement perpendicular to the unperturbed boundary surface. $\Delta\varepsilon_{12}$ is defined as (ε_1 - ε_2) and $\Delta\left(\varepsilon_{12}^{-1}\right)$ is defined as $\left(\varepsilon_1^{-1}-\varepsilon_2^{-1}\right)$. $\left|E_{\parallel}^{(0)}\right|^2$ is the unperturbed *E*-field parallel to the boundary surface while $\left|D_{\perp}^{(0)}\right|^2$ is the unperturbed electric displacement *D* normal to the boundary surface. From Ref. [52], one defines $Q(r)=\alpha q(r)$, where α is the largest displacement amplitude that occurs anywhere for the displacement field $Q(r)$. From the perturbative formulation, one then obtains: $L_{OM}^{-1}=\frac{1}{2}\frac{\int dA\left(q(r)\cdot\hat{n}\right)\left[\Delta\varepsilon_{12}(r)\left|E_{\parallel}^{(0)}\right|^2-\Delta\left(\varepsilon_{12}^{-1}(r)\right)\left|D_{\perp}^{(0)}(r)\right|^2\right]}{\int dV_{\varepsilon}(r)\left|E(r)\right|^2}$, where $\hat{n}$ is the unit normal vector at the surface of the unperturbed cavity and the spatial *r*-dependence explicitly shown here.

2.4.2 Optomechanical coupling in slot-type optical cavities

Fig. 2.4 shows the computed optomechanical coupling in the slot-type mode gap cavities, from first-order perturbation theory. As noted from parity consideration, here we show the optomechanical coupling strengths for the first optical mode to the *allowed* first ($\Omega_{m,1}$) and second ($\Omega_{m,3}$) mechanical modes, denoted as $g_{om}(O_1\text{-}M_1)$ and $g_{om}(O_1\text{-}M_2)$ respectively. We illustrate the coupling strengths for different slot gaps *s* of cavity, ranging from 40 nm to 200 nm. The electromagnetic field used is within a slot length $l = 8a$, since the cavity is confined by the PhCWG mode gap to a spatial localization of only several lattice constants *a*. As shown in Fig. 2.4, when the first optical mode is coupled

with the second mechanical mode, the g_{om} is lower than that with the fundamental mechanical mode, which means the fundamental optical and mechanical modes provide the strongest dispersive coupling. The negative values depict as a decrease in optical resonance frequency for increasing slot widths s. For the fundamental mode, the dispersive coupling can go up to 940 GHz/nm (or a coupling length of 202 nm) for a slot width of 40 nm. These strong optomechanical coupling is more than an order of magnitude larger than in earlier optomechanical implementations. We also note that, since the electromagnetic field is negligible outside the cavity region of $l = 8a$, the coupling length does not change much when l is longer than $8a$.

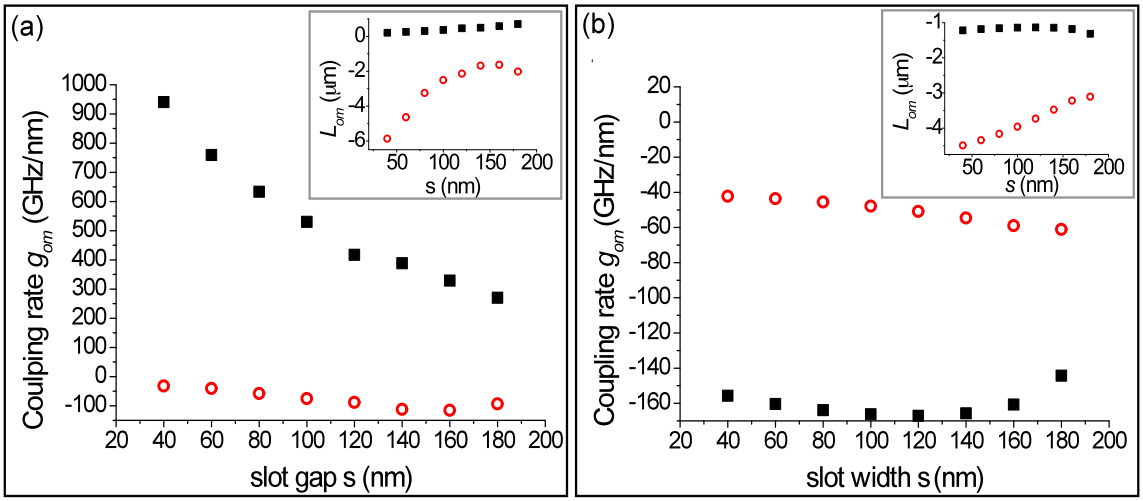

Figure 2.4 | Coupling rate of the slot cavity. a, Computed optomechanical coupling rates of the fundamental optical mode with first (black solid squares) and second (red open circles) *allowed* mechanical modes, computed for the different slot gaps *s*. The inset panel is the corresponding coupling length. **b**, Computed optomechanical coupling rates of the second optical mode coupled with first (black solid squares) and second (red open circles) *allowed* mechanical modes.

2.5 Coupled mode theory

The coupled equations of motion for the optical and mechanical modes can be derived from a single Hamiltonian [64, 8]: $\frac{da}{dt} = i\Delta(x)a - \left(\frac{1}{2\tau_0} + \frac{1}{2\tau_{ex}}\right)a + i\sqrt{\frac{1}{\tau_{ex}}}s$ and $\frac{d^2x}{dt^2} + \frac{\Omega_m}{2Q_m}\frac{dx}{dt} + \Omega_m^2 x = \frac{F_{OM}(t)}{m_{eff}} + \frac{F_L(t)}{m_{eff}} = -\frac{g_{OM}}{\omega_0}\frac{|a|^2}{m_{eff}} + \frac{F_L(t)}{m_{eff}}$, where $|a|^2$ is the stored cavity energy, $|s|^2$ the launched input power into the cavity, with a cavity decay rate κ of $\frac{1}{2\tau} = \frac{1}{2\tau_0} + \frac{1}{2\tau_{ex}}$, with intrinsic rate $1/\tau_o$ and coupling rate $1/\tau_{ex}$. $\Delta(x) = \omega - \omega_0(x)$ is the pump laser frequency ω detuning with respect to the cavity resonance $\omega_o(x)$ with explicitly displacement x shown. In this case, we have $\Delta(x) = \Delta - g_{OM}x$. $F_L(t)$ is the thermal Langevin force. We illustrate the time-domain displacement $x(t)$ and the normalized cavity amplitude of the first optical and first mechanical modes in Fig. 2.5(a). The cavity amplitude oscillates in-phase with the displacement within the mechanical frequency cycle as shown. The sub peaks of the cavity amplitude a come from the overlap of the first and second harmonic modes. In Fig. 2.5(b) we show the optical cavity amplitude transduction for different normalized detunings ($\Delta\tau$ = -1, -0.25, 0, 0.25, 1). At zero detuning and with a launched power $|s|^2$ into the cavity, the cavity amplitude oscillates with a single-period cycle at the fundamental mechanical mode frequency, as indication of mixing of the optomechanical domains. At detunings $\Delta\tau$ = ±0.25, a two-period cycle with a second amplitude maxima is distinctly observed, with

inverted transmission between the blue and red detunings. At larger detunings (such as $\Delta\tau = \pm 1$), a two-period cycle is still observed, although the second amplitude maxima are suppressed.

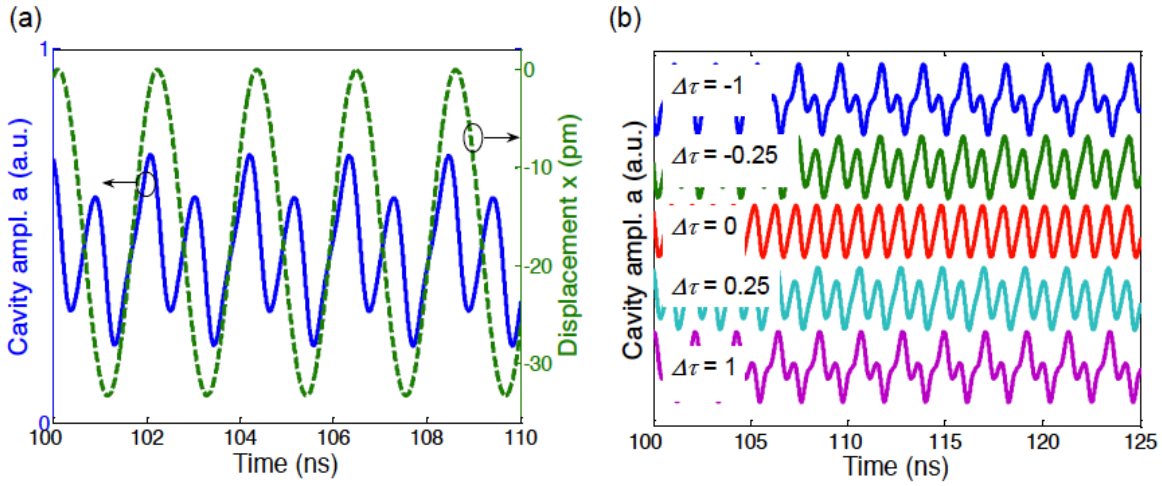

Figure 2.5 | Time-domain cavity amplitude from coupled equations. a, Time-domain cavity amplitude a (solid blue line) and displacement x (dashed green line) of the first optical and first mechanical modes, with g_{om} of 940 GHz/nm, $\Omega_m/2\pi$ of 470 MHz, Q_m of 12,400, $\kappa/2\pi$ of 425 GHz, and $(1/\tau_{ex})/2\pi$ of 38 MHz. **b**, Time-domain cavity amplitude for normalized detunings $\Delta\tau$ at -1, -0.25, 0, 0.25 and 1 (top to bottom).

2.6 Displacement spectral density

2.6.1 Optically-induced stiffening and effective damping rate

From the coupled equations, the *x*-dependent contribution to this adiabatic response provides an optical contribution to the stiffness of the spring-mass system. The corresponding change in spring constant leads to a frequency shift relative to the unperturbed mechanical oscillator eigenfrequency, or termed as optically-induced stiffening [13, 57]. The non-adiabatic contribution in coupled equations is proportional to the velocity of the spring-mass system. The optical gradient force induced damping rate modifies the intrinsic mechanical resonator loss rate Γ_m, yielding an effective damping rate: $\Gamma_{eff} = \Gamma + \Gamma_m$, where

$$\Gamma = -\frac{\omega_0}{2\Omega L_{om}^2 m_{eff}}\left(\frac{2\kappa_{ex}}{\kappa^2 + 4\Delta^2}\right)\left[\frac{\kappa/2}{(\Delta - \Omega_m)^2 + (\kappa/2)^2} - \frac{\kappa/2}{(\Delta - \Omega_m)^2 + (\kappa/2)^2}\right]p.$$ We note that this is valid only in the weak retardation regime in which $\kappa >> \Omega_m$. We illustrate in Fig. 2.5 the corresponding frequency shifts and effective damping rate of the slot-type mode-gap cavity, for different input powers and normalized detuning ($\Delta\tau$). With this classical model, the laser introduces a damping without introducing a modified Langevin force. This is a key feature and allows the enhanced damping to reduce the mechanical oscillator temperature, yielding as a final effective temperature T_{eff} for the mechanical mode under consideration: $T_{eff} \cong \frac{\Gamma_m}{\Gamma_{eff}} T_R$. As shown in Fig. 2.5, as optical Q increases, at certain detuning the frequency shift becomes larger and the effective temperature is

lowered, denoting the increased cooling rate. For a fixed optical Q in the unresolved sideband limit, there will be an optimal detuning where the linewidth reaches its largest value and the effective temperature is the lowest. In our case this optimal detuning $\Delta\tau$ is around -0.25 with an input power of 50 pW and the effective temperature can be lower than 50 K.

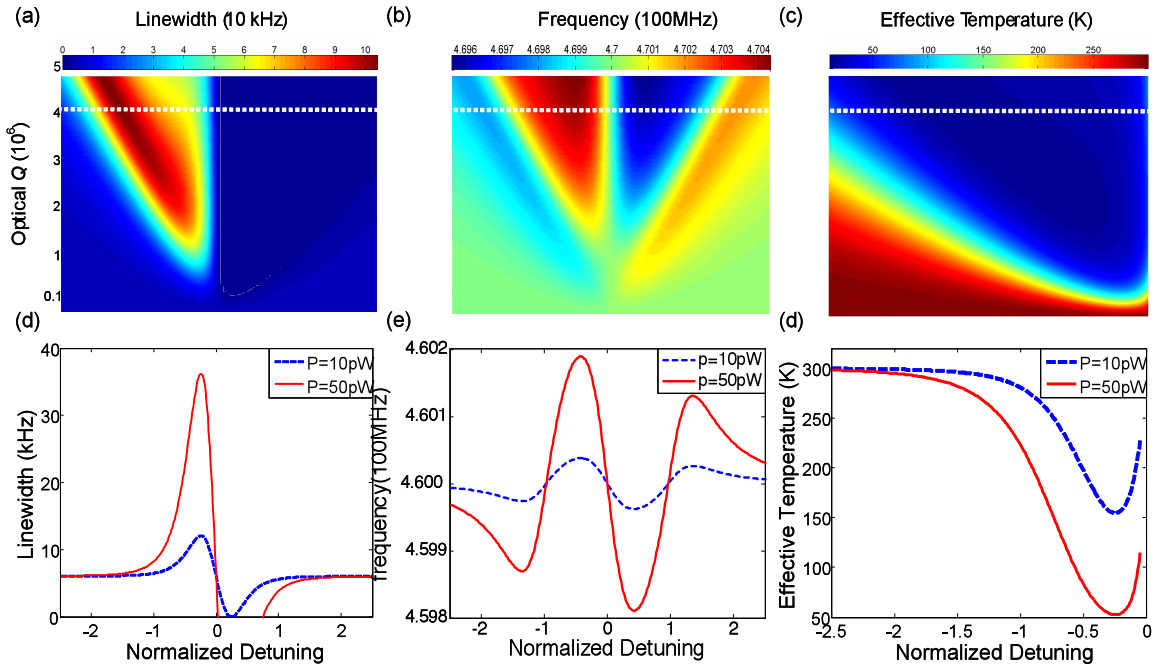

Figure 2.6 | Optomechanical cooling and heating effect. a-c, Two-dimensional surface plots of the first optical – first mechanical mode linewidth **a**, mechanical frequency **b**, and effective temperature **c**, for varying detunings and optical Q factors. A fixed pump power of 1 pW is used, along with an effective mass of 200 fg and a 300 K bath temperature. The dashed white line denotes the condition for $\Omega_m = \kappa$. d-f, Example first optical – first mechanical mode linewidths (**d**), frequency shift (**e**) and effective temperature (**f**) with two input powers (P) and varying laser-cavity detuning. Otherwise indicated, the conditions are identical to panel (a), and with optical Q chosen at 5×10^5.

2.6.2 Spectral intensity

The spectral intensity of purely mechanical displacement in the oscillator is described as: $S_x(\Omega) = \frac{2\Gamma_m k_B T / m_x}{\left(\Omega_m^2 - \Omega^2\right)^2 + \left(\Omega\Gamma_m\right)^2}$, without the optical stiffening and damping. Since the coupling will shift the oscillator frequency and damping, we can modify Ω_m and Γ_m in the expression into $\Omega_m^{'} = \Omega_m + \Delta\Omega_m$ and $\Gamma_m^{'} = \Gamma + \Gamma_m$. Fig. 2.7(a) shows the resulting displacement spectral density when the input power *P* changes from 0 to 6.9uW, and normalized detuning $\Delta\tau$ = -0.25 where the linewidth has the maximum value and the frequency shift is positive. With increasing input power, the peak value of the displacement spectral density goes down and the full-width at half-maximum becomes larger, which demonstrates an effective cooled temperature of the slot-type optomechanical oscillator. In Fig. 2.7(b) we show the optical stiffing and linewidth damping of the first two mechanical modes, for a span of detunings while maintaining a fixed input power. Note that the optical stiffening is not monotonic with increasing detuning. For a cavity decay $\kappa/2\pi$ of 387 MHz, the optimal detuning is at $\Delta\tau$ of -0.43, for the largest optical gradient force stiffening. For the second allowed mode, in the region of normalized detuning from zero to -4, this stiffening is large which leads to a significantly suppressed spectral density. Moreover, note that in both Fig. 2.7(a) and 2.7(b), a large optical stiffening can be observed in the slot-type optomechanical cavity, where the optical stiffening can result in a modified mechanical frequency more than 1.86× the bare mechanical frequency.

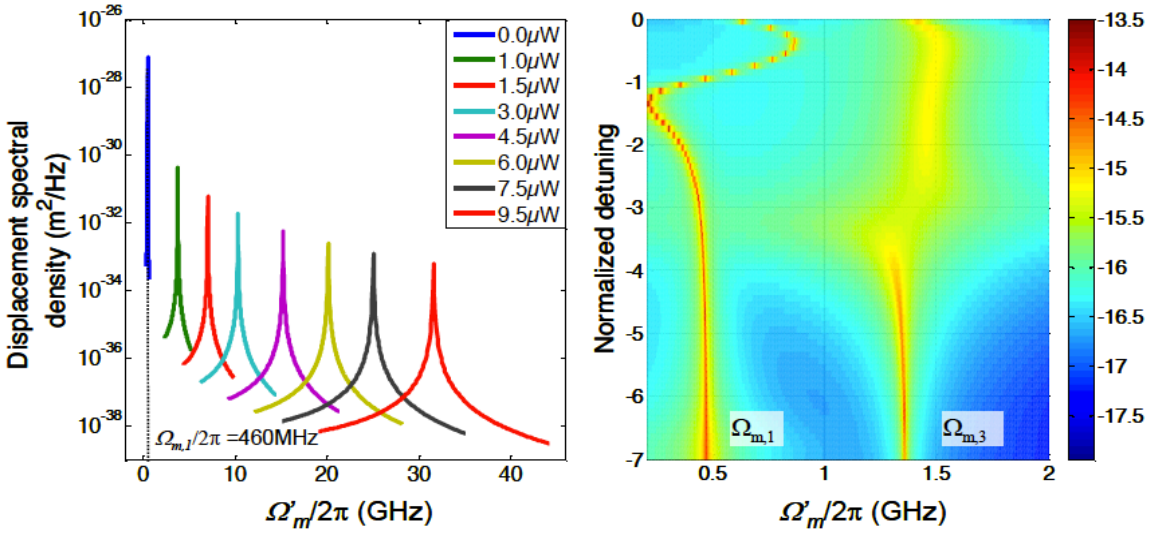

Figure 2.7 | Displacement spectral density. a, Displacement spectral density of the first mechanical mode, with optical detuning from the first optical mode. With the input power increasing from 0 to 9.5 μW, in addition to an observed optical stiffening, the amplitude decreases with a larger linewidth for a decrease in the effective temperature. The detuning $\Delta\tau$ is fixed at -0.25, for an optical Q of 5×10^5, m_{eff} of 2 pg, at 300K bath temperature. **b**, Displacement spectral density of the first and second allowed mechanical modes with different detunings. The scale bar is in dB with units of m^2/Hz (pump powers P_1 of 0.1 μW and P_2 of 50 μW used respectively in the modeling).

As shown above, both cooling and amplification can be realized in the optomechanical cavity through the red- and blue-detuning to the cavity resonance. An important question is what limiting temperature is achievable with the optical gradient force backaction cooling technique as described above. Two theoretical papers [31, 35] have extended the classical theory of radiation-pressure backaction cooling to the quantum regime and shown the close relationship that cavity backaction cooling has with the laser cooling of harmonically bound atoms and ions. The result can be simply divided by two conditions. In the unresolved side-band regime, $\kappa >> \Omega_m$, the ground state cooling is limited as: $n_f \approx \frac{\kappa}{4\Omega_m} >> 1$, where n_f is the minimum phonon number. On the other hand, in the resolved side-band regime, $\Omega_m >> \kappa$, occupancies well below unity can be attained yielding: $n_f \approx \frac{\kappa^2}{16\Omega_m^2} << 1$. Most of the present optomechanical cavities are in the unresolved sideband regime, either because low optical quality factor or low mechanical frequency, which limit the minimum phonon number higher than unity. However, since our ultrahigh-*Q/V* slot-type photonic crystal cavity has a high optical *Q* factor and higher mechanical frequency due to its small volume, it has significant potential to operate into the resolved sideband region. For example, for the first mechanical mode ($\Omega_m/2\pi$ of 460 MHz), an optical *Q* of more than 5×10^5 will bring the optomechanical oscillator within the resolved sideband limit with a n_f of 1×10^{-3}, allowing the potential to cool the mechanical mode to its ground state.

2.7 Conslusion

In this chapter, we illustrate numerically the slot-type mode-gap photonic crystal cavities for strong optical gradient force interactions. With the simultaneous strong optical field localization in $0.02(\lambda/n)^3$ modal volumes and cavity Q_o up to 5×10^6, we examined the optomechanical transduction of the various mechanical and optical modes for a dispersive coupling g_{om} up to 940 GHz/nm for the fundamental modes. Temporal coupled oscillations between the optical and mechanical fields are examined, along with effects of large optically-induced stiffening, cooling and resulting displacement spectral densities, for the various operating regimes in the slot-type optomechanical cavities.

Bibliography

[1] Kepler, J., De Cometis (1619).

[2] Lebedew, P., *Ann. Phys.* 311, 433 (1901).

[3] E. F. Nichols, and G. F. Hull, A Preliminary Communication on the Pressure of Heat and Light Radiation, *Phys. Rev.* 13, 307 (1901).

[4] A. Einstein, On the development of our understanding of the nature and composition of radiation, *Phys. Z.* 10, 817 (1909).

[5] T. W. Hänsch, and A. L. Schawlow, Cooling of gases by laser radiation, *Opt. Commun*. 13, 68 (1975).

[6] D. J. Wineland, and H. Dehmelt, The uncertain energy of an excited state, *Bulletin of the American Physical Society* 20, 637 (1975).

[7] A. Ashkin, Trapping of atoms by resonance radiation pressure, *Phys. Rev. Lett.* 40, 729 (1978).

[8] A. Ashkin, Optical trapping and manipulation of neutral particles using lasers, (World Scientific 2006).

[9] S. Stenholm, The semiclassical theory of laser cooling, *Rev. Mod. Phys.* 58, 699 (1986).

[10] H. J. Metcalf, and P. van der Straten, Laser Cooling and Trapping, (Springer, 1999).

[11] I. Bloch, J. Dalibard, and W. Zwerger, Many-body physics with ultracold gases, *Rev. Mod. Phys.* 80, 885 (2008).

[12] V. B. Braginsky, Measurement of Weak Forces in Physics Experiments (University

of Chicago Press, Chicago, 1977).

[13] V.B. Braginskii, A.B. Manukin, Ponderomotive Effects of Electromagnetic Radiation, *Sov. Phys. JETP* 25, 653 (1967).

[14] C. K. Law, Interaction between a moving mirror and radiation pressure – a hamiltonian-formulation, *Phys. Rev. A* 51, 2537 (1995).

[15] S. Mancini and P. Tombesi, Quantum-noise reduction by radiation pressure, *Phys. Rev. A* 49, 4055 (1994).

[16] I. Wilson-Rae, P. Zoller, and A. Imamoglu, Laser cooling of a nanomechanical resonator mode to its quantum ground state, *Phys. Rev. Lett.* 92, 075507 (2004).

[17] D. Kleckner and D. Bouwmeester, Sub-kelvin optical cooling of a micromechanical resonator, *Nature* 444, 75 (2006).

[18] O. Arcizet, P. F. Cohadon, T. Briant, M. Pinard, and A. Heidmann, Radiation-pressure cooling and optomechanical instability of a micromirror, *Nature* 444, 71 (2006).

[19] S. Gigan, H. R. Bohm, M. Paternostro, F. Blaser, G. Langer, J. B. Hertzberg, K. C. Schwab, D. Bauerle, M. Aspelmeyer, and A. Zeilinger, Self-cooling of a micromirror by radiation pressure, *Nature* 444, 67 (2006).

[20] T. J. Kippenberg, H. Rokhsari, T. Carmon, A. Scherer, and K. J. Vahala, Analysis of radiation-pressure induced mechanical oscillation of an optical Microcavity, *Phys. Rev. Lett*. 95, 033901 (2005).

[21] A. Schliesser, P. Del'Haye, N. Nooshi, K. J. Vahala, and T. J. Kippenberg, Radiation pressure cooling of a micromechanical oscillator using dynamical Backaction, *Phys. Rev. Lett.* 97, 243905 (2009).

[22] J. D. Thompson, B. M. Zwickl, A. M. Jayich, Florian Marquardt, S. M. Girvin, and J. G. E. Harris, Strong dispersive coupling of a high-finesse cavity to a micromechanical membrane, *Nature* 452, 06715 (2008).

[23] D. J. Wilson, C. A. Regal, S. B. Papp, and H. J. Kimble, Cavity optomechanics with stoichiometric SiN films, *Phys. Rev. Lett.* 103, 207204 (2009).

[24] F. Marquardt and S. M. Girvin, Optomechanics, *Physics* 2, 40 (2009).

[25] T. J. Kippenberg and K. J. Vahala, Cavity Opto-Mechanics, *Opt. Express* 15, 17172 (2007).

[26] T. J. Kippenberg and K. J. Vahala, Cavity Optomechanics: Back-Action at the Mesoscale, *Science* 321, 1172 (2008).

[27] I. Favero and K. Karrai, Optomechanics of deformable optical cavities, *Nature Photonics* 3, 201 (2009).

[28] D. Van Thourhout and J. Roels, Optomechanical device actuation through the optical gradient force, *Nature Photonics* 4, 211 (2010).

[29] H. Rokhsari, T. J. Kippenberg, T. Carmon, and K. J. Vahala, Radiation-pressure-driven micro-mechanical oscillator, *Opt. Express* 13, 5293 (2005).

[30] T. Carmon, H. Rokhsari, L. Yang, T. J. Kippenberg, and K. J. Vahala, Temporal behavior of radiation-pressure-induced vibrations of an optical microcavity phonon mode, *Phys. Rev. Lett*. 94, 223902 (2005).

[31] M. Eichenfield, C. Michael, R. Perahia, and O. Painter, Actuation of micro-optomechanical systems via cavity enhanced optical dipole forces, *Nature Photonics* 1, 416 (2007).

[32] P. T. Rakich, M. A. Popović, M. Soljačić, and E. P. Ippen, Trapping, corralling and spectral bonding of optical resonances through optically induced potentials, *Nature Photonics* 1, 658 (2007).

[33] R. Ma, A. Schliesser, P. Del'Haye, A. Dabirian, G. Anetsberger, and T. J. Kippenberg, Radiation-pressure-driven vibrational modes in ultrahigh-Q silica microspheres, *Opt. Lett*. 32, 2200 (2007).

[34] F. Marquardt, J. P. Chen, A. A. Clerk, and S. M. Girvin, Quantum theory of cavity-assisted sideband cooling of mechanical motion, *Phys. Rev. Lett.* 99, 093902 (2007).

[35] A. Schliesser, R. Riviere, G. Anetsberger, O. Arcizet, and I. J. Kippenberg, Resolved sideband cooling of a mechanical oscillator, *Nature Physics* 4, 415 (2008).

[36] M. Hossein-Zadeh and K. J. Vahala, Photonic RF down-converter based on optomechanical oscillation, *IEEE Photonics Technol. Lett*. 20, 234 (2008).

[37] Y.-S. Park and H. Wang, Resolved-sideband and cryogenic cooling of an optomechanical resonator, *Nature Phys.* 5, 489 (2009).

[38] Q. Lin, J. Rosenberg, X. Jiang, K. J. Vahala, and O. Painter, Mechanical oscillation and cooling actuated by the optical gradient force, *Phys. Rev. Lett.* 103, 103601 (2009).

[39] G. Anetsberger, O. Arcizet, Q. P. Unterreithmeier, R. Rivière, A. Schliesser, E. M. Weig, J. P. Kotthaus, and T. J .Kippenberg, Near-field cavity optomechanics with nanomechanical oscillators, *Nature Phys.* 5, 909 (2009).

[40] A. D. O'Connell, M. Hofheinz, M. Ansmann, R. C. Bialczak, M. Lenander, E. L.ucero, M. Neeley, D. Sank, H. Wang, M. Weides, J. Wenner, J. M. Martinis, and A. N. Cleland, Quantum ground state and single-phonon control of a mechanical resonator,

Nature 464, 697 (2010).

[41] Q. Lin, J. Rosenberg, D. Chang, R. Camacho, M. Eichenfield, K. J. Vahala, and O. Painter, Coherent mixing of mechanical excitations in nano-optomechanical structures, *Nature Photonics* 4, 236 (2010).

[42] M. L. Povinelli, M. Lončar, M. Ibanescu, E. J. Smythe, S. G. Johnson, F. Capasso, and J. D. Joannopoulos, Evanescent-wave bonding between optical waveguides, *Opt. Lett.* 30, 3042 (2005).

[43] M. Li, W. Pernice, C. Xiong, T. Baehr-Jones, M. Hochberg, and H. Tang, Harnessing optical forces in integrated photonic circuits, *Nature* 456, 480 (2008).

[44] M. Li, W. H. P. Pernice, and H. X. Tang, Tunable bipolar optical interactions between guided lightwaves, *Nature Photonics* 3, 464 (2009).

[45] M. Li, W. H. P. Pernice, and H. X. Tang, Reactive cavity optical force on microdisk-coupled nanomechanical beam waveguides, *Phys. Rev. Lett*. 103, 223901 (2009).

[46] G. S. Wiederhecker, L. Chen, A. Gondarenko, and M. Lipson, Controlling photonic structures using optical forces, *Nature* 462, 633 (2009).

[47] A. H. Safavi-Naeini, T. P. Mayer Alegre, M. Winger, and O. Painter, Optomechanics in an ultrahigh-Q slotted 2D photonic crystal cavity, arXiv: 1006.3964.

[48] M. Notomi, H. Taniyama, S. Mitsugi, and E. Kuramochi, Optomechanical wavelength and energy conversion in high-Q double-layer cavities of photonic crystal slabs, *Phys. Rev. Lett*. 97, 023903 (2006).

[49] H. Taniyama, M. Motomi, E. Kuramochi, T. Yamamoto, Y. Yoshikawa, Y. Torii,

and T. Kuga, Strong radiation force induced in two-dimensional photonical crystal slab cavities, *Phys. Rev. B* 78, 165129 (2008).

[50] J. Chan, M. Eichenfield, R. Camacho, and O. Painter, Optical and mechanical design of a "zipper" photonic crystal optomechanical cavity, *Opt. Express* 5, 3802 (2009).

[51] M. Eichenfield, J. Chan, A. H. Safavi-Naeini, K. J. Vahala, O. Painter, Modeling dispersive coupling and losses of localized optical and mechanical modes in optomechanical crystals, *Opt. Express* 17, 20078 (2009).

[52] M. Eichenfield, J. Chan, R. M. Camacho, K. J. Vahala, and O. Painter, Optomechanical Crystals, *Nature* 462, 78 (2009).

[53] S. Mohammadi, A. A. Eftekhbar, A. Khelif, and A. Adibi, Simultaneous two-dimensional phononic and photonic band gaps in opto-mechanical crystal slabs, *Opt. Express* 18, 9164 (2010).

[54] B.-S. Song, S. Noda, T. Asano, and Y. Akahane, Ultra-high-Q photonic double-heterostructure nanocavity, *Nature Materials* 4, 207 (2005).

[55] E. Kuramochi, M. Notomi, S. Mitsugi, A. Shinya, and T. Tanabe, Ultra-high-Q photonic crystal nanocavities realized by the local width modulation of a line defect, *Appl. Phys. Lett.* 88, 041112 (2006).

[56] T. Yamamoto, M. Notomi, H. Taniyama, E. Kuramochi, Y. Yoshikawa, Y. Torii, and T. Kuga, Design of a high-Q air-slot cavity based on a width-modulated line-defect in a photonic crystal slab, *Opt. Express* 16, 13809 (2008).

[57] M. Eichenfield, R. Camacho, J. Chan, K. J. Vahala, and O. Painter, A picogram-

and nanometre-scale photonic-crystal optomechanical cavity, Nature 459, 550 (2009).

[58] I.W. Frank, P. B. Deotare, M. W. McCutcheon, and M. Lončar, Programmable photonic crystal nanobeam cavities, *Opt. Express* 18, 8705 (2010).

[59] Y.G. Roh, T. Tanabe, A. Shinya, H. Taniyama, E. Kuramochi, S. Matsuo, T. Sato, and M. Notomi, Strong optomechanical interaction in a bilayer photonic crystal, *Opt. Express* 18, 8705 (2010).

[60] J. Gao, J. F. McMillan, M.-C. Wu, J. Zheng, S. Assefa, and C. W. Wong, Demonstration of an air-slot mode-gap confined photonic crystal slab nanocavity with ultrasmall mode volumes, *Appl. Phys. Lett.* 96, 051123 (2010).

[61] F. Riboli, P. Bettotti, and L. Pavesi, Band gap characterization and slow light effects in one dimensional photonic crystal based silicon slot-waveguides, *Opt. Express* 15, 11769 (2007).

[62] Y. G. Roh, T. Tanabe, A. Shinya, H. Taniyama, E. Kuramochi, S. Matsuo, T. Sato, and M. Notomi, Strong optomechanical interaction in a bilayer photonic crystal, *Phys. Rev. B* 81, 121101 (2010).

[63] A. Di Falco, L. O'Faolain, and T. F. Krauss, Chemical sensing in slotted photonic crystal heterostructure cavities, *Appl. Phys. Lett*. 94, 063503 (2009).

[64] V. Almeida, Q. Xu, C. A. Barrios, and M. Lipson, Guiding and confining light in void nanostructure, *Opt. Lett*. 29, 1209 (2004).

[65] J. T. Robinson, C. Manolatou, L. Chen, and M. Lipson, Ultrasmall mode volumes in dielectric optical microcavities, *Phys. Rev. Lett*. 95, 143901 (2005).

[66] S. G. Johnson, M. Ibanescu, M. A. Skorobogatiy, O. Weisberg, J. D. Joannopoulos,

and Y. Fink, Perturbation theory for Maxwell's equations with shifting material boundaries, *Phys. Rev. E* 65, 066611 (2002).

[67] C. W. Wong, P. T. Rakich, S. G. Johnson, M. Qi, H. I. Smith, L. C. Kimerling, Y. Jeon, G. Barbastathis, and S-G. Kim, Strain-tunable silicon photonic band gap microcavities in optical waveguides, *Appl. Phys. Lett.* 84, 1242 (2004).

[68] C. Jamois, R.B. Wehrspohn, L.C. Andreani, C. Herrmann, O. Hess and U. Gosele, Silicon-based two-dimensional photonic crystal waveguides, *Photonics and Nanostructures: Fundamentals and Applications* 1, 1-13 (2003).

[69] Stephen D. Senturia, *Microsystem Design* (Springer 2000).

[70] G. Anetsberger, R. Rivière, A. Schliesser, O. Arcizet, and T. J. Kippenberg, Ultralow-dissipation optomechanical resonators on a chip, *Nature. Photon.* 2, 627 (2008).

[71] A. A. Kiselev, and G. J. Iafrate, Phonon dynamics and phonon assisted losses in Euler-Bernoulli nanobeams. *Phys. Rev. B* 77, 205436 (2008).

[72] C. Zener, Internal Friction in Solids. I. Theory of Internal Friction in Reeds, *Phys. Rev.* 52, 230 (1937).

[73] T. H. Metcalf, B. B. Pate, D. M. Photiadis, and B. H. Houston, Thermoelastic damping in micromechanical resonators, *Appl. Phys. Lett.* 95, 061903 (2009).

[74] C. Cohen-Tannoudji, B. Din, and F. Laloe, *Quantum Mechanics* (Hermann, Paris, 1977), Vol. 1, Chap. 2; Vol. 2, Chaps. 11 and 13.

[75] H. A. Haus, *Waves and Fields in Optoelectronics* (Prentice-Hall 1984).

Chapter 3

Parametric optomechanical oscillations in slot-type photonic crystal cavities

3.1 Introduction

Photonic crystal (PhC) slab is a versatile platform for optical device development and scientific observations [1]. By adding defects to photonic crystal slab or waveguide, ultra-small volume (V) cavities can be engineered to have an ultra-high optical quality factor Q [2]. The large Q/V ratio indicates a strong internal optical field, which enables strong on-chip light-matter interactions due to the optical nonlinearities, such as free-carrier dispersion and two-photon absorption [3]. In recent years, the field of cavity optomechanics has attracted extensive attention for investigation of light-structure interactions [4-6]. Due to the improvement of micro- and nano-fabrication techniques, on-chip devices with unique geometries have been successfully demonstrated with well-coupled optical and mechanical modes, and much work has been done on actuation and cooling of their mechanical motions using optical pumps [7]. Compared with device platforms for microtoroid and microsphese etc., PhC slabs are shown to be an attractive, flexible platform for developing integrated devices that support well-coupled ultrasmall high-Q optical modes and small resonant mechanical modes [8,9]. The strong internal optical field of high-Q/V PhC cavities corresponds to a strong optical force with a low input optical power. The small size of the resonant mechanical device corresponds to a small physical mass or effective mechanical mass, which typically leads to a high mechanical frequency. The high mechanical frequency is important for reaching the sideband resolved regime, and is widely tunable by varying the geometrical parameters of the photonic crystal cavities [10]. The mechanical Q is another important factor for optomechanical applications, which is proportional to the coherence time of the

mechanical vibrations. It is possible to improve the mechanical Q of the PhC resonators by carefully engineering the anchor geometries to reduce the radiation losses. In particular, it is suggested that the radiation losses can be eliminated by anchoring the PhC resonator to artificial materials with complete mechanical band gaps covering the mechanical resonances [11-13]. Furthermore, the optomechanical coupling rates g_{om} of the reported photonic crystal cavities are high with well-overlapped optical and mechanical fields [9,10,14]. Among these cavities, the differential in-plane mechanical modes of the air-slot photonic crystal cavities show relatively higher optomechanical coupling rates since the optical resonant frequencies are very sensitive to the slot-width variations [15,16]. We have theoretically investigated the dispersive optomechanical coupling in an air-slot mode-gap photonic crystal cavity. In this chapter, we will experimentally demonstrate the optomechanical properties of fabricated samples. With a large optomechanical coupling rate, the optical induced spring effect, damping and amplification of the mechanical modes are observed with measurements in air. Behaviors above the parametric instability threshold are shown. Finally, the phase noise of the optomechanical oscillator is analyzed.

3.2 Device fabrication process

The air-slot optomechanical cavity used in these experiments is similar in geometry to the one examined in our former work [15,17]. An air-slot is created along a regular mode-gap cavity [18] and holes in the cavity center are shifted by a few nanometers.

The devices are fabricated using electron-beam nanolithography at Brookhaven

National Laboratory (BNL), on a silicon-on-insulator (SOI) substrate with 250 nm device thickness on top of a 3 μm buried oxide cladding. To prepare the wafer, we use an ultrasonicator and O_2 plasma to clean the surface of the wafer before spin-coating 100% ZEP 520A resist on it. The rotation speed of the spin is 4000rmp yielding a 300-nm thick resist coating. Electron-beam lithography is used to define the device after the resist coating is baked at 300^{o}C for three minutes. The layouts of the devices are drawn with autoCAD. Numerous variants of the "self-consistent dose correction" are applied to correct proximity effect by using LayoutBEAMER, which allows the nanopatterning of the 80 nm (line) slot next to the photonic crystal round holes, with high fidelity to create the photonic crystal nanocavities. The nanocavities are then written with the 50 MHz JEOL JBX-6300FS system (Fig. 3.1(a)) at 100 keV and 100pA current, with rigorously optimized base dose of 280 μC/cm^2. Because we use the positive resist ZEP520A, the polymer bonds will be broken with the beam, which makes the resist more soluble in the exposed areas. The nanopattern is developed in xylene for 90 seconds. The resulting pattern is then transferred into the silicon device layer through inductively-coupled plasma dry-etching at a rate of 20 nm/s. The ebeam resist is removed via Microposit solvent 1165 at 90°C and the large-membrane nanocavities air-bridged via wet-etching the underlying oxide in 5:1 buffered-oxide etchant for 7 minutes. The time of wet-etching may vary depends on the architectures of the devices. The samples are released with critical point drying technique to overcome stiction with high yield. The illustration of the fabrication process is shown in Fig. 3.1(b). Besides the slot-type photonics crystal cavities, we also fabricated other silicon photonics chips by

using the above fabrication procedure as shown in Fig. 3.1(c)

A scanning electron microscope (SEM) image of the fabricated sample is shown in Fig. 3.2(a). After calibration, statistical analysis of the SEM images shows that the measured lattice period a is 525 nm, radius r is 0.375a and slot width s is 105 nm. The lattice holes at the cavity center are shifted by 15 nm, 10 nm and 5 nm, respectively.

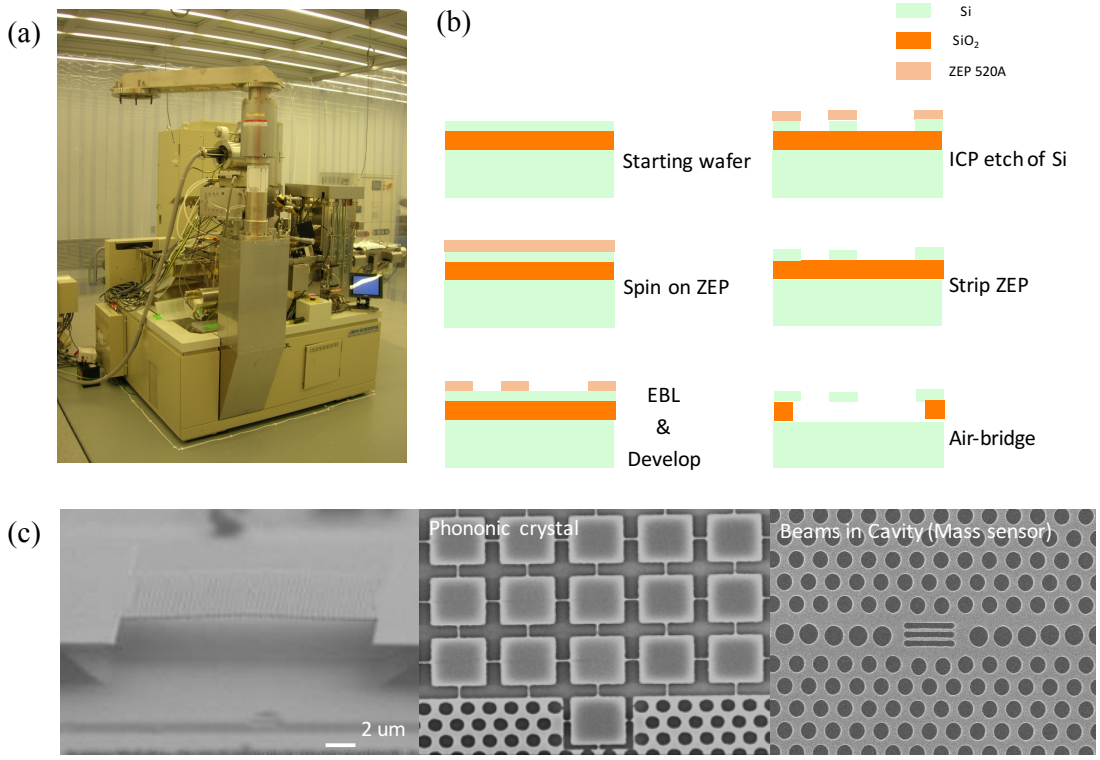

Figure 3.1 | **a,** 50 MHz JEOL JBX-6300FS system at Brookhaven National Lab. **b**, Scheme of nanofabrication procedure. **c**, SEMs of devices fabricated at BNL.

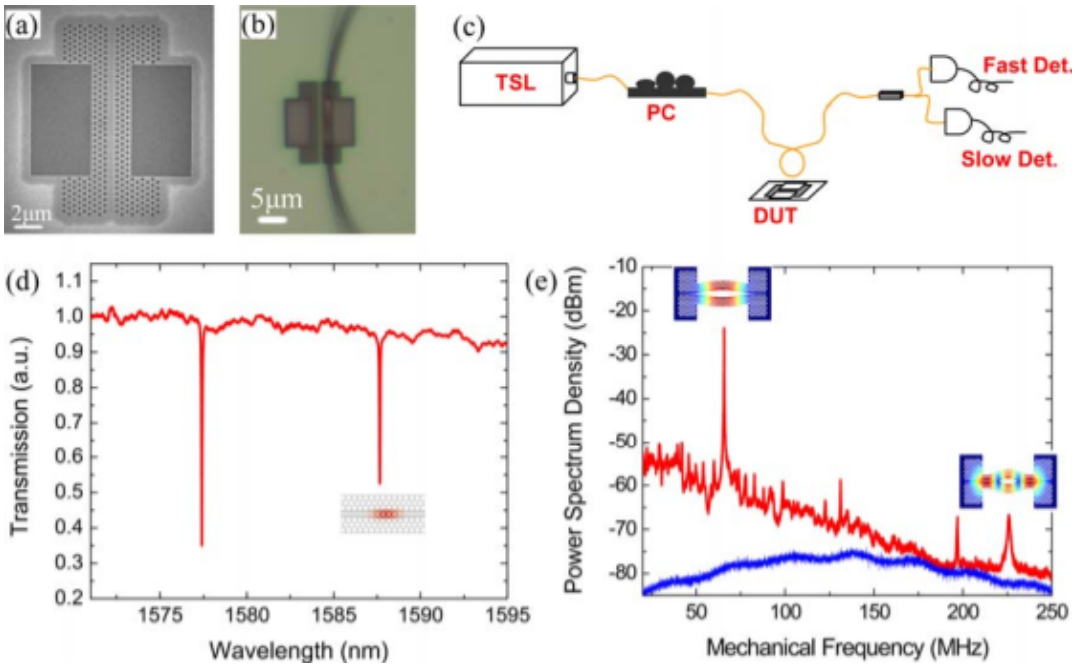

Figure 3.2 | **a,** SEM image of the fabricated sample. **b**, Optical microscope image showing the fiber taper loop loaded on the right side of the cavity. **c**, Simplified scheme of the measurements. **d,** Normalized optical transmission by laser scanning showing two cavity modes. The inset below the fundamental optical mode shows its electrical-field energy distribution. **e**, Red curve shows RF PSD at a blue detuning for the frequency range from 20 MHz to 250 MHz. The first three major peaks are related to the fundamental differential in-plane mechanical mode. The last major peak shows a high-order differential in-plane mechanical mode. FEM simulated frequencies matches the measured ones well. The displacement field distributions for these two modes are shown as insets on top of their RF peaks. The blue curve shows the measurement noise floor. The incident optical power is 81 mW and the resolution bandwidth is 10 kHz.

3.3 Experimental setup

The simplified measurement scheme is shown in Fig. 3.2(c). The light source is a high performance tunable laser (Santec TSL510 Type C, λ = 1500–1630 nm). The polarization state of the input light is optimized by using a polarization controller (PC). The device under test (DUT) is probed by a single-mode fiber taper with a single loop created at its thinnest region. The diameter of the loop is around 70 μm. To tune the coupling strength, the lateral taper-cavity distance is adjusted gradually with a step resolution of 25 nm. The looped fiber taper is then loaded on one side of the device as shown in Fig. 3.2(b). It is necessary to anchor the taper to the device to avoid fiber-taper oscillations due to the optical force when the laser wavelength is swept across the optical resonances. The optical transmission is monitored by a fast detector (New Focus Model 1811) and a slow detector simultaneously. The radio-frequency (RF) signal from another fast detector (New Focus Model 1611-AC) is analyzed by a power spectrum analyzer (PSA, Agilent E4440A) and an oscilloscope. The phase noise of the optomechanical oscillator is measured by a phase noise analyzer (Agilent E5052B), which employs the cross-correlation technique.

The tapered fiber stretching setup is as shown in Fig. 3.3(a). Single mode tapered fibers are home made by using the hydrogen flame on the setup. A one-meter long Corning SMF-28e single mode optical fiber is used. The ends of the fiber are cleaved and inserted into bare fiber connectors, which are then connected to an ASE laser and optical spectrum analyzer (OSA). These two equipments are used to monitor how the

optical transmission of the fiber changes when stretching. The fiber is then clamped down onto the stages. The stages are attached to two linear motors that are controlled by a Newport motion controller. The hydrogen flow is detected by a flow meter. The flow can be adjusted to a fixed value to keep the flame size of about 2-3 mm and the temperature of 2100 °C at its outer zone. In the middle of the 1-m fiber, the cladding is striped off for about 1.5 cm and the core is exposed and is placed in the outer zone of the flame. While the silica is melting, the linear motors slowly stretch on two ends of the fiber. An imaging system is employed to observe the diameter of the core. The transmission of the fiber will become a sinusoidal function when stretching because multi mode waves will transmit through the fiber. The stop point is determined by the transmission spectrum when it becomes a flat line again, which means the fiber is a single mode fiber. The diameter of the core of the fiber has decreased from 9 μm to approximately 1 μm. A good quality of the tapered fiber can have a transmission decrease of only -10 dB.

Unlike coupling light into a micro-ring or micro-disk that the tapered fiber can keep straight and be placed parallel to the resonator, it is harder to couple light into a resonator with a plane configuration, such as a 2D PhC cavity, using the tapered fiber. Usually, we will make a dimple at the tapered section. The Fig. 3.3(b) shows the setup that we used to make dimples. The tapered fiber is bent and then adhesive to a fiber mount. Another hydrogen torch is used to heat up the tip of a stripped fiber. The tip is on top of the fiber taper. While lifting up the tapered fiber, the heated fiber tip will press the tapered section down and stretch it for 30 seconds. After release the tip, there will be

a dimple at the tapered section, which makes it easier to couple light into the PhC cavities.

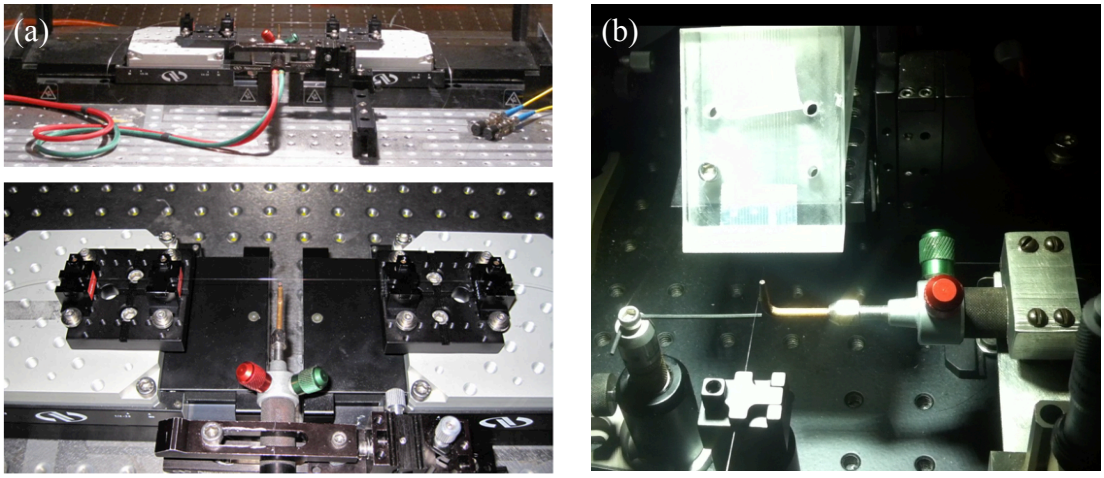

Figure 3.3 | **a,** Fiber stretching setup **b**, Setup to generate dimple on the tapered fiber

3.4 Optomechanical coupling

Fig. 3.2(d) shows the optical transmission measurement with two cavity modes examined. The high-order mode is a relatively delocalized mode at 1575.49 nm. The fundamental mode with resonant wavelength of 1587.645 nm is the expected high-Q mode based on the mode-gap effect. The measured loaded quality factor Q_{tot} is 32,900 and the intrinsic quality factor Q_{int} is 42,000. A three-dimensional finite-difference time-domain (FDTD) simulation [19], with the refractive index of silicon n_{Si} = 3.4, shows that the resonant wavelength for this mode is about 1584.95 nm, which matches our measurement very well. The theoretical intrinsic optical quality factor is higher than 1.3×10^6. The measured Q_{int} is much less than the theoretical Q, and is limited by the fabrication quality and surface-state absorption [16]. The optical mode volume is about $0.051(\mathrm{l}/n_{\mathrm{air}})^3$. The electrical field intensity of the cavity mode is also shown in Fig. 3.2(d). The maximum field intensity is located at the cavity center in the air slot. Due to its field distribution feature, the fundamental optical mode is well coupled with the selected differential in-plane mechanical modes, which will be shown later. Fig. 3.2(e) shows the measured RF power spectrum density (PSD) with incident power of 81 mW at the blue detuning of the fundamental optical mode. The resolution bandwidth is 10 kHz. Four major peaks are shown with frequencies of 65.68 MHz, 131.22 MHz, 196.93 MHz and 225.97 MHz. The first peak clearly indicates the fundamental mechanical mode, while the second and third peaks indicate its second and third harmonics respectively. The high-order

harmonics reflect the nonlinear optomechanical transduction from the Lorentzian optical lineshape. The mechanical modes are identified by using the finite-element method (FEM). In the frequency range up to 320 MHz, over sixty mechanical modes are obtained which are classified into three kinds: in-plane, out-of-plane and twisting modes. Each kind is composed by mode pairs of differential and common motions. The mechanical modes detected by the optical method are the modes with relatively large coupling with the optical mode. The optomechanical coupling rates $g_{\mathrm{om}} = d\mathrm{w}_o/dx$ are inversely proportional to the optomechanical coupling lengths. For the Fabry–Pérot cavity, g_{om} is easily determined by the cavity length. For complex cavity geometries such as the one examined here, g_{om} is derived by using a perturbation theory for Maxwell's equations with shifting material boundaries and calculated with the non-perturbed optical and mechanical fields [20, 21]. For the slot-type cavity here, the resonant optical frequency is strongly dependent on the slot width. Thus, the differential in-plane mechanical modes with relatively larger displacements at the cavity center have larger optomechanical coupling rates. As is expected, two of these modes are founded at frequencies 64.82 MHz and 231.41 MHz, which match very well with the experimentally observed major peaks. These two in-plane mechanical modes exhibit modeled optomechanical coupling rates of $g_{om}/2\pi$ = 564 GHz/nm and 393 GHz/nm respectively, which are at least fifty times larger than the other mechanical modes. Their displacement fields are shown in Fig. 3.2(e). The fundamental differential in-plane mechanical mode has an effective mass of 6.11 pg and an

effective mechanical volume of 2.62 mm^3. The vacuum optomechanical coupling rate $g^*/2\pi$ is 2.59 MHz which is large even for photonic crystal structures. In above simulations, density of silicon is 2.329×10^3 kg/m^3. Poisson's ratio is 0.28, and Young's modulus is 170 GPa [22].

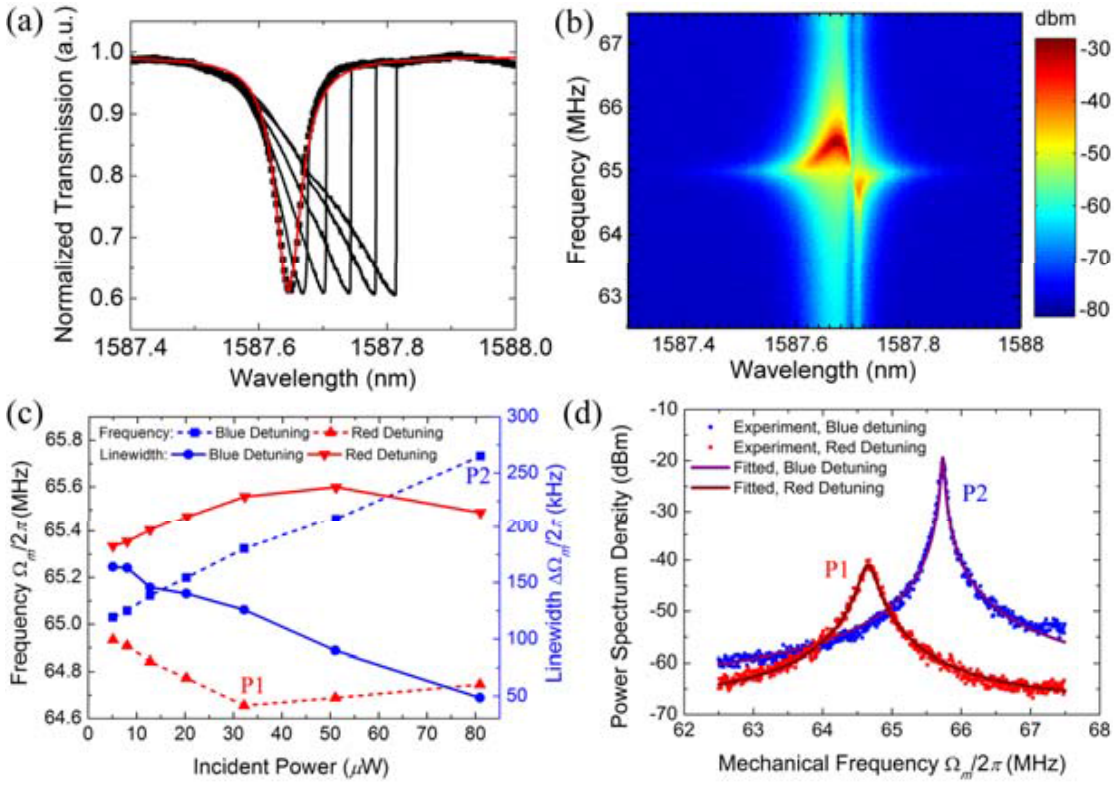

Figure 3.4 | a, Normalized optical transmission versus wavelength for increasing incident powers. Black dots for an incident power of 5.1 mW, black curves for 32.2 mW, 64.9 mW, 102.6 mW, 128.2 mW, and 162.2 mW respectively. The red curve is the fitted curve which gives a total quality factor Q_{tot} = 32,900 and an intrinsic quality factor Q_{int} = 42,000 under a low incident power. For higher incident powers, the red-shifted sharp edges indicate the thermal optical bistability. **b,** Example RF PSD by sweeping the laser wavelength. **c,** Mechanical frequency and linewidth versus incident power at the optimal detuning for the optical spring effect. **d**, RF PSD for points P1 and P2 indicated in panel **c**. The dots are the experimental values and the solid curves are the fitted.

The fundamental differential in-plane mechanical mode is selected for studying the optomechanical dynamics. Fig. 3.4(a) shows the optical transmission by the slow detector under different incident powers. As the power increases from 5.1 mW to 162.2 mW, the optical bistability arises mainly due to the two-photon absorption (TPA) [3]. The optical modification of the Brownian mechanical vibrations is measured by sweeping the incident wavelength across the resonance. As an example, Fig. 3.4(b) shows the obtained two-dimensional (2D) map of the RF PSD with the incident optical power of 51 mW. The wavelength is tuned with a 1 pm step. The RF PSD is given at each step. The blue detuning side and the red detuning side are separated by the zero-detuning line, where the RF signal is modulated in phase rather than in amplitude. The optical spring effect is shown with obvious increased mechanical frequency at the blue detuning side for this 65 MHz resonator. In the measurements, an incident power as low as 5.1 mW is able to introduce an observable mechanical frequency change due to the optical force. The 2D RF PSDs are analyzed and summarized for different incident powers in Fig. 3.4(c). The linewidth and frequency are extracted for the detuning with maximized optical spring effect. For powers more than 32.2 mW, there are bends on the curves for the red side detuning due to the difficulty of setting the laser wavelength to the theoretical optimal detuning. Using a linear fit of the non- bended parts of the curves, it is obtained that the intrinsic mechanical frequency $\omega_m/2\pi$ is 64.99 MHz and the cold cavity mechanical quality factor Q_m is 367. Furthermore, the experimental optomechanical coupling rate is also obtained with $g_{om}/2\pi$ = 154.1 GHz/nm, correspond to a

vacuum optomechanical coupling rate of $g^*/2\pi$ = 707.2 kHz. The discrepancy between the modeled and experimental optomechanical coupling rates is believed to be due to the coupling with the adjacent flexural mechanical modes [16]. Fig. 3.4(d) shows the measured and fitted RF PSDs for a red detuning point (P1) and a blue detuning point (P2) as indicated in Fig. 3.4(c). For P1, the mechanical frequency decreases by 345 kHz, and the Brownian motion of this mechanical mode dampens with an effective Q_m of 282.4. On the contrary, for P2 the mechanical frequency increases by 730 kHz, and the Brownian motion is amplified with a Q_m of 1358.3. The above observations show that the picogram slot-type cavity has a large optomechanical coupling rate which is of key importance for optomechanical studies. In addition, the mechanical frequencies for devices with different lengths and PhC lattice constants vary between 50 MHz to 120 MHz in the experiments.

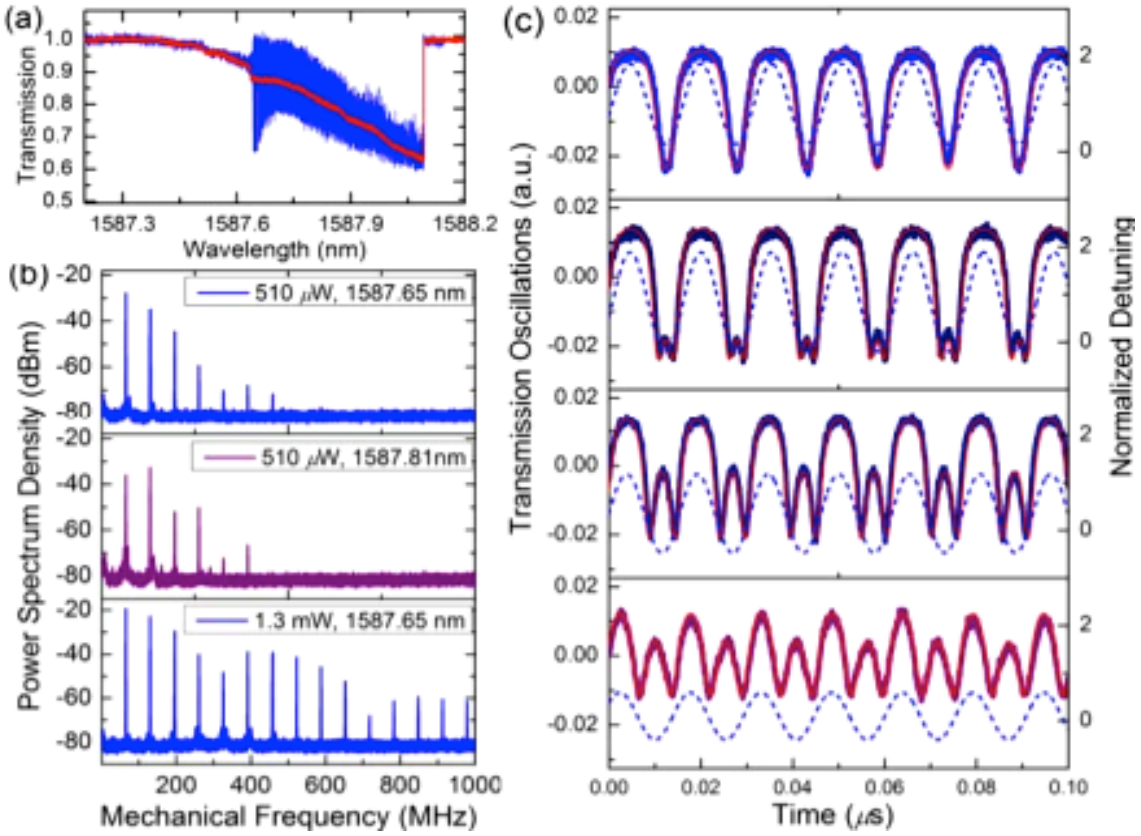

Figure 3.5 | a, Normalized optical transmission for an input power of 510 mW by sweeping laser wavelength across the optical resonance. Strong oscillations are shown by the blue curve, overlaid with the red low-pass-filtered signal. **b**, Power spectrum density of the transmission oscillations for different incident powers (510 mW and 1.3 mW) and wavelengths (1587.65 nm and 1587.81 nm). The reference bandwidth is 100 kHz. **c**, Transmission oscillations overlaid with modeled oscillations (Red curves) in time domain for incident power of 510 mW as used in (**a**). The incident wavelengths are varying from 1587.65 nm (the top panel) to 1587.81 nm (the bottom curve). The blue dashed curves show the corresponding real-time detuning. The detuning is normalized by the linewidth of the optical linewidth.

With a proper high input power, the optomechanical cavity starts to oscillate periodically when the intrinsic mechanical energy dissipation is overcome by the optical amplification. Fig. 3.5(a) shows the optical transmission for an input power of 520 mW by use of an oscilloscope. The blue line is obtained by the fast detector (New Focus Model 1811), and the red curve is obtained by using a low-pass filter with a cutoff frequency of 1.9MHz. The optically-driven oscillations rise suddenly near the wavelength 1587.65 nm which indicates the above-threshold behavior [23]. The filtered signal shows a sudden drop at that wavelength as seen in Fig. 3.5(a). In Fig. 3.4(c), the trend of linewidth for the blue detuning indicates a threshold power slightly higher than 100 mW with optimized detuning. This is confirmed by a series of swept-wavelength measurements with different incident powers. In Fig. 3.5(b) and (c), the transmission oscillations in frequency and time domains are given by using a low-noise fast detector with 1 GHz bandwidth (New Focus Model 1611-AC). It is shown that the detuning gets smaller, the second harmonic get relatively stronger and a second peak is rising in a single oscillation period. It indicates that the resonant optical frequency shift induced by optical pump gets comparable to the optical resonance linewidth. The effective real-time resonant wavelength is smaller than the incident wavelength for a certain time in a period, which is shown by the normalized real-time detuning in Fig. 3.5(c). By using a higher incident power, the nonlinearity of the optical power oscillations will get stronger due to a larger amplitude of the sinusoidal mechanical vibrations. An example with 1.3-mW input power is shown in the bottom panel of Fig. 3.5(b). Harmonics with frequency up to 1 GHz are observed.

The lineshape and spectrum show the dynamic interactions of the internal optical cavity field with the mechanical movement for different detuning and incident power, which is accurately described by temporal coupled-mode theory [15, 24].

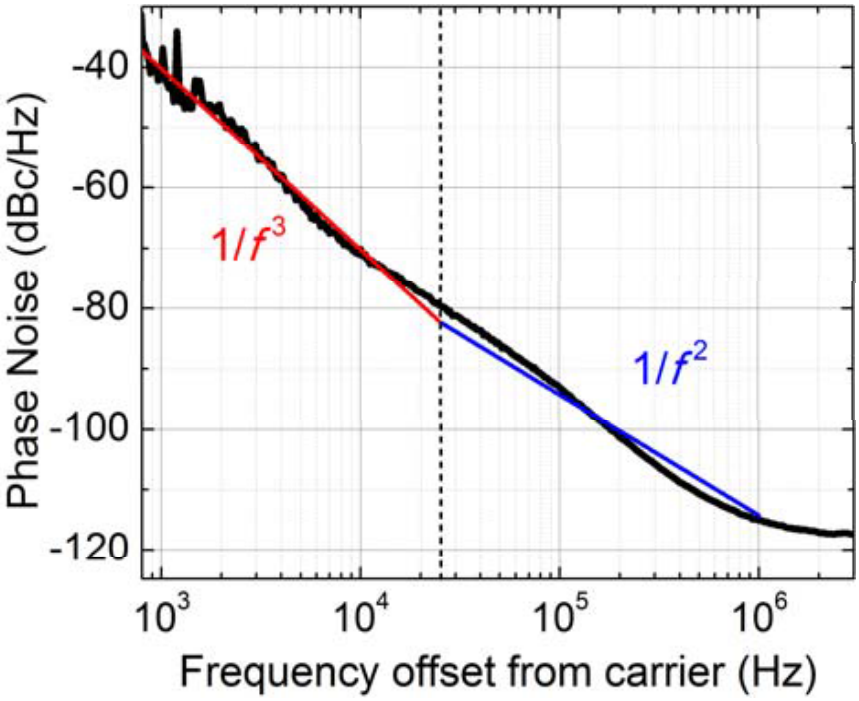

Figure 3.6 | Example phase noise spectrum of the optomechanical oscillations obtained with input power of 1.3 mW. The black curve shows experimental data, which is fitted by using a piecewise function. The red line indicates the $1/f^3$ dependence and the blue line indicates the $1/f^2$ dependence.

With the above-threshold condition satisfied, the optomechanical cavity is viewed as a self-sustained close-loop oscillator, which can be utilized as a photonic clock. The amplitude noise is suppressed above the threshold due to the inherent amplitude-limiting mechanism present in harmonic oscillators [25]. The phase noise in the system is measured with phase noise analyzers for high-precision estimation of the short-term linewidth and can be explained with Lesson's model [26]. In this model, there is always a $1/f^3$ region at small frequency offsets due to $1/f$ noise. After the corner frequency is the $1/f^2$ region due to the white frequency noise, which reflects the measurement limitations [27]. Here, the phase noise analyzer (Agilent E5052B) employs a two-channel cross-correlation technique for accurately analysis of the RF signal carried by the transmission light. In Fig. 3.6, the typical phase noise versus offset frequency is obtained with an input laser power of 1.3 mW. By fitting with a piecewise function following the Lesson's model, it shows that the corner frequency is 25.4 kHz. For offset frequencies less than 25.4 kHz, the $1/f^3$ dependence is predominantly related to relatively slow environmental vibrations. For offset frequencies larger than 25.4 kHz, the $1/f^2$ dependence is related to intrinsic properties of the oscillator. We note that the fitting for the $1/f^2$ region shows an averaged dependence rather than a well-matched dependence. The averaged dependence is possibly due to the noise contamination by coupling to nearby low-Q mechanical modes since the feedback loop of optomechanical oscillators is inherent. The anchored fiber taper also adds noise to the system [27]. Assuming a 1MHz

offset point in the $1/f^2$ regime, the phase noise of 117 dBc/Hz there corresponds to a short-term linewidth of 12.5 Hz. The root-mean-square (RMS) timing jitter integrated from 1 kHz to 1 MHz offset frequency is 758 ps with major contributions from 1 kHz to 10 kHz. The RMS timing jitter from 10 kHz to 1 MHz is about 81 ps. In future experiments, the phase noise performance of the current optomechanical oscillator will be improved by further engineering the mechanical Q and taking measurements in a more stable environment such as a vacuum chamber.

3.5 Conclusion

In this chapter, we have experimentally demonstrated the optomechanical behaviors of a slot-type high-optical-Q PhC cavity in air at room temperature. The optical and mechanical simulations match the experiments well. The optomechanical coupling rate between the selected mechanical modes and optical modes is quantified at $g_{om}/2\pi = 154$ GHz/nm. With the large optomechanical coupling, the optical spring effect, optical damping and amplification of the mechanical mode are all clearly exhibited. In the above threshold regime, time-domain oscillations are observed and the phase noises are analyzed. The device is shown to be a promising candidate for studying optomechanical dynamics and applications. Further experimental study will focus on improving the optical Q by optimizing the fabrication process and the mechanical Q_m by modifying the anchor geometry [28, 29]. The measured mechanical frequency is widely tunable by varying geometrical parameters. Additionally, it has the potential to be improved for

more challenging tasks such as side-band resolved cooling of the mechanical modes and work as a low-power low-noise photon clock.

Bibliography

[1] S. Noda, A. Chutinan, and M. Imada, *Nature* 407, 608 (2000).

[2] M. Notomi, E. Kuramochi, and T. Tanabe, *Nat. Photonics* 2, 741 (2008).

[3] X. Yang, C. Husko, and C. W. Wong, *Appl. Phys. Lett*. 91, 051113 (2007); C. Husko, A. Rossi, S. Combrie, Q. V. Tran, F. Raineri, and C. W Wong, *Appl. Phys. Lett.* 94, 021111 (2009).

[4] T. J. Kippenberg, and K. J. Vahala, *Opt. Express* 15, 17172 (2007).

[5] M. Li, W. Pernice, C. Xiong, T. Baehr-Jones, M. Hochberg, and H. Tang, *Nature* 456, 480 (2008).

[6] D. Van Thourhout, and J. Roels, *Nat. Photonics* 4, 211 (2010).

[7] A. Schliesser, R. Rivière, G. Anetsberger, O. Arcizet, and T. J. Kippenberg, *Nat. Physics* 4, 415 (2008).

[8] Y.-G. Roh, T. Tanabe, A. Shinya, H. Taniyama, E. Kuramochi, S. Matsuo, T. Sato, and M. Notomi, *Physical Review B* 81, 121101R (2010).

[9] M. Eichenfield, R. Camacho, J. Chan, Kerry J. Vahala, and O. Painter, *Nature* 459, 550 (2009).

[10] M. Eichenfield, J. Chan, R. M. Camacho, K. J. Vahala, and O. Painter, *Nature* 462, 78 (2009).

[11] S. Mohammadi, A. A. Eftekhar, A. Khelif, and A. Adibi, *Opt. Express* 18, 9164 (2010).

[12] Y. Pennec, B. Djafari Rouhani, E. H. EI Boudouti, C. Li, Y. EI Hassouani, J. O.

Casseur, N. Papanikolaou, S. Benchabane, V. Laude, and A. Martinez, *Opt. Express* 18, 14301 (2010).

[13] A. H. Safavi-Naeini, and O. Painter, *Opt. Express* 18, 14926 (2010).

[14] E. Gavartin, R. Braive, I. Sagnes, O. Arcizet, A. Beveratos, T. J. Kippenberg, and I. Robert-Philip, *Phys. Rev. Lett*. 106, 203902 (2011).

[15] Y. Li, J. Zheng, J. Gao, J. Shu, M. S. Aras, and C. W. Wong, *Opt. Express* 18, 23844 (2010).

[16] A. H. Safavi-Naeini, T. P. M. Alegre, M. Winger, and O. Painter, *Appl. Phys. Lett.* 97, 181106 (2010).

[17] J. Gao, J. F. McMillan, M.-C. Wu, J. Zheng, S. Assefa, and C. W. Wong, *Appl. Phys. Lett*. 96, 051123 (2010).

[18] E. Kuramochi, M. Notomi, S. Mitsugi, A. Shinya, T. Tanabe, and T. Watanabe, *Appl. Phys. Lett.* 88, 041112 (2006).

[19] A. F. Oskooi, D. Roundy, M. Ibanescu, P. Bermel, J. D. Joannopoulos, and S. G. Johnson, *Computer Physics Communications* 181, 687-702 (2010).

[20] S. G. Johnson, M. Ibanescu, M. A. Skorobogatiy, O. Weisberg, J. D. Joannopoulos, *Phys. Rev. E* 65, 066611 (2002).

[21] C. W. Wong, P. T. Rakich, S. G. Johnson, M. Qi, H. I. Smith, E. P. Ippen, L. C. Kimerling, Y. Jeon, G. Barbastathis, and S.-G. Kim, *Appl. Phys. Lett*. 84, 1242 (2004)

[22] M. A. Hopcroft, W. D. Nix, and T. W. Kenny, *Journal of Microelectromechanical systems* 19, 229 (2010).

[23] Q. lin, J. Rosenberg, X. Jiang, K. J. Vahala, and O. Painter, *Phys. Rev. Lett.* 103, 103601 (2009).

[24] T. Carmon, H. Rokhsari, L. Yang, T. J. Kippenberg, and K. J. Vahala, *Phys. Rev. Lett.* 94, 223902 (2005).

[25] M. Hossein-Zadeh, H. Rokhasari, A. Hajimiri, and K. J. Vahala, Phys. Rev. A 74, 023813 (2006). H. Rokhsari, M. Hossein-Zadeh, A. Hajimiri, and K. J. Vahala, *Appl. Phys. Lett.* 89, 261109 (2006).

[26] A. Hajimiri, and T. H. Lee, *Kluwer Academic Publishers*, 2003.

[27] S.Tallur, S. Sridaran, and S. A. Bhave, *Opt. Express* 19, 24522 (2011).

[28] K. Wang, A.-C. Wong, and C. T.-C. Nguyen, *J. of Microelectromechanical systems* 9, 347 (2000).

[29] G. Anetsberger, R. Rivière, A. Schliesser, O. Arcizet and T.J. Kippenberg, *Nat. Photonics* 2, 627 (2008).

Chapter 4

A chip-scale optomechanical DC accelerometer

4.1 Introduction

Recent advances in cold atom interferometry have determined the DC gravitational redshift to an accuracy of 7×10^{-9} [1], improved precision of the Newtonian gravitational constant to 1 part in 10^6 [2], and determined gravity to a sensitivity of 100 ng per shot [3]. With interferometric or timed measurements, detection approaching the standard quantum limit has been examined recently theoretically and experimentally [4]. Working with masses of tens of atoms, however, extreme force sensitivities are required for tens of $mg/Hz^{1/2}$ acceleration resolutions, necessitating unprecedented low-noise laser stabilization and atom cooling. Solid-state implementations, through coherent optical readout, can provide an alternative platform with significantly more massive resonators for DC acceleration detection, with wide applications in navigation, oil exploration, and earthquake prediction.

State-of-the-art solid-state accelerometers can be categorized into the following approaches [5-22]: (1) Capacitive sensing with the proof mass on one side of parallel plate or sensing capacitors. This approach involves compensating and amplification circuits to detect minute capacitance changes, and translate them into an amplified output voltage. (2) Piezoresistive sensing through mechanical resistive transduction in internal stresses of the support spring [23]. (3) Piezoelectric sensing, which provides a direct voltage from the displacement field through the material polarizability [24]. (4) Tunneling accelerometers based on electron tunneling and exponential sensitivity, along

with feedback control designs [25]. (5) Optical drive, sensing, and readout with coherent laser sources through evanescent-field or resonant cavity transduction [5, 6, 26-30].

In contrast to prior accelerometers using piezoelectric or capacitance readout techniques [31], optical readout provides narrow-linewidth high-sensitivity laser detection along with low-noise resonant optomechanical transduction at the standard quantum limit. In this chapter, we demonstrate an optomechanical accelerometer with DC resolution at 730 ng/$Hz^{1/2}$ (or equivalently 40.1 aN/$Hz^{1/2}$), with a transduction bandwidth of ≈ 85 kHz, towards gravimetry. Driven into the optomechanical sustained-oscillation mode, the slot photonic crystal cavity provides a radio-frequency (RF) readout of the optically-driven transduction with an enhanced sensitivity of 196 ng per Hz of RF shift. Measuring the optomechanically-stiffened oscillation, instead of optical transmission shift, provides a 125.1× resolution enhancement over pre-oscillation mode detection due to strong optomechanical transduction and readout in the optical domain. Our DC acceleration measurements operate at the thermal limit and 3.7× the quantum backaction noise, with a 23.5 dB dynamic range, supported by our theory and numerical modeling. The solid-state room-temperature silicon DC accelerometer architecture is robust for portability and field deployment.

Recent advances in radiation-pressure driven cavity optomechanics have provided new frontiers for laser cooling of mesoscopic systems [32-34], chip-scale stable RF sources and filters [35, 36], phonon lasers [37]], induced-transparency through multi-mode interferences [38, 39], and explorations into potential quantum transductions of microwave, spin, and optical qubits [40, 41]. The coupled optical and mechanical

degrees-of-freedom [42] allows detection of nanomechanical motion [43-45] towards force sensing [46], radio wave detection [47], and z-axis accelerometers [48]. This also includes recent efforts in AC acceleration through piezoelectric shakers, such as with bulk fiber cavities at 100 ng/Hz$^{1/2}$ resolution [49] or one-dimensional nanobeam chip-scale cavities at 10 μg/Hz$^{1/2}$ resolution with lock-in detection [50], and without driving into self-regenerative narrow-linewidth oscillation modes. Driven by optically-induced gradient force [45], our tight sub-wavelength confinement in photonic crystal cavities [51] allows for one of the largest optomechanical transduction coefficient $g_{om}/2\pi$ [52] along with the large motional mass for sensing in gravimetry.

We also emphasize our approach is through resonant driving (different from AC sensing) to measure the DC acceleration. With resonant acceleration sensing, this offers the advantages of: (1) high-resolution, (2) large dynamic range, as well as (3) direct (RF) frequency readout, compared to static optical or electronic readout sensing approaches.

4.2 Device design and fabrication

The coherent optomechanical coupling rate $g^*/2\pi$ is obtained through first-order perturbation theory and computed through the closed-form integrals of the electromagnetic fields and displacement fields of the DC accelerometer including the relative permittivities. The optical resonant modes and electromagnetic fields of the photonic crystal cavity are obtained from finite-difference time-domain (FDTD) simulations through a freely available software package (MEEP). Mechanical displacement fields and modes are determined with COMSOL Multiphysics. Coupled

mode theory on the optical fields and the harmonic oscillator [52] is used to model the optical stiffening of the RF tone and the dynamical shifts.

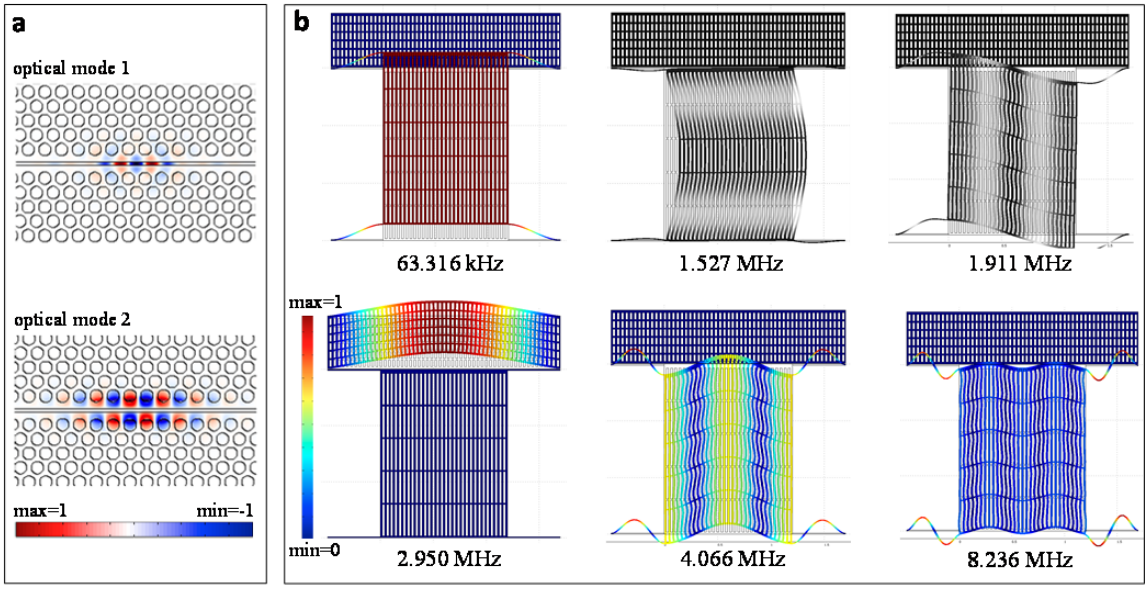

Figure 4.1 | Optomechanical accelerometer design. a, Modeled transverse-electric field distribution of the two resonant optical modes of the slot cavity. **b,** Modeled displacement field of the first six mechanical modes of the accelerometer. The fundamental mode of the proof mass, as the first deformation field shown, is used to test the acceleration. The resonant frequency is listed below each panel. Modes in color can couple to optical mode 1 and are symmetric with respect to the *y*-axis. From symmetry, modes in grey are not excited.

Cavity optomechanics [53-58] can have resonators with laser red-detuned to cool towards or at the quantum mechanical ground state [59-61] or blue-detuned to be driven into oscillation mode [62-68], along with coupled states [69], and quantum transduction or states [70-73]. In our subset with the slot-type photonic crystal cavity, the optical cavity modes are designed with MEEP [74] and mechanical modes are designed with COMSOL Multiphysics. The resulting optical and mechanical modes are illustrated in Figure 4.1. For an optomechanical system, the coupling rate is defined as $g_{om} = d\omega/dx$ [29, 75]. The spring effect is driven by dynamical backaction, which can be derived from coupled equations of motion [76] for the optical and mechanical modes. With a constant acceleration signal applied on the proof mass, we add a corresponding signal force in the vibration equation:

$$\frac{da}{dt} = i\Delta(x)a - \left(\frac{1}{2\tau_o} + \frac{1}{2\tau_{ex}}\right)a + i\sqrt{\frac{1}{2\tau_{ex}}}s \qquad (1)$$

$$\frac{d^2x}{dt^2} + \frac{\Omega_M}{2Q_M}\frac{dx}{dt} + \Omega_M^2 x = \frac{F_o(t)}{m_{eff}} + \frac{F_T(t)}{m_{eff}} + \frac{F_s}{m_{eff}} \qquad (2)$$

The first equation describes the dynamics of the optical field, where $|a|^2$ is the stored cavity energy and $\frac{1}{2\tau} = \frac{1}{2\tau_0} + \frac{1}{2\tau_{ex}}$ is the optical field decay rate. For an oscillator, a constant applied force will result in a displacement shift $x_s = \frac{F_s}{\Omega_M^2 m_{eff}}$. Thus, the displacement can be written as: $x = x_a + x_s$, where x_a is the solution of the mechanical equation without the constant force. For $x = x_o \sin(\Omega_M t) + x_s$, the solution of the coupled equations can be obtained from Bessel function:

$$\tilde{a}(t) = a(t)e^{-i\omega_l t} = \sqrt{\frac{\eta_c}{\tau}} s \sum_{n=-\infty}^{+\infty} \frac{(-i)^n J_n(\beta)}{-i(\omega_l + n\Omega_M - \omega_c + g_{OM}x_s) + \frac{1}{2\tau}} e^{-i(\omega_l + n\Omega_m)t + i\beta\cos(\Omega_M t)} \quad (3)$$

where $\beta = g_{OM}x_o/\Omega_M$. In our case, detuning Δ (= ω_l - ω_c) >> Ω_M, and we obtain the effective frequency as:

$$\Omega'_M = \sqrt{\Omega_M^2 + \left(\frac{2|a|^2 g_{OM}^2}{((\omega_l - \omega_c + g_{OM}x_s)^2 + (1/2\tau)^2)\omega_c m_{eff}}\right)(\omega_l - \omega_c + g_{OM}x_s)} \quad (4)$$

Figure 4.2 illustrates the numerical modeling of the optomechanical transduction rate change with slot width, as well as the effective optomechanical vibration frequency shift (optomechanical stiffening) for slot width changes.

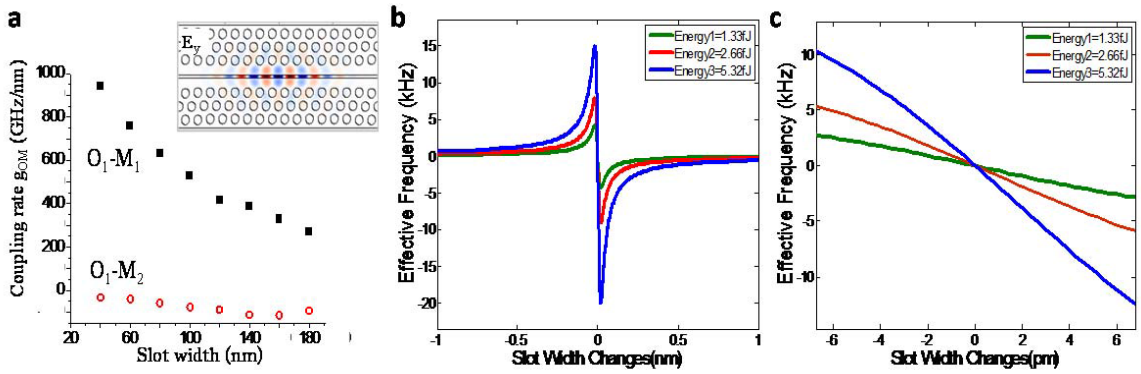

Figure 4.2 | Design of chip-scale DC accelerometer frequency shifts. a, Modeled optomechanical coupling rates. Fundamental optical mode coupling with first- (black solid squares) and second- (red open circles) allowed mechanical modes, computed for the different slot width *s*. The inset panel is the E_y-field distribution of the slot accelerometer. **b,** Modeled overall RF shift for various sensed slot-cavity gaps *s*, for 1.33 fJ (red), 2.88 fJ (blue), and 5.32 fJ (green) intracavity stored energies. **c,** Zoom-in of RF frequency shift for slot cavity displacements Δs of 13 pm.

Figure 4.3a illustrates the optomechanical DC accelerometer nanofabricated in a silicon-on-insulator (SOI) substrate with a 250 nm thick silicon layer. A slot-type photonic crystal cavity with optical gradient force transduction is designed and located at the device center, with shifted and perturbed lattice holes [51, 52] to form the localized optical resonant modes. The slot cavity features a slot width s of 80 nm, 470 nm photonic crystal lattice constant (a), and 150 nm hole radii, with 5 nm (red), 10 nm (green) and 15 nm (blue) lattice perturbations, as shown in Figure 4.3b, to form the localized cavity mode on a line-defect waveguide with width $1.2\times a$. The cavity mode volume is subwavelength at $0.051(\lambda/n)^3$ with the $|E|^2$-distribution illustrated in Figure 4.3b inset. The large ($\approx$ 120 μm × 150 μm) 5.6 ng proof mass for DC acceleration detection has four (1 μm × 50 μm) compliant support beams providing a 63.3 kHz fundamental resonance and a 885.8 mN/m combined stiffness, and is attached to one side of the slot cavity as shown as section *i* in Figure 4.3a. The other side (*ii*) of the slot cavity is anchored to the substrate and has the same x-length as the proof mass to reduce asymmetric residual stress z-bow between the two sections (*i* and *ii*), in order to preserve the localized optical resonance mode.

The DC accelerometers are fabricated with electron-beam nanolithography at Brookhaven National Laboratory, on a SOI substrate with 250 nm device thickness on top of a 3 μm buried oxide cladding. To prepare the wafer, we use an ultrasonicator and O_2 plasma to clean the surface of the wafer before spin-casting 100% ZEP 520A resist on it. Proximity error correction with LayoutBEAMER allows the nanopatterning of the 80 nm (line) slot next to the photonic crystal round holes, with high fidelity to create the

photonic crystal nanocavities. The nanocavities are then written with the 50 MHz JEOL JBX-6300FS system at 100 keV, with rigorously optimized base dose of 280 $\mu C/cm^2$. Numerous variants of the "self-consistent dose correction" are applied to correct proximity effect. The nanopattern is developed in xylene for 90 seconds. The resulting pattern is then transferred into the silicon device layer through inductively-coupled plasma dry-etching at a rate of 20 nm/s. The ebeam resist is removed via Microposit solvent 1165 at 90°C and the large-membrane nanocavities air-bridged via wet-etching the underlying oxide in 5:1 buffered-oxide etchant for 17 minutes. The samples are released with critical point drying technique to overcome stiction with high yield.

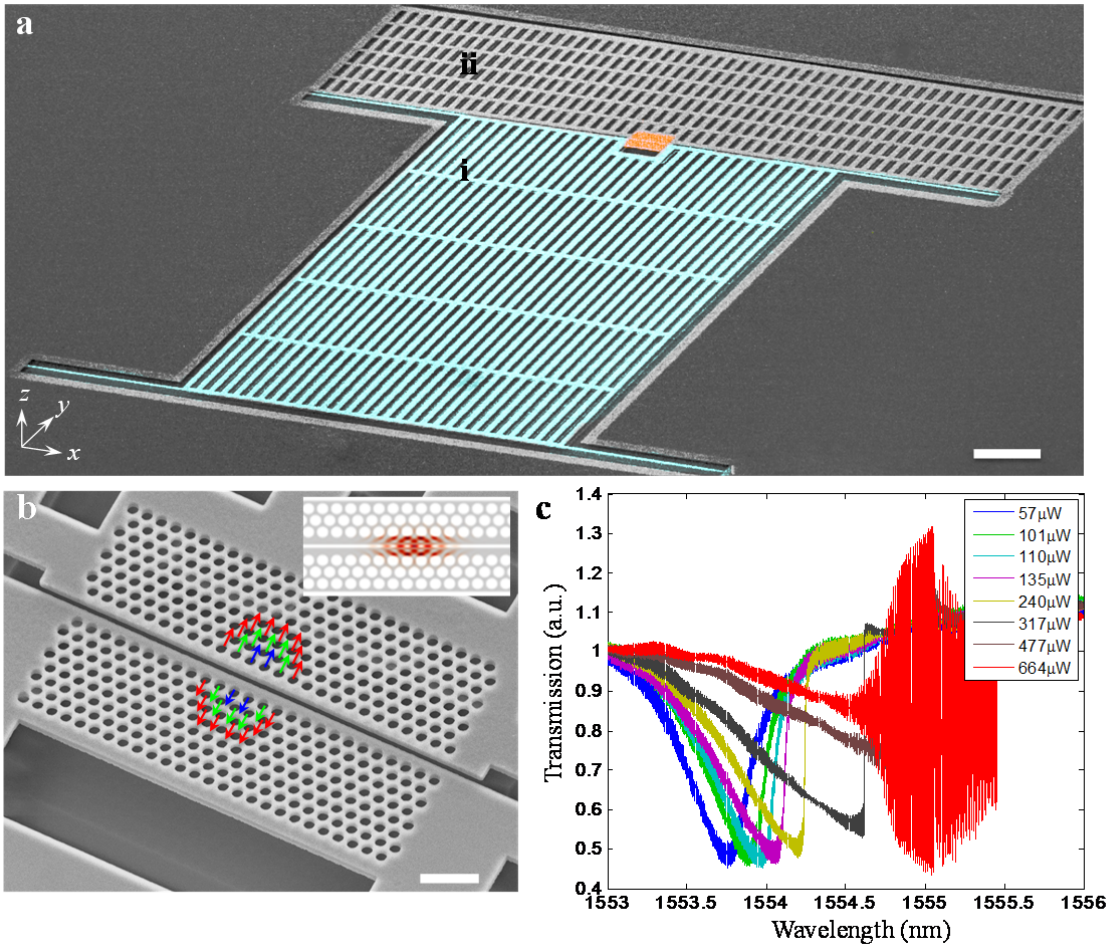

Figure 4.3 | A chip-sale optomechanical DC accelerometer through optical readout. **a,** Scanning electron micrographs (SEMs) of DC accelerometer nanofabricated in silicon-on-insulator (250 nm device layer) with a 5.6 ng proof mass and co-designed slot-type photonic crystal cavity with a 80 nm slot width *s*. The fundamental mechanical resonance is designed around 60 to 85 kHz, above most of the ambient, acoustic and seismic vibrational noise frequencies. Section *i* (in cyan) is the moving mass and section *ii* (in grey) is the stationary section. Scale bar: 20 μm. The orange region is the slot-type

photonic crystal cavity, with the dashed white box expanded in panel **b**. **b**, Colored arrows denote the 5 nm (red), 10 nm (green) and 15 nm (blue) photonic crystal lattice perturbations to form the slot-localized resonance modes with $0.051(\lambda/n)^3$ mode volumes. Inset: computed $|E|^2$-distribution for the designed nanocavity. Scale bar: 2 μm. **c,** Optical transmission spectra of the DC accelerometer, with increasing drive and readout powers (57 μW to 664 μW) including observations of self-induced regenerative oscillations with the signature spectral fluctuations (in red).

4.3 Optomechanical coupling

We mount the tapered fiber and optomechanical DC accelerometer on a controlled Aerotech ADRS-200 rotary stage to impart the true acceleration onto the chip. This high-torque rotary stage is driven by a brushless servomotor and equipped with direct coupled, high-accuracy rotary encoders. With the Soloist digital scope control, the control filter parameters are set at the optimal gain values (position loop gain k_{pos} = 10, integral gain k_i = 500, and proportional gain k_p = 105,000) to drive the acceleration to the set values promptly without overtone ringing, with our low rotational velocities and large measurement setup load. The 5-axis Attocube positioners in a Janis ST-500 chamber is mounted 21.60 ± 0.01 cm from the rotational center for the centrifugal force. A dimpled tapered fiber with more than 90% transmission is coupled to the DC accelerometer, with a flange fiber-through into the sealed chamber, by anchoring the fiber dimple directly on the chip surface and on side *ii* (see Figure 4.3b) of the optomechanical slot cavity. The optical resonance intensity is monitored to ensure that the transmission and coupling are maintained rigorously during the slow rotation. The optical drive and readout is performed with a tunable laser diode (Santec TSL-510) and polarization control, along with photodetector readout of the RF and optical spectra simultaneously. A high-resolution commercial accelerometer is placed on the opposite side of the rotating stage but, at our low acceleration levels, is always in the noise floor. We note that a polarization maintaining fiber is designed and employed to maintain the stable drive polarization while the stage is rotating.

For the purpose of a vacuum experiment environment, the tested device, the

nanopositioning stages and tapered fiber are placed inside a customized Janis ST-500 cryostat. Measured devices are placed under the vacuum chamber-imaging window, which allows us to control the tapered fiber coupling to the device. The 5-axis Attocube positioners translate the devices over a 5 mm travel range with sub-nanometer scanning resolution in fine-positioning mode. The prepared tapered fibers have a transmission of 90%. It is connected with the drive laser and detector outside the vacuum chamber through Teflon fiber feedthroughs. An Edwards T-Station 75 turbopump is used to evacuate the chamber to high vacuum. The pumping station consists with an E2M1.5 backing pump and a XDD1 turbo pump, allowing the chamber to reach 10^{-7} mbar vacuum.

Probed by a dimpled tapered fiber anchored to side *ii* of the optomechanical cavity, Figure 1c shows the measured optical transmission spectra under different drive powers. Under low-drive power (57 μW), the loaded cavity quality factor Q_o is measured at ≈ 4,350 (intrinsic cavity Q_{in} at ≈ 13,200). With increasing drive power, thermal nonlinearity broadens the cavity lineshape into Fano-like resonances. With pump powers greater than 477 μW, the optomechanical cavity is driven into self-induced regenerative oscillations [36] – with significantly narrower RF linewidth and the signature spectral fluctuations (shown in red of Figure 4.3c). On the 63.3 kHz RF resonance, the oscillator linewidth is instrumentation resolution-bandwidth-limited at ≈ 50 mHz.

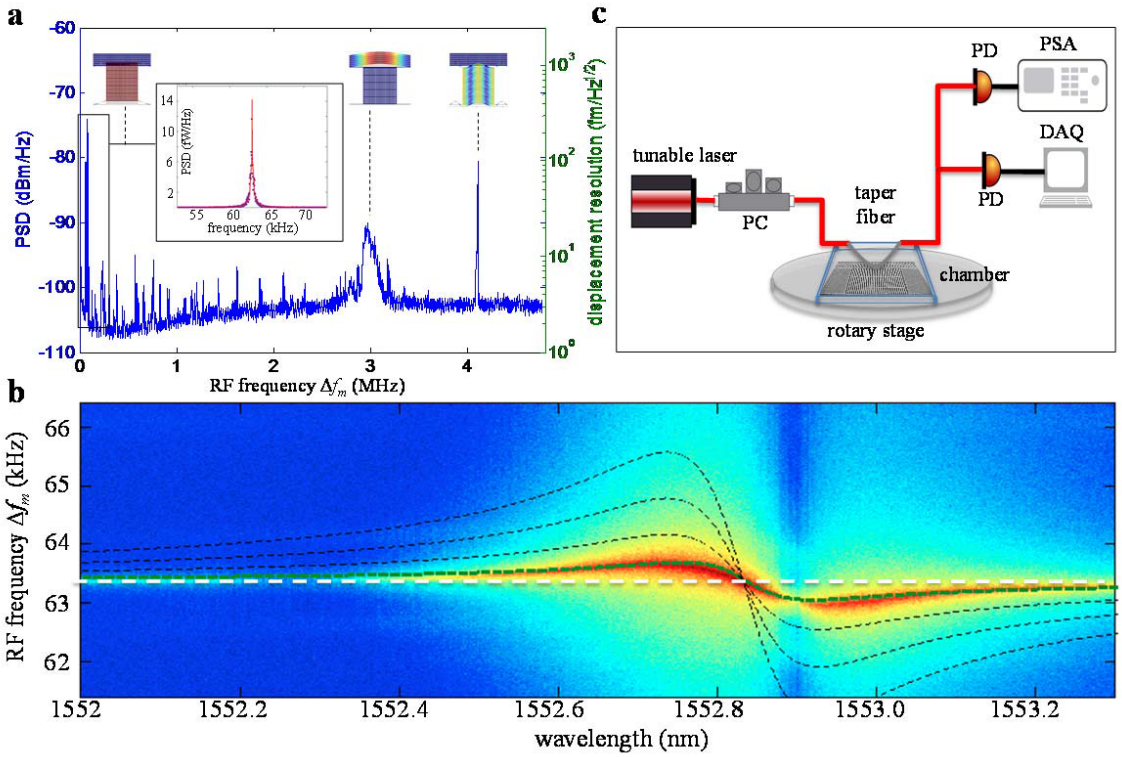

Figure 4.4 | DC accelerometer transduction and enhanced sensitivity in the RF domain. a, Optical gradient force backaction transduction into the RF power spectral density. The RF resonances at 63.3 kHz, 2.95 MHz, and 4.10 MHz represent the first three coupled modes respectively, along with the modelled displacement profiles in the inset. Q_m is 1,658 and the measurement resolution bandwidth is 1 Hz. The equivalent displacement sensitivity is shown on the right *y*-axis. **b,** 2D map of the transduction and optomechanical spring effect in the DC accelerometer. The wavelength resolution is 2 pm on a 1552.833 nm optical resonance, at 370 μW input power. The dashed lines show the numerical modeling of the backaction transduction for different laser-cavity detunings, with the green middle line at 370 μW input and the others at 550 μW , 640 μW and 920 μW respectively. **c,** Measurement setup schematic with dual-detectors for

RF tracking and simultaneous optical power monitoring. Optical drive and readout is coupled through tapered fiber coupling. Devices are placed in a vacuum chamber on a rotation stage.

Figure 4.4a shows an example RF spectrum simultaneously monitored with the optical transmission with dual photodetectors, illustrating the fundamental mechanical resonance and higher-order 2.95 MHz and 4.10 MHz excited modes (corresponding modelled displacement field profiles shown in inset). The proof mass displacement is described by $x(\omega) = (m^2 - \omega^2 + i\omega\omega_m/Q_m)^{-1}$ a$(\omega) = \chi(\omega)$ a(ω) when subjected to an external acceleration $a(\omega)$. In the low frequency regime ($\omega << \omega_m$), $\chi(\omega) \approx 1/m^2$ for an accelerometer bandwidth ω_m of 63.3 kHz. The right y-axis of Figure 4.4a shows the corresponding power spectral density in displacement noise units, reaching displacement resolutions of 10 to 100 fm/Hz$^{1/2}$ on resonance.

In the slot-type optomechanical cavity, resonant enhancement of the pump-laser optical gradient force yields strong backaction and, with the deeply sub-wavelength confinement, the optomechanical stiffening and optical-RF resonance spectra of the cavity are strongly dependent on the slot width s [26]. In the presence of a (+y direction) acceleration the two side-membranes of the slot cavity displace differentially, decreasing the slot width s. Consequently, the optomechanical stiffening increases with a resulting modified (and increased) RF frequency resonance Ω'_m described by:

$$f'_m = \sqrt{f_m^2 + \left(\frac{2|a|^2 g_{om}^2}{\Delta^2 \omega_c m_x}\right)\Delta_0} = \sqrt{f_m^2 + \left(\frac{2|a|^2 g_{om}^2}{(\omega_l - \omega_c)^2 + (\Gamma/2)^2 \omega_c m_x}\right)(\omega_l - \omega_c)} \qquad (4)$$

where fm' (fm) is the shifted (unperturbed) resonance frequency, $|a|^2$ the averaged intracavity photon energy, g_{om} the optomechanical coupling rate, m_x the effective mass, and Γ and ω_c the optical cavity decay rate and resonance respectively. From equation

(4), we also note the strong dependence of RF spectra on the optical cavity resonance and laser detuning $\Delta_0 = \omega_l - \omega_c$ and $\Delta^2 = \Delta_0^2 + (\Gamma/2)^2$, which enhances the minimal displacement resolution detection.

Figure 4.4b next illustrates the measured 2D RF spectra, in a static (non-acceleration) frame for the test case with a swept pump wavelength. In this device characterization, the optical resonance is 1552.83 nm at 370 μW incident power with a 1.33 fJ optical intracavity energy. The modeled mechanical frequency for different detunings [equation (4)] is also superimposed on the 2D measurement. From the measurement-model correspondence, we obtain the optomechanical coupling rate $g_{om}/2\pi$ = 37.1 GHz/nm, with a vacuum optomechanical coupling rate $g^*/2\pi$ = 345 kHz. Pre-oscillation, the measured vacuum mechanical quality factor Q_m is ≈ 1,658 and largely bounded by the large mass and anchor losses. Driven into oscillation mode, the measured linewidth is bounded by the resolution-bandwidth [77]. We observe that the RF resonance has a strong optical resonance dependence from 1552.81 nm to 1552.88 nm (or equivalently, the slot width *s*), with a mechanical resonance frequency shift Δf_m of 450 Hz over an externally-driven 70 pm wavelength detuning. We note that the measured $g_{om}/2\pi$ is smaller than theoretically predicted due to height asymmetries of the released masses (of sections *i* and *ii* in Figure 1a), lowering the optomechanical transduction from designed values. With increased injected optical power, the RF shift is larger due to the stronger optical gradient force.

Figure 4.5 illustrates the measured 2D RF spectra with different laser wavelengths and powers to study the optomechanical stiffening and damping of the

accelerometer. Four sets of complete results are measured with incident powers of 94.8 μW, 301 μW, 476 μW, and 754 μW respectively. From the 2D RF maps, we also fit the mechanical frequency shift as a function of laser-cavity detuning Δ; this fitting indicates a $g_{om}/2\pi$ = 3.1 GHz/nm.

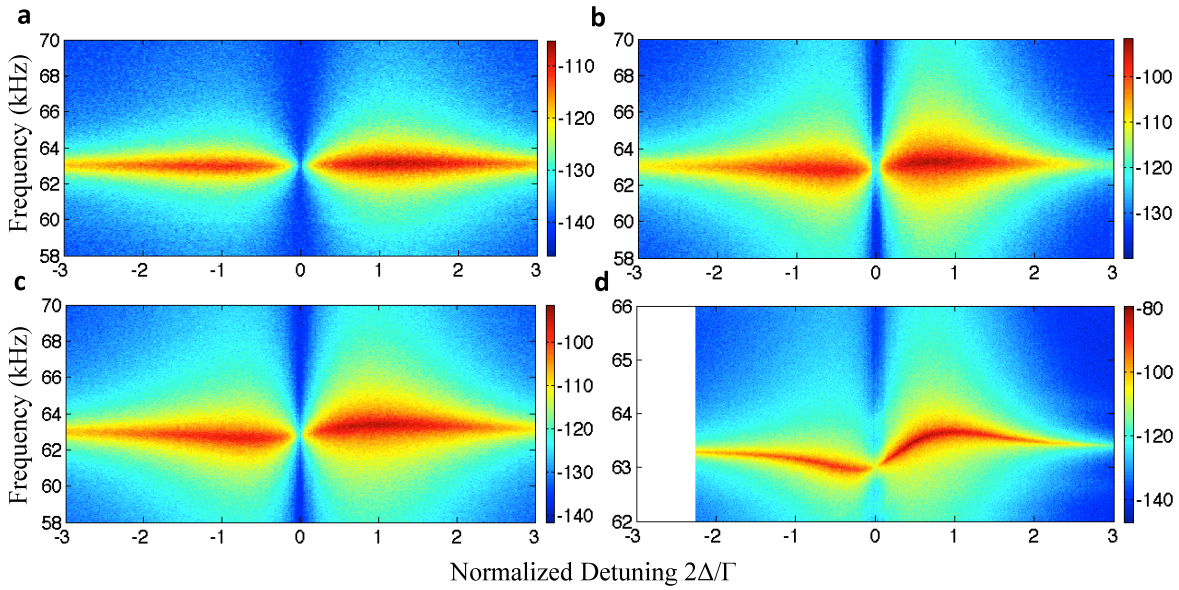

Figure 4.5 | Measured 2D RF spectra for different input powers. The mechanical sensing frequency and linewidth changes with detuning (Δ) is illustrated for different input powers of (**a**) 94.8 μW, (**b**) 301 μW, (**c**) 476 μW, and (**d**) 754 μW. The optical cavity linewidth is 350 pm or a cavity decay rate Γ of 43 GHz. When the detuning is large or the input power is lower than -5 dBm, RF spectrum represents the eigenfrequency of the proof mass at 63.3 kHz. With increased input pump power, the optomechanical damping and spring effects are observed. From these measurements, the g_{om} is determined to be 3.1 GHz/nm.

4.4 Acceleration sensing demonstration

Next we fix the drive wavelength and drive power (with laser instabilities less than ± 166 fm and ± 0.01-dB in 10-minutes) and examined the RF shift Δf_m under DC acceleration. To impart the DC acceleration, we mounted the device and vacuum setup onto a high-torque (Aerotech ADRS-200) rotary stage, as shown in Figure 4.4c. With optimized digital control and drive filter parameters (detailed in Methods), the stage provides a noise-equivalent input DC acceleration precision (in the $+y$ axis direction) down to ~ 20 ng. Figure 4.6a shows the measured backaction RF transduction in the pre-oscillation mode at 370 μW drive powers (f_m is ≈ 72 kHz in this measurement), from 6.7 μg to 1314.3 μg DC acceleration. Examining the Lorentzian RF lineshapes over the first 40 spectra (up to 154.8 μg), the RF frequency is observed to decrease by 48 Hz on-average over the measurement range, equivalent to a sensitivity S of 2.31 ± 0.32 μg/Hz (or a scale factor of 432.9 kHz/g). The uncertainty in the sensitivity S is determined from the least-squares regression estimate at 95% confidence interval.

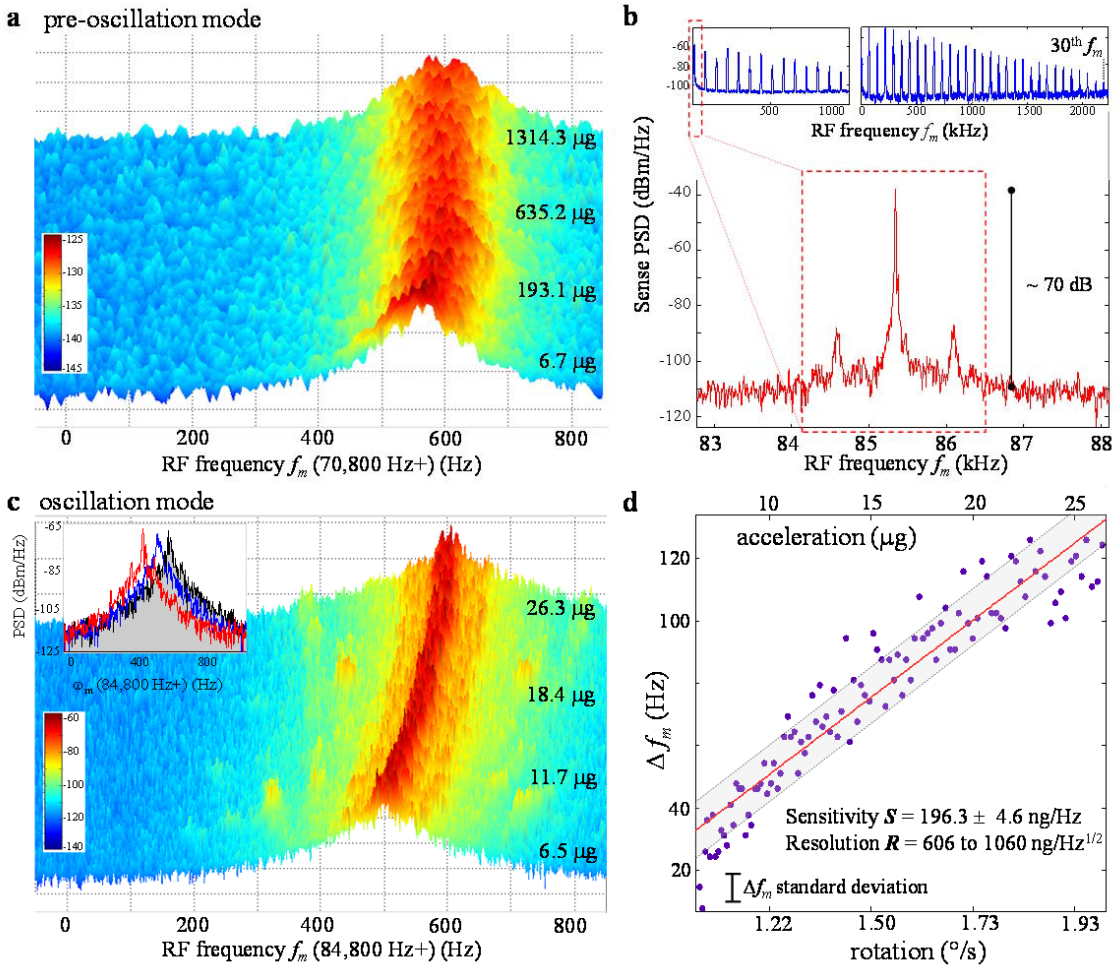

Figure 4.6 | DC acceleration signal detection. a, Backaction RF transduction at 370 μW drive powers under different accelerations, from 6.7 μg to 154.8 μg. Accelerations applied on the device pointing outwards from rotation center. Mechanical RF frequency decreases by 146 Hz. Each curve is offset by 2 dBm along *y*-axis for illustration. The overall fit to the detection sensitivity is at 2.31 μg/Hz. The resolution *R* is determined from R = 14.5 μg/Hz$^{1/2}$, pre-oscillation. **b,** DC accelerometer driven into self-sustained oscillation mode, with optical drive power exceeding the intrinsic mechanical damping, with up to 30th harmonic observed (top panel). Zoom-in of fundamental oscillation

mode at 85.3 kHz in this device, with the sidebands arising from coupling to out-of-plane modes. **c,** Tracked RF spectra of oscillation-mode DC acceleration sensing at ≈ 500 μW drive powers. Accelerations applied are from 6.5 μg to 26.3 μg pointing outwards from rotation center, with device mounted with reduction of slot width *s*. Mechanical resonance frequency increases by ≈ 98 Hz. Each curve is offset by 3 dBm along the power spectra for visual clarity. Inset: comparison RF spectra under 6.53, 14.68 and 26.34 μg (from left to right) respectively. **d,** RF resonance of the backaction transduction in oscillation-driven mode under different accelerations. Solid red line is the overall fit of the sensitivity *S* at 196.3 ng/Hz (shaded grey region represents the least-squares regression estimate at 95% confidence interval). The resolution is determined from the frequency noise density, and at ≈ 730 ng/$Hz^{1/2}$, at the thermal noise limit.

We consider the error from misalignment between the device mounting and the acceleration direction. If there is an error angle θ between the device mounting and acceleration direction, the acceleration error is $\Delta a = a - a' = (1 - \cos\theta)a$. Therefore, even if there is a ± 5° misalignment, the error in the acceleration estimate *Δa/a* would only be (1 - cos5°) or equivalently a ± 0.38% fixed (and consistent) offset in the imparted DC acceleration in the measurement. Figure 4.7 also shows the 2D RF spectra with the device mounted in the 180° direction opposite from Figure 4.6a (i.e. acceleration in the *–y* axis direction). The imparted DC acceleration ranges from 6.5 μg to 122.1 μg. The observed RF shift is estimated ≈ +120 Hz, through a numerical fit to the experimental data. The overall detection sensitivity is determined at ≈ 0.96 μg/Hz.

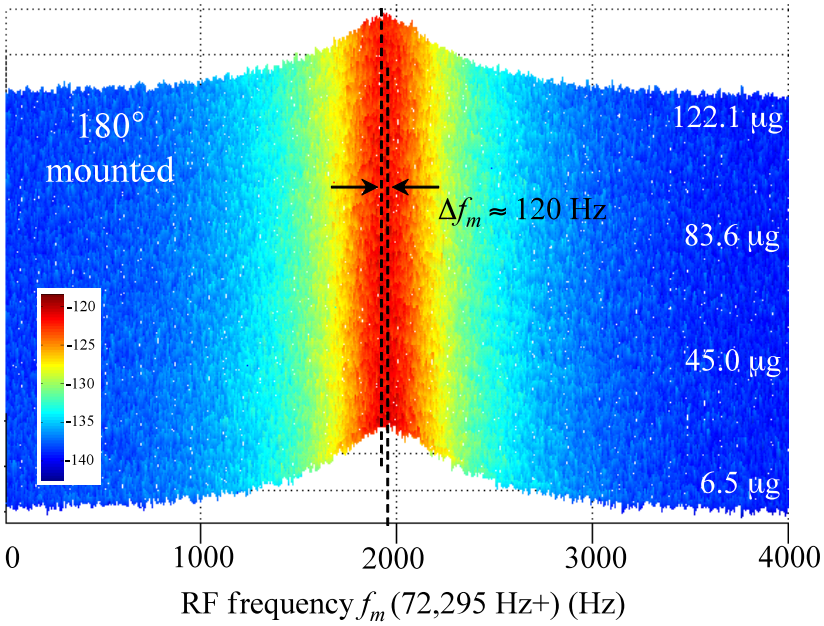

Figure 4.7 | Backaction RF transduction with device mounted in 180° direction without the oscillation mode, for acceleration in the *-y* direction. Imparted acceleration from 6.5 μg to 122.1 μg, with a corresponding RF shift of ≈ +120 Hz. The overall detection sensitivity is determined at ≈ 0.96 μg/Hz.

With the accelerometer resolution R defined as [78] where t_{meas} is the measurement time, we determined the minimal detectable RF shift based on thermal noise fluctuations, $\delta\omega_{thermal}$, from the displacement noise spectra (Figure 4.4a). From the measured displacement noise spectra we obtain $\delta\omega_{thermal}/2\pi$ as 19.9 Hz in 0.1 second integration and on-resonance. This corresponds to a DC acceleration resolution R of 91.3 $\mu g/Hz^{1/2}$, in pre-oscillation mode. We note that only the first 40 RF spectra (up to 154.8 μg) are used in the analysis to be well-within the linear dynamic range. We also measured other DC accelerometers with similar geometry but with the device mounted 180° opposite from Figure 4.6a (i.e. acceleration in the $-y$ axis direction); the RF frequency shift is observed in opposite direction under the same acceleration ranges.

4.5 Oscillation mode

4.5.1 Acceleration sensing in oscillation mode

We next drive the 5.6 ng DC accelerometer into oscillation mode as shown in Figure 4.6b, 4.6c and 4.6d, with drive powers above ≈ 477 μW. From the nonlinear optomechanical transduction, high-order harmonics (up to the 30th harmonic) of the fundamental resonance are observed above threshold [36], with two example spectra shown in the top insets of Figure 4.6b. In this device, the fundamental oscillation frequency is at 85.3 kHz (on another device), with the sidebands arising from coupling to out-of-plane modes. Note the ≈ 70-dB intensity peak-to-noise floor when in the self-induced regenerative oscillation regime, compared to ≈ 20-dB in the resonant (pre-

oscillation) mode. Figure 4.6c illustrates the tracked RF resonance shift under 6.53 μg to 26.34 μg DC acceleration, under ≈ 500 μW intracavity drive powers. We note the sizably larger RF shift at ≈ 98 Hz, compared to the pre-oscillation regime, even when measured over ≈ 50× smaller acceleration ranges (compared to Figure 4.6a). The inset of Figure 4.6c illustrates the spectra comparison (left to right) under 6.53, 14.68 and 26.34 μg respectively. To characterize the oscillator, we also measured the single-sideband phase noise which shows a -102-dBc/Hz noise floor at 10 kHz frequency offset from carrier.

Figure 4.6d summarizes the oscillator-mode DC acceleration measurement data over 102 datapoints, with the datapoints obtained from Lorentzian RF spectral peak. The fitted RF shift dependence shows a detection sensitivity S of 196.3 ± 4.6 ng/Hz (or equivalently, 5.02 ± 0.12 MHz/g). The improved sensitivity is due to the larger optomechanical stiffening at higher drive powers [$|a|^2$ in equation (1)], and matches our numerical modeling prediction of 140.3 ng/Hz. The DC accelerometer resolution is determined from the single-sideband phase noise S_φ and its corresponding frequency noise density S_f [78]. In the frequency range below 100 Hz, the frequency noise density can be up to ≈ 3.7 Hz/Hz$^{1/2}$ (from external noise; before reaching a minimum of 70 mHz/Hz$^{1/2}$ at 2.9 kHz offset). With the measured oscillator sensitivity of 196.3 ng/Hz, this corresponds to a measured DC acceleration noise density of ≈ 730 ng/Hz$^{1/2}$ when close to DC, ≈ 125.1× better than the pre-oscillation resonant mode. In addition to the ± 4.6 ng/Hz sensitivity regression estimate, the one standard deviation of the frequency shift fluctuations δf is also analyzed to be 9.78 Hz for 0.1 second integration, as also plotted as the grey region (and scale bar) of Figure 4.6d. This corresponds to an

oscillator DC acceleration resolution R of 606.2 ng/Hz$^{1/2}$. In oscillation mode, we also note the narrow (deeply sub-Hz) full-width half-maximum and large peak-to-noise floor ratio allows a minimal distinguishable RF shift (between two overlapping Lorentzian lineshapes) δf_{min_detect} much smaller than pre-oscillation $\delta f_{thermal}$.

4.5.2 Self-induced regenerative of oscillation modes

The minimum threshold power P_{th} [53] is given by:

$$P_{th} = \frac{\Omega_M}{Q_M}\frac{\hbar\omega_l\left(\Delta^2+(\kappa/2)^2\right)}{g_{OM}^2\kappa_{ex}\kappa}\left(\frac{1}{\left(\Delta-\Omega_M\right)^2+(\kappa/2)^2}-\frac{1}{\left(\Delta+\Omega_M\right)^2+(\kappa/2)^2}\right)^{-1}$$, where κ_{ex} is the optical cavity coupling rate and κ the total loss rate. With our experimental parameters, the theoretical threshold is ≈ 400 μW for a $g^*/2\pi$ of 325 kHz ($g_{om}/2\pi$) = 34.9 GHz/nm. When the input power is higher than parametric oscillation threshold, the proof mass will oscillate with its self-induced regenerative oscillation mode. We have observed up to 30th harmonic mode as shown in Figure 4.6b of the main text, with pump powers at ≈ 500 μW. The number of harmonic modes measured is bounded by the incident power and the detector bandwidth. Phase noise is a characterization of the oscillator [67] and Figure 4.8a illustrates the single sideband phase noise in the oscillator-mode DC accelerometer measured with an E5052 phase noise analyzer, following the Leeson model characteristics. Fitted with piecewise functions, the resulting corner frequency is 3.8 kHz and a $1/f^3$ region is observed at ~ 100 Hz to 1 kHz offsets. After the corner frequency the $1/f^2$ region arises from white frequency noise. At 10 kHz offset, the phase noise is determined down to about -102-dBc/Hz for the ~ 70 to 80 kHz

oscillator. Also, as shown in Figure 4.8b, we examine how the fundamental mode evolves with laser wavelength from 1553.5 nm to 1555.5 nm under input laser power of 1.6 mW, much higher than the oscillation threshold, with new harmonics appearing at this high power.

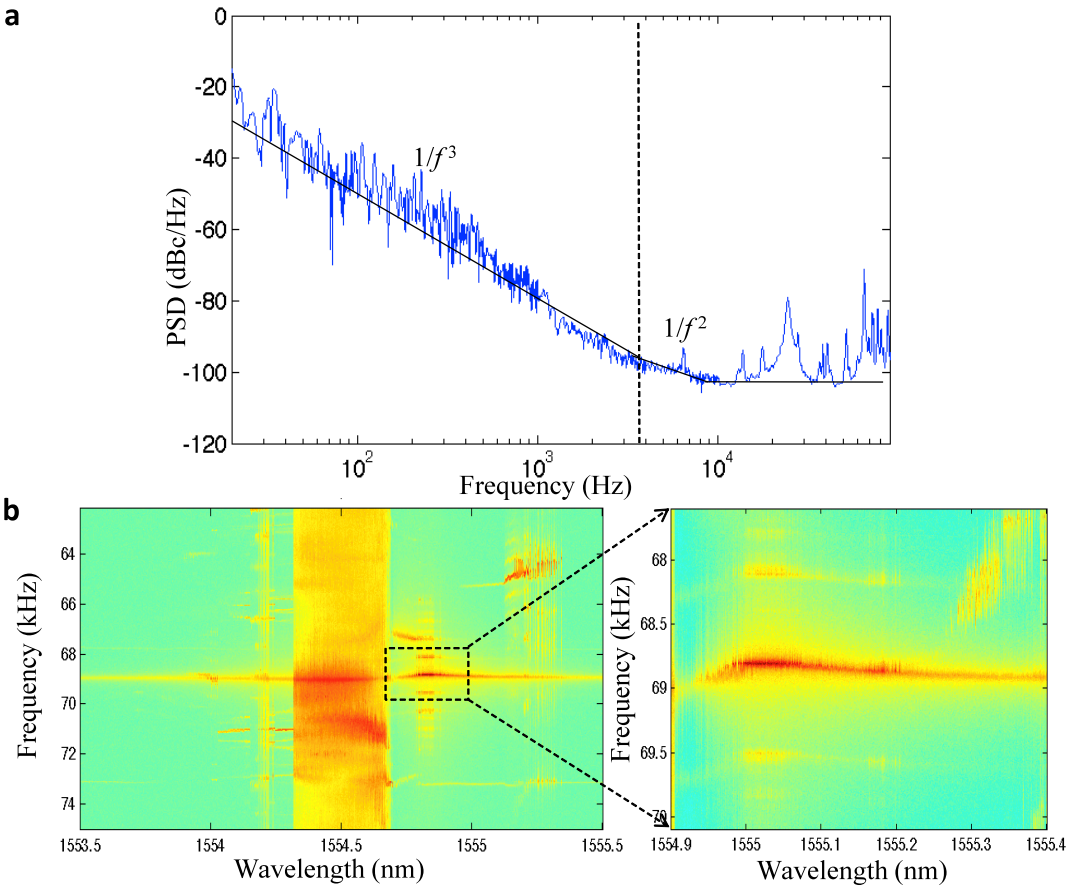

Figure 4.8 | Oscillation mode characteristics of optomechanical DC accelerometer. **a,** Phase noise measurement of the oscillation mode. The blue curve shows experimental data, which is fitted by using a piecewise function. The black lines indicate the $1/f^3$ dependence and the $1/f^2$ dependence. **b,** Evolution of the fundamental mode RF spectrum with swept pump laser wavelengths, at much higher input drive powers of 1.6 mW.

4.6 Specifications

Even in pre-oscillation mode, we emphasize that the detectable 3.05 Hz RF shift is equivalent to a 467 fm wavelength perturbation in the optical cavity resonance – this is difficult to resolve in the optical transmission spectra with optical spectrum analyzers and, if optical interferometers are used, requires good phase stability in the moving environment. Furthermore, we note that the observed oscillation acceleration sensitivity (730 ng/$Hz^{1/2}$) corresponds to the force detection – through the optical drive and RF readout – of 40.1 aN/$Hz^{1/2}$. In our measurements, for maximal sensitivity to the external DC acceleration, we tune the drive and readout laser wavelength to the slot-cavity resonance. In our measurements, the cavity slot direction is aligned perpendicular to the rotation radius, allowing the imparted centrifugal force to be in the *y*-direction onto the proof mass (the alignment error is negligible and, even for a ± 5° error, contributes only a ± 0.38% fixed offset in the imparted force measurement). Furthermore, we note that the estimated instabilities of drive wavelength (± 166 fm) over 10-minutes contribute to only a ± 5% uncertainty in the DC acceleration resolution; for long-term measurements this uncertainty can be readily improved with more stable drive lasers. We also note that the coupled intracavity power is monitored to account for any coupling drifts or power fluctuations in the rotation measurements, and a polarization-maintaining tapered fiber serves as the input/output coupling fiber through vacuum chamber to avoid any polarization shifts during the imparted rotation and acceleration. In addition, we emphasize that our optomechanical *resonant* readout approach for DC accelerometer

sensing has negligible zero-offset error (in contrast to other resistive or piezoresistive *LC*-circuit resonant accelerometers) since the readout is always based on the relatively-insensitive mechanical eigenfrequency.

Without optomechanical stiffening, the accelerometer resolution, or the noise equivalent acceleration (NEA), is solely represented by the mechanical domain parameters and described by thermal Brownian noise from the equipartition theorem as $a_{th} = \sqrt{\frac{4k_B T\omega_m}{mQ_m}}$. With the large mass oscillator and high drive powers, the measured oscillator linewidth is consistently determined to be instrument-limited at the 50 mHz or less (analyzer resolution bandwidth). From the measured single sideband phase noise or the derived oscillator displacement through optical intensity modulation [35], the converted intrinsic linewidth is estimated between 2 to 5 mHz (at 1.5 kHz to 9 kHz offset). This corresponds to be theoretical thermally-limited oscillator DC acceleration at ≈ 700 ng/Hz$^{1/2}$, supporting that our resolution and sensitivity measurements are close to, or at, the thermal limit. Optical noise arising from quantum backaction noise a_{BA} can contribute to the noise [50]. In our oscillator design and implementation parameters, the resulting a_{BA} limit is estimated at 200 ng/Hz$^{1/2}$. We note that, with this RF transduction readout approach instead of solely the optical intensity transmission readout, optical shot noise and photodetector shot noise do not contribute significantly to the fundamental limit in our readout scheme, allowing our measured acceleration resolutions (between 606 and 730 ng/Hz$^{1/2}$ in oscillation mode) within 3.0× to 3.7× of the quantum backaction limit.

Figure 4.9 shows the resulting measured frequency shift Δf_m over linewidth ratio, comparing the oscillation and pre-oscillation resonant modes. Note the ≈ 16× oscillation sensitivity enhancement is only bounded by the instrumentation resolution-bandwidth of the oscillator linewidth. Our single model for both resonant and oscillation mode frequency shifts are shown in the dashed lines and match our measurements over four orders-of-magnitude. The remaining deviations of the modeled sensitivity from the measurements likely arise from a residual ≈ 25% over-estimate in the optical resonance shift per displacement in the finite-difference time-domain simulations. Figure 4.9b summarizes the DC detection resolution versus bandwidth (or linewidth), over four independent devices. To support the accelerometer demonstration, we determine the linear dynamic range experimentally from the 1 dB compression point (20% deviation from linear dependence) as 23.5 dB, which compares well with the ≈ 24.8 dB in theory. The linearity deviation arises primarily from the nonlinear dependence of the optical resonance on the slot width s. In addition, to further improve the sensitivity and resolution, self-reference noise cancellation [79] or thermal stabilization through multiply-resonant optomechanical oscillators [80] can be pursued.

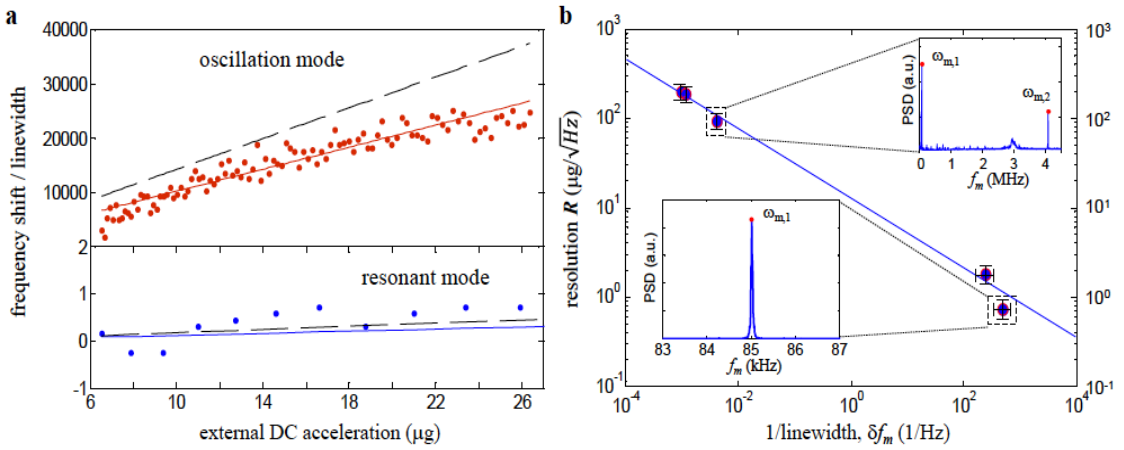

Figure 4.9 | Oscillation mode sensitivity enhancement and dynamic range. a, Detection at the μg/Hz$^{1/2}$ and lower levels. The frequency shift-over-linewidth ratio is increased to more than 10^4 in oscillation-driven mode, compared to ~1 in non-oscillation resonant mode detection, and bounded only by the instrumentation resolution bandwidth. Dashed lines are the theoretical model while the solid lines are the data best-fits. **b,** Summary of resolution versus optomechanical cavity linewidth. 4 independent devices are measured in this panel, with one repeated device for different pump conditions. Inset: power spectral density of the investigated modes.

In addition, the effects of pump laser wavelength instability and coupled intracavity energy instability can be considered through equation (1) of the main text. The tunable Santec laser (TSL-510C) has specified wavelength and power instabilities of less than ± 166 fm and ± 0.0016 dB in 10-minutes, without feedback [30] control. The wavelength instabilities translate into a ± 5% uncertainties for the measured acceleration. The low optical Q (and relatively large optical linewidth of ≈ 1 nm) reduces the sensitivity to pump wavelength fluctuations, although wavelength feedback locking to an external frequency reference can further drive down this uncertainty. The ± 0.01-dB power instability is negligible in the RF readout.

4.6.1 DC accelerometer sensitivity

The proof mass supported with thin tethers acts as an oscillator. The sensitivity of a resonant accelerometer is defined as frequency shift responding to unit acceleration change, $\Delta f / \Delta a$. Acceleration sensitivity in terms of displacement can be calculated from mechanical susceptibility, $|x(\omega)|/a(\omega) = |\chi(\omega)| = \left|\omega_m^2 - \omega^2 + i|\omega\omega_m|/Q_m\right|^{-1}$. The oscillator operates at its resonant frequency ω_m. Therefore, $|x(\omega)|/a(\omega) = |\chi(\omega)| = Q_m/\omega_m^2 = 104\, fm/\mu g$ The cavity resonance frequency is a function of slot width x, which is used to detect the position of the proof mass. Fitting the photonic crystal slot cavity simulation results, we obtain optical resonance frequency ω dependence as , where x represents slot width in units of nm. Resonator frequency shift with different detuning due to optomechanical stiffness effect is obtained from the

curve slope at zero detuning, which is $\Delta f / \Delta\lambda$ = 450 Hz / 70 pm for pre-oscillation mode and $\Delta f / \Delta\lambda$ = 2,640 Hz / 43 pm for oscillation mode. Therefore, the sensitivity of the accelerometer is $\Delta f / \Delta a = (\Delta f / \Delta\lambda) \cdot (\Delta\lambda / \Delta x) \cdot (|x(\omega_m)| / a(\omega_m))$ = 776 kHz/g (or 1.26 μg/Hz) in pre-oscillation mode and 7.13 MHz/g (or 140.3 ng/Hz) in oscillation mode.

4.6.2 DC accelerometer resolution

The DC accelerometer resolution is defined by its noise equivalent acceleration. This noise comes primarily from thermal Brownian motion. Displacement noise from thermal Brownian motion at DC is: $x = \sqrt{S_{xx}^{th}} = \chi(0)\sqrt{S_{aa}^{th}} = a_{th}/\omega_m^2 = 210\, fm/\sqrt{Hz}$ Noise from the thermal Brownian motion then corresponds to a noise-equivalent acceleration of $a_{th} = \sqrt{\frac{4k_B T\omega_m}{mQ_m}}$, derived from the equipartition theorem. With the large 5.6 ng mass, the oscillator demonstrates a linewidth consistently limited only by the resolution bandwidth of the spectrum analyzer (50 mHz or less; or an equivalent mechanical Q_m in excess of 1.7×10^6). From the measured single sideband phase noise, the derived intrinsic linewidth is estimated between 2 to 5 mHz. For the oscillator $\omega_m/2\pi$ at 85.3 kHz, this gives a thermal-noise limited acceleration resolution at ≈ 700 ng/Hz$^{1/2}$.

Optical noise arising from quantum backaction noise a_{BA} exerts a random force on the mechanical oscillator. The acceleration noise created by optomechanical backaction is: $S_{aa}^{BA} = 2\frac{(\hbar g_{om})^2}{m^2} n_c \frac{4}{\kappa}$ where n_c is the cavity photon number. When the input power is 370 μW, the photon number in the cavity is 10,400 and the above

equation results in a noise equivalent acceleration from quantum backaction as:

$$a_{BA} = \sqrt{S_{aa}^{BA}} = \sqrt{2\frac{\left(\hbar g_{om}\right)^2}{m^2} n_c \frac{4}{\kappa}} = 200ng/Hz^{1/2}$$

Frequency inaccuracy from the spectrum analyzer also brings noise to the acceleration measurement. Readout frequency accuracy of the Agilent PSA E4448a is determined by the sum of several error sources, including frequency reference inaccuracy, span error, and resolution bandwidth (RBW) center-frequency error. Frequency reference accuracy is ±[(time since last adjustment × aging rate) + temperature stability + calibration accuracy] = ±[1×10^{-7}/year × 1 year + 1×10^{-8} + 7×10^{-8}] = $\pm1.8 \times 10^{-7}$. For the measurement, the span error is 0.25% × span = 0.25% × 400 Hz = 1 Hz and RBW error is 5% × RBW = 5% × 1 Hz = 50 mHz. Residual error is 2 Hz. The sum of the above is 3.05 Hz, which gives the total readout frequency inaccuracy.

4.6.3 Detection dynamic range

We also examined the linear response range of the accelerometer. Figure 4.10a illustrates the computed linear response dynamic range from optomechanical stiffening. Along with the increase of acceleration signal, frequency shift deviates from linear behavior due to the nonlinear dependence of the optical resonance on the slot width *s*. To compare with measurements, an experimental standard deviation of the RF shift fluctuations are defined onto the modeling as shown which illustrates a ≈ 24.8 dynamic range. We also calculate the dynamic range versus stored energy for devices with different proof masses. As illustrated in Figure 4.10b, linear dynamic range increase with stored energy

but decreases with larger proof mass. The corresponding experimental dynamic range is determined to be 23.5 dB and illustrated in Figure 4.10b, matching well with our numerical modeling predictions.

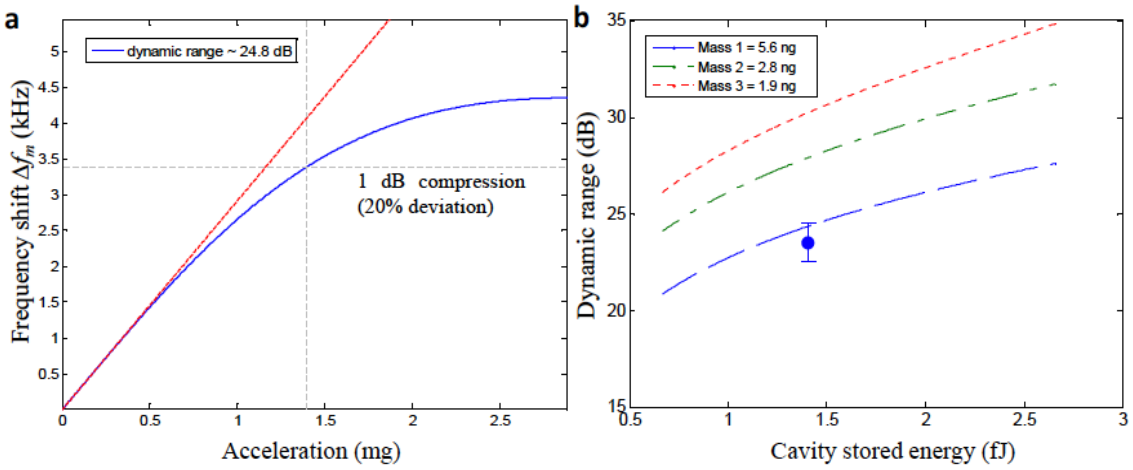

Figure 4.10 | Dynamic range parameter space of the DC optomechanical accelerometer. a, Modeled primary DC accelerometer design with ≈ 24.8 dB dynamic range, , defined as 20% deviation (1 dB compression point) from linear regime. Dashed red line is the linear dependence, and blue line is the modeled Δf_m for large imparted accelerations. **b,** Dynamic range for increasing optical pump power (cavity stored energy) and different proof masses. The experimental dynamic range from the measurement data analysis is determined as 23.5 dB with the represented solid blue datapoint.

4.7 Conclusion

We have demonstrated for the first time a DC-response optomechanical accelerometer, driven into the oscillation mode for enhanced noise-equivalent acceleration in gravimetry. In pre-oscillation mode, the optomechanical drive and readout shows a sensitivity of 2.31 μg/Hz. Driven into self-regenerative optomechanical oscillation modes with sub-10-mHz linewidths, the oscillator demonstrates a DC acceleration resolution down to 730 ng/$Hz^{1/2}$, at the thermal noise limit and ≈ 3.7× the quantum backaction noise. The mesoscopic room-temperature implementation with RF optomechanical transduction and readout provides a platform towards low-noise precision sensing of gravity, navigation, and metrology.

Bibliography

[1] H. Muller, A. Peters, and S. Chu, A precision measurement of the gravitational redshift by the interference of matter waves, *Nature* 463, 926 (2010).

[2] G. Rosi, F. Sorrentino, L. Cacciapuoti, M. Prevedelli, and G. M. Tino, Precision measurement of the Newtonian gravitational constant using cold atoms, *Nature* 510, 518 (2014).

[3] N. Malossi, Q. Bodart, S. Merlet, T. Lévèque, A. Landragin, and F. Pereira Dos Santos, Double diffraction in an atomic gravimeter, *Phys. Rev. A* 81, 013617 (2010).

[4] S. Schreppler, N. Spethmann, N. Brahms, T. Botter, M. Barrios, D. M. Stamper-Kurn, Optically measuring force near the standard quantum limit, *Science* 344, 1486 (2014).

[5] F. G. Cervantes, L. Kumanchik, J. Pratt, and J. Taylor, High sensitivity optomechanical reference accelerometer over 10 kHz, *Appl. Phys. Lett.* 104, 221111 (2014).

[6] A. G. Krause, M. Winger, T. D. Blasius, Q. Lin, and O. Painter, A high-resolution microchip optomechanical accelerometer, *Nature Photonics.* 6, 768 (2012).

[7] C.-H. Liu and T. W. Kenny, A high-precision, wide-bandwidth micromachined tunneling accelerometer, *J. Micromechanical Sys.* 10, 425 (2001).

[8] A. A. Seshia, M. Palaniapan, T. A. Roessig, R. T. Howe, R. W. Gooch, T. R. Schimert, and S. Montague, A vacuum packaged surface micromachined resonant

accelerometer, *J. Micromechanical Sys.* 11, 784 (2002); T. A. Roessig, R. T. Howe, A. P. Pisano, and J. H. Smith, Surface micromachined resonant accelerometer, *Proc. Solid-State Sensors and Actuators* (Transducers ’97), 859 (1997).

[9] K. H.-L. Chau, S. R. Lewis, Y. Zhao, R. T. Howe, S. F. Bart, and R. G. Marcheselli, An integrated force-balanced capacitive accelerometer for low-g applications, *Proc. Solid-State Sensors and Actuators* (Transducers’95), 593 (1995).

[10] C. Yeh and K. Najafi, CMOS interface circuitry for a low-voltage micromachined tunneling accelerometer, *J. Microelectromech. Syst.* 7, 6 (1998).

[11] F. Rudolf, A. Jornod, J. Bergqvist, and H. Leuthold, Precision accelerometer with μg resolution, *Sensors and Actuators* A21–A23, 297 (1990).

[12] R. L. Kubena, G. M. Atkinson, W. P. Robinson, and F. P. Stratton, A new miniaturized surface micromachined tunneling accelerometer, *IEEE Electron Device Lett.* 17, 306 (1996).

[13] D. L. DeVoe and A. P. Pisano, A fully surface-micromachined piezoelectric accelerometer, *Proc. Solid-State Sensors and Actuators* (Transducers’97), 1205 (1997).

[14] A. Partridge, J. K. Reynolds, B.W. Chui, E. M. Chow, A. M. Fitzgerald, L. Zhang, S. R. Cooper, and T. W. Kenny, A high performance planar piezoresistive accelerometer, *Proc. Solid-State Sensors and Actuators* (Hilton Head ’98), 59 (1998).

[15] A. M. Leung, J. Jones, E. Czyzewska, J. Chen, and B. Woods, Micromachined accelerometer based on convection heat transfer, *Proc. IEEE Micro Electro Mechanical Systems* (MEMS ’98), 627 (1998).

[16] K. L. Ekinci and M. L. Roukes, Nanoelectromechanical systems, *Rev. Sci. Instr.* 76,

061101 (2005).

[17] X. Zou, P. Thiruvenkatanathan, and A. A. Seshia, A seismic-grade resonant MEMS accelerometer, *J. Microelectromech. Syst.* 23, 768 (2014).

[18] A. N. Cleland and M. L. Roukes, Noise processes in nanomechanical resonators, *J. Appl. Phys.* 92, 2758 (2002).

[19] S. D. Senturia, *Microsystem Design*, Springer, 2005.

[20] K.L. Ekinci, Y.T. Yang and M.L. Roukes, Ultimate limits to inertial mass sensing based upon nanoelectromechanical systems, *J. Appl. Phys.* 95, 2682 (2004).

[21] S. Tadigadapa and K. Mateti, Piezoelectric MEMS sensors: state-of-the-art and perspectives, *Meas. Sci. Technol.* 20, 092001 (2009).

[22] C. Acar and A. M. Shkel, Experimental evaluation and comparative analysis of commercial variable-capacitance MEMS accelerometers, *J. Micromech. Microeng.* 13, 634 (2003).

[23] W.-T. Park, A. Patrick, R. N. Chandler, V. Ayanoor-Vitikkate, G. Yama, M. Lutz, and T. W. Kenney, Encapsulated submillimeter piezoresistive accelerometers, *J. Micromechanical Sys.* 15, 507 (2006).

[24] S. C. Masmanidis, R. B. Karabalin, I. De Vlaminck, G. Borghs, M. R. Freeman, and M. L. Roukes, Multifunctional nanomechanical systems via tunably coupled piezoelectric actuation, *Science* 317, 780 (2007).

[25] C.-H. Liu and T. W. Kenny, A high-precision, wide-bandwidth micromachined tunneling accelerometer, *J. Micromechanical Sys.* 10, 425 (2001).

[26] H. Miao, K. Srinivasan, and V. Aksyuk, A microelectromechanically controlled

cavity optomechanical sensing system, *New. J. Phys.* 14, 075015 (2012).

[27] D. N. Hutchison and S. A. Bhave, Z-axis optomechanical accelerometer, *Proc. IEEE MEMS*, Paris, France (2012).

[28] J. Zheng, Y. Li, N. Goldberg, M. McDonald, A. Hati, M. Lu, S. Strauf, T. Zelevinsky, D. A. Howe, and C. W. Wong, Feedback and harmonic locking of slot-type optomechanical oscillators to external low-noise reference clocks, *Appl. Phys. Lett.* 102, 141117 (2013).

[29] Y. Li, J. Zheng, J. Gao, J. Shu, M. S. Aras, and C. W. Wong, Design of dispersive optomechanical coupling and cooling in ultrahigh-Q/V slot-type photonic crystal cavities, *Optics Express* 18, 23844 (2010).

[30] M. Li, W. H. P. Pernice, and H. X. Tang, Broadband all-photonic transduction of nanocantilevers, *Nature Nano* 4, 377 (2009).

[31] A. K. Naik, M. S. Hanay, W. K. Hiebert, X. L. Feng, and M. L. Roukes, Towards single-molecule nanomechanical mass spectrometry, *Nature Nano.* 4, 445 (2009).

[32] A. D. O'Connell, M. Hofheinz, M. Ansmann, R. C. Bialczak, M. Lenander, E. Lucero, M. Neeley, D. Sank, H. Wang, M. Weides, J. Wenner, J. M. Martinis, and A. N. Cleland, Quantum ground state and single-phonon control of a mechanical resonator, *Nature* 464, 697 (2010).

[33] J. Chan, T. P. M. Alegre, A. H. Safavi-Naeini, J. T. Hill, A. Krause, S. Gröblacher, M. Aspelmeyer, and O. Painter, Laser cooling of a nanomechanical oscillator into its quantum ground state, *Nature* 478, 89 (2011).

[34] Y.-C. Liu, Y.-F. Xiao, X. Luan, and C. W. Wong, Dynamic dissipative cooling of a

mechanical oscillator in strong-coupling optomechanics, *Phys. Rev. Lett.* 110, 153606 (2013).

[35] M. Hossein-Zadeh, H. Rokhsari, A. Hajimiri, and K. J. Vahala, Characterization of a radiation-pressure-driven micromechanical oscillator, *Phys. Rev. A* 74, 023813 (2006).

[36] X. Luan, Y. Huang, Y. Li, J. F. McMillan, J. Zheng, S.-W. Huang, P.-C. Hsieh, T. Gu, D. Wang, A. Hati, D. A. Howe, G. Wen, M. Yu, G. Lo, D.-L. Kwong, and C. W. Wong, An integrated low phase noise radiation-pressure-driven optomechanical oscillator chipset, *Sci. Rep.* 4, 6842 (2014).

[37] K. Vahala, M. Hermann, S. Knünz, V. Batteiger, G. Saatho***ff***, T. W. Hänsch, and Th. Udem, A phonon laser, *Nature Physics* 5, 682 (2009).

[38] S. Weis, R. Rivière, S. Deléglise, E. Gavartin, O. Arcizet, A. Schliesser, and T. J. Kippenberg, Optomechanical induced transparency, *Science* 330, 1520 (2010).

[39] C. Dong, V. Fiore, M. Kuzyk, and H. Wang, Optomechanical dark mode, *Science* 338, 1609 (2012).

[40] S. Kolkowitz, A. C. Bleszynski-Jayich, Q. P. Unterreithmeier, S. Bennett, P. Rabl, J. G. E. Harris, M. Lukin, Coherent sensing of a mechanical resonator with a single-spin qubit, *Science* 335, 6706 (2012).

[41] T. A. Palomaki, J. W. Harlow, J. D. Teufel, R. W. Simmonds, and K. W. Lehnert, Coherent state transfer between itinerant microwave fields and a mechanical oscillator, *Nature* 495, 210 (2013).

[42] J. C. Sankey, C. Yang, B. M. Zwickl, A. M. Jayich, and J. G. E. Harris, Strong and tunable nonlinear optomechanical coupling in a low-loss system, *Nature Physics* 6, 707

(2010).

[43] G. Anetsberger, E. Gavartin, O. Arcizet, Q. P. Unterreithmeier, E. M. Weig, M. L. Gorodetsky, J. P. Kotthaus, and T. J. Kippenberg, Measuring nanomechanical motion with an imprecision below the standard quantum limit, *Phys. Rev. A* 82, 061804(R) (2010).

[44] H. Miao, K. Srinivasan, and V. Aksyuk, A microelectromechanically controlled cavity optomechanical sensing system, *New. J. Phys.* 14, 075015 (2012).

[45] M. Li, W. H. P. Pernice, and H. X. Tang, Broadband all-photonic transduction of nanocantilevers, *Nature Nano.* 4, 377 (2009).

[46] E. Gavartin, P. Verlot, and T. J. Kippenberg, A hybrid on-chip optomechanical transducer for ultrasensitive force measurements, *Nature Nano.* 7, 509 (2012).

[47] T. Bagci, A. Simonsen, S. Schmid, L. G. Villanueva, E. Zeuthen, J. Appel, J. M. Taylor, A. Sørensen, K. Usami, A. Schliesser, and E. S. Polzik, Optical detection of radio waves through a nanomechanical transducer, *Nature* 507, 81 (2014).

[48] D. N. Hutchison and S. A. Bhave, Z-axis optomechanical accelerometer, *Proc. IEEE MEMS*, Paris, France, 2012.

[49] F. G. Cervantes, L. Kumanchik, J. Pratt, and J. Taylor, High sensitivity optomechanical reference accelerometer over 10 kHz, *Appl. Phys. Lett.* 104, 221111 (2014).

[50] A. G. Krause, M. Winger, T. D. Blasius, Q. Lin, and O. Painter, A high-resolution microchip optomechanical accelerometer, *Nature Photonics.* 6, 768 (2012).

[51] J. Gao, J. F. McMillan, M.-C. Wu, J. Zheng, S. Assefa, and C. W. Wong,

Demonstration of an air-slot mode-gap confined photonic crystal slab nanocavity with ultrasmall mode volumes, *Appl. Phys. Lett.* 96, 051123 (2010).

[52] Y. Li, J. Zheng, J. Gao, J. Shu, M. S. Aras, and C. W. Wong, Design of dispersive optomechanical coupling and cooling in ultrahigh-Q/V slot-type photonic crystal cavities, *Optics Express* 18, 23844 (2010).

[53] M. Aspelmeyer, T. J. Kippenberg, and F. Marquardt, Cavity optomechanics, arXiv:1303.0733v1 (2013).

[54] I. Favero and K. Karrai, Optomechanics of deformable optical cavities, *Nature Photonics* 3, 201 (2009).

[55] D. V. Thourhout and J. Roels, Optomechanical device actuation through the optical gradient force, *Nature Photonics* 4, 211 (2010).

[56] M. Li, W. H. P. Pernice, C. Xiong, T. Baehr-Jones, M. Hochberg, and H. X. Tang, Harnessing optical forces in integrated photonic circuits, *Nature* 456, 480 (2008).

[57] G. Bahl, M. Tomes, F. Marquardt, T. Carmon, Observation of spontaneous Brillouin cooling, *Nature Physics* 8, 203 (2012).

[58] E. Gavartin, P. Verlot, and T. J. Kippenberg, Stabilization of a linear nanomechanical oscillator to its thermodynamic limit, *Nature Comms.* 4, 2860 (2013).

[59] T. Rocheleau, T. Ndukum, C. Macklin, J. B. Hertzberg, A. A. Clerk, and K. C. Schwab, Preparation and detection of a mechanical resonator near the ground state of motion, *Nature* 463, 72 (2010).

[60] J. D. Teufel, T. Donner, D. Li, J. W. Harlow, M. S. Allman, K. Cicak, A. J. Sirois, J. D. Whittaker, K. W. Lehnert, and R. W. Simmonds, Sideband cooling of

micromechanical motion to the quantum ground state, *Nature* 475, 359 (2011).

[61] A. Schliesser, R. Riviere, G. Anetsberger, O. Arcizet, and T. J. Kippenberg, Resolved-sideband cooling of a micromechanical oscillator, *Nature Physics* 4, 415 (2008).

[62] S. Tallur, S. Sridaran, and S. A. Bhave, A monolithic radiation-pressure driven, low phase noise silicon nitride opto-mechanical oscillator, *Opt. Express* 19, 24522–9 (2011).

[63] A. B. Matsko, A. A. Savchenkov, and L. Maleki, Stability of resonant opto-mechanical oscillators, *Optics Express* 20, 16234 (2012).

[64] P. B. Deotare, I. Bulu, I. W. Frank, Q. Quan, Y. Zhang, R. Ilic and M. Loncar, All optical reconfiguration of optomechanical filters, *Nature Comm.* 3, 846 (2012).

[65] J. Li, H. Lee, and K. J. Vahala, Microwave synthesizer using an on-chip Brillouin oscillator, *Nature Comms.* 4, 2097 (2013).

[66] T. Beyazoglu, T. O. Rocheleau, K. E. Grutter, A. J. Grine, M. C. Wu, and C. T.-C. Nguyen, A multi-material *Q*-boosted low phase noise optomechanical oscillator, *Proceedings of IEEE Int. Conf. MEMS* 1193 (2014).

[67] X. Luan, Y. Huang, Y. Li, J. F. McMillan, J. Zheng, S.-W. Huang, P.-C. Hsieh, T. Gu, D. Wang, A. Hati, D. A. Howe, G. Wen, M. Yu, G. Lo, D.-L. Kwong, and C. W. Wong, An integrated low phase noise radiation-pressure-driven optomechanical oscillator chipset, *Sci. Rep.* 4, 6842 (2014).

[68] K. Fong, M. Poot, X. Han, H. Tang, Phase noise of self-sustained optomechanical oscillators, *Phys. Rev. A* 90, 023825 (2014).

[69] A. H. Safavi-Naeini, T. P. Mayer Alegre, J. Chan, M. Eichenfield, M. Winger, Q.

Lin, J. T. Hill, D. E. Chang, and O. Painter, Electromagnetically induced transparency and slow light with optomechanics, *Nature* 472, 69 (2011).

[70] S. Camerer, M. Korppi, A. Jöckel, D. Hunger, T. W. Hänsch, and P. Treutlein, Realization of an optomechanical interface between ultracold atoms and a membrane, *Phys. Rev. Lett.* 107, 223001 (2011).

[71] J. Bochmann, A. Vainsencher, D. D. Awschalom, and A. N. Cleland, Nanomechanical coupling between microwave and optical photons, *Nature Phys.* 9, 712 (2013).

[72] A. H. Safavi-Naeini, S. Groblacher, J. T. Hill, J. Chan, M. Aspelmeyer, and O. Painter, Squeezed light from a silicon micromechanical resonator, *Nature* 500, 185 (2013).

[73] B. D. Clader, Quantum networking of microwave photons using optical fibers, *Phys. Rev. A* 90, 012324 (2014).

[74] A. F. Oskooi, D. Roundyb, M. Ibanescua, P. Bermelc, J.D. Joannopoulosa, and S. G. Johnson, Meep: A flexible free-software package for electromagnetic simulations by the FDTD method, *Computer Physics Communications* 181, 687 (2010).

[75] S. G. Johnson, M. Ibanescu, M. A. Skorobogatiy, O. Weisberg, J. D. Joannopoulos, and Y. Fink, Perturbation theory for Maxwell's equations with shifting material boundaries, *Phys. Rev. E* 65, 066611 (2002).

[76] H. A. Haus, *Waves and Fields in Optoelectronics*, Prentice Hall, Englewood Cliffs, New Jersey (1984).

[77] J. Zheng, Y. Li, M. S. Aras, A. Stein, K. L. Shepard, and C. W. Wong, Parametric

optomechanical oscillations in two-dimensional slot-type high-*Q* photonic crystal cavities, *Appl. Phys. Lett.* 100, 211908 (2012).

[78] C. Comi, A. Corigliano, G. Langfelder, A. Longoni, A. Tocchio, and B. Simoni, A resonant microaccelerometer with high sensitivity operating in an oscillating circuit, *J. Micromechanical Sys.* 19, 1140 (2010).

[79] Y. Zhao, Dalziel J. Wilson, K.-K. Ni, and H. J. Kimble, Suppression of extraneous thermal noise in cavity optomechanics, *Optics Express* 20, 3586 (2012).

80[30] A. B. Matsko, A. A. Savchenkov, V. S. Ilchenko, D. Seidel, and L. Maleki, Self-referenced stabilization of temperature of an optomechanical microresonator, *Phys. Rev. A* 83, 021801(R) (2011).

Chapter 5

A Broadband On-chip OSA Based on the Vernier Effect of Dual Ring Resonators

5.1 Introduction

Integrated optical spectrometers have received increased attention in recent years due to their inherent advantages and broad potential applications to wavelength division multiplexed optical communications, as well molecular and biological detection and identification.

Integrated optical spectrometers with different configurations have been realized, including examples based on arrayed-waveguide gratings [1, 2] and diffractive grating spectrometers [3]. Since the spectral resolution is linked to the number of grooves or waveguides, the resolution of these spectrometers is limited by the size of the dispersive region. If such spectrometers are to be integrated in lab-on-chip devices, reducing the footprint of the spectrometers is an important requirement. A recent demonstration with decreased configuration area used a diffractive grating spectrometer combined with thermally tunable micro-ring resonators [4]. However, the resolution and channel counts of these grating-based designs are still restricted by the number of waveguides.

Previous designs of array-based micro-spectrometers with narrow-band spectral responses include a filter array with Fabry-Perot cavities [5, 6], a micro-donut resonators array [7] and an array of photonic crystal cavities [8-11]. The bandwidths of these configurations are strictly limited by the free spectral range (FSR) of individual elements and each element only represents one channel. To obtain high channel counts

requires a large number of high quality optical elements, which greatly increases fabrication complexity. For some of these architectures, each channel requires a single photodetector to measure the output from the spectral component simultaneously. By the high count of photodetectors necessary to support these systems, integration complexity likewise scales.

In this chapter, we propose and demonstrate a new on-chip optical spectrum analyzer (OSA) configuration based on the Vernier Effect of the two cascaded high quality tunable ring resonators. The FSR of the resonator can be largely extended by the optical Vernier effect. An FSR up to 100 GHz has been reported with dual ring filters [12]. Applications of the dual ring systems, such as biosensors [13], have also been reported. In this work, the device, inclusive of the two cascaded resonators, exhibits an FSR of around 70 nm. To make a compact on-chip OSA system, we also integrate an on-chip Germanium photodetector to measure the optical power and send the data to be processed. An on-chip Mach-Zehnder modulator (MZM) is employed to conduct a phase sensitive detection. The device performance metrics in combination show significant improvements compared to the state-of-the-art with the achievement of small footprint, wide wavelength range as well as sub-nanometer resolution. Its compact and simple configuration, compared with other spectrometers, reduces fabrication complexity. This on-chip OSA could be attractive for implementation in photonic integrated circuits (PICs) and optical communication systems.

5.2 Device design and experimental setup

Our broadband on-chip OSA is composed of two cascaded ring resonators. Each individual ring resonator has a comb-like transmission spectrum with peaks at its resonance wavelengths. The FSRs of the two rings, FSR_1 and FSR_2, are designed to be different by choosing different radii for the first and second ring, respectively. Heaters are integrated with the ring resonators to tune the resonant frequency, since the optical path length of the heated waveguide changes due to the temperature dependence of the refractive index [14].

To derive the period, the resonances of the ring resonator with the shorter optical roundtrip are noted λ_{short}, and the resonances of the resonator with the longer optical roundtrip as λ_{long}. Suppose at wavelength λ_0 two resonances of the respective resonators coincide. The other resonance wavelengths of both resonators are

$$\lambda_{short,k} = \lambda_0 + k \times \mathrm{FSR}_{\mathrm{short}} \tag{1}$$

$$\lambda_{long,k} = \lambda_0 + l \times \mathrm{FSR}_{\mathrm{long}} \tag{2}$$

where k and l are integers. The signal appears again in the transmission spectrum when the two resonances coincide again. This occurs for an index k = K for which $\lambda_{short,K} = \lambda_{long,K+N}$, plug into equation (1) and (2) we have

$$\frac{K}{N} = \frac{FSR_{long}}{\left(FSR_{short} - FSR_{long}\right)} \tag{3}$$

K and N are the minimum integers that satisfy the equation. Equivalently,

$$\text{Period} = \lambda_{short,K} - \lambda_0 = K \times FSR_{short}$$

$$= \frac{N \times FSR_{short} \times FSR_{long}}{\left(FSR_{short} - FSR_{long}\right)} \quad (4)$$

The FSR of two cascaded ring resonators is then given by the least common multiple of FSR_1 and FSR_2.

For the on-chip OSA, the cascaded ring architecture serves as a wavelength filter and only light at wavelengths with identical peaks can be transmitted. Each combined FSR corresponds to one such channel. Illustration the functionality of the OSA, then, the transmitted power is proportional to the input power at the filtered wavelength. The integrated heater of each cascaded microring can be tuned to continuously shift the channel wavelength via adjusting the ring's resonant frequency. In this case, the channel spacing is only limited by the minimum step that the resonances can be tuned. The transmitted power seen at the OSA output is an indication of the energy level at specific channel wavelengths.

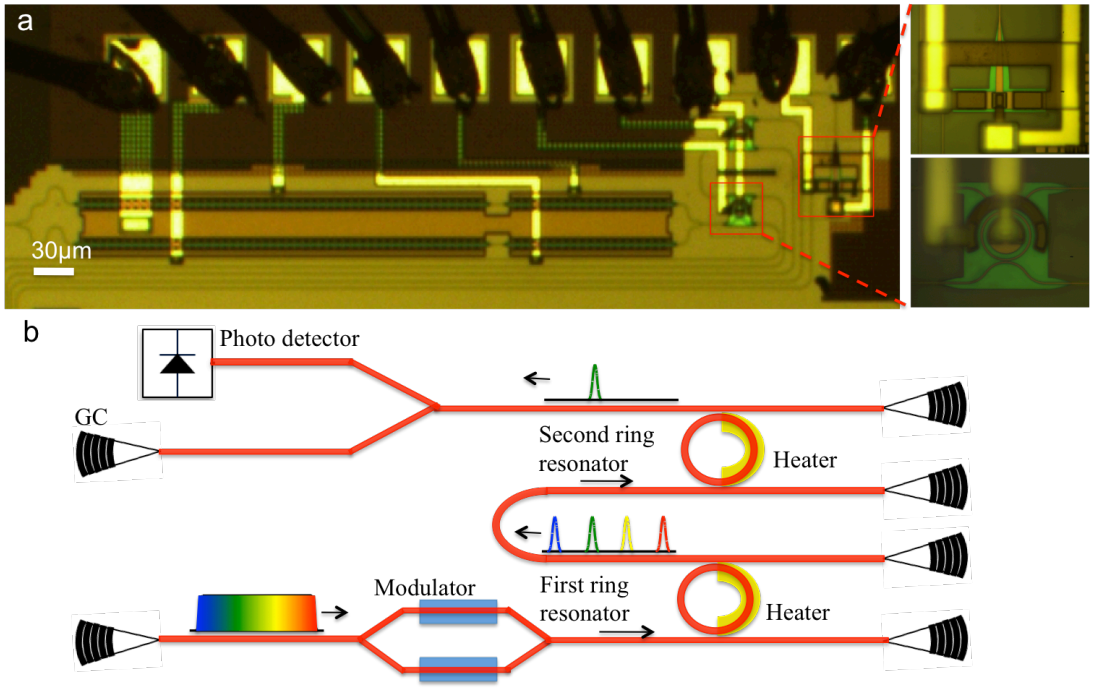

Figure 5.1 | SEM images and band diagram of the photonic crystal. a, Microscope image of the on-chip OSA. Zoomed in images show the germanium photodetector (top) and the first micro-ring resonator with the integrated heater (bottom). **b**, An illustration of the on-chip OSA device. GC: grating coupler.

The on-chip OSA is fabricated using a Silicon-on-Insulator (SOI) wafer with a 220 nm device layer. The image of the integrated device is shown in Figure 5.1(a). Light is coupled in and out of the circuit through grating couplers (not shown in the image). The grating couplers have a silicon-etch of 60 nm to define the gratings, which are arranged in a non-uniform pattern to increase coupling. The insertion loss is about 3.1 dB at 1550 nm and the 1.5 dB bandwidth is 50 nm [16]. The built-in traveling-wave MZM modulates the input light for a phase sensitive detection, which will extract signal from the environmental noise. The modulator is constructed, based on a lateral p-n junction waveguide with coplanar metal strips. The modulator length is 1 mm, while each arm has an independent Ground-Signal (GS) transmission line drive [17]. Two ring resonators with different optical roundtrip length are cascaded by 1.2 μm-wide ridge waveguide, which has a propagation loss of 0.27±0.06 dB/cm. The radii of the two ring resonators are 12.1 μm and 11.8 μm respectively. Integrated heaters are placed on top of the micro-rings. Light transmits through the two cascaded ring filters and then is received by an evanescently coupled Germanium photo-detector with a length of 11 um. The p-n junction is defined by an n-type implant in Germanium and a p-implant in silicon directly below the Germanium. Cross-wafer testing measured an average responsivity of 0.74±0.13 A/W [18]. Zoom-in images in Figure 5.1(a) show the photodetector (top) and one of the ring resonators (bottom) with its heater. There are ten electronic pads, all of which have been wire-bonded to a Pin Grid Array (PGA) package in order to maintain a stable contact resistance. The total footprint of the integrated device is ~ 1.5 mm^2. Figure 5.1(b) is a schematic illustration of the on-chip OSA. Both

rings have unused waveguide input and output ports serving as the test port to measure the spectrum of each ring separately.

5.3 Characterization and function demonstration

5.3.1 Experimental setup

The experimental setup diagram is shown in Figure 5.2. A tunable laser (Ando Q1234, λ = 1520 nm−1600 nm) is used as the light source. The polarization state of the input light is optimized by a polarization controller (PC). Light is coupled into grating couplers using an x-port fiber array. The transmission is monitored by a photodetector (Thorlabs PPA20CS). Two DC power supplies (Agilent E3633A, 0-12 V, minimum step size 1 mV) are employed to change the heater voltages and tune the resonant frequency. Another DC power supply (Agilent E3620A) is adopted to adjust the bias of the on-chip modulator. The spectrum of a micro-ring cavity is used as the reference spectrum to demonstrate the functionality of the on-chip OSA. The light source used here is a broadband source (JDS Uniphase). The reference signal is amplified by an erbium-doped fiber amplifier (EDFA) before sending to the on-chip OSA. The input light is modulated by a 50 kHz sinusoidal signal generated by a signal generator (Rhode&Schwarz). The same signal is also sent to the lock-in amplifier (Stanford Research System) as a reference signal. The electrical signal from the on-chip Germanium detector mixes with the reference signal in the lock-in amplifier, and the output signal is collected by a data acquisition (DAQ) board in the computer. The optical spectrum from the on-chip OSA is

compared with a commercial OSA (Yokogawa AQ6375).

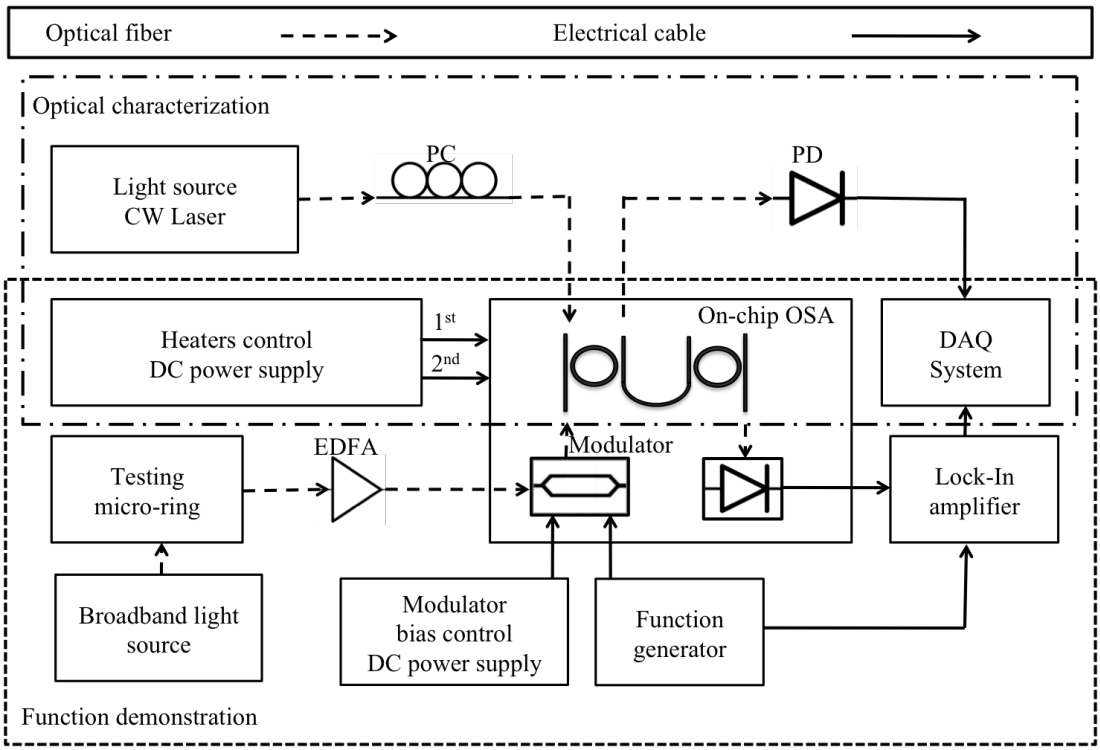

Figure 5.2 | Block diagram of the experimental setup. The on-chip OSA box represents the on-chip OSA system. The optical characterization box represents the setup used to measure optical spectrum of each ring resonators. A tunable laser and a photo-detector are used. DC power supplies control the integrated heaters voltages. The function demonstration box represents the setup used to test the functionality of the system. A testing signal is generated from a broadband source and a micro-ring resonator. The optical signal is amplified by the EDFA before it is sent to the on-chip OSA. The function generator connects to the on-chip modulator and the detector sends signal to the lock-in amplifier.

5.3.2 Function demonstration

Figure 5.3(a) shows the periodic optical frequency responses of the first and second ring resonators from 1530 nm to 1600 nm at passive state. The FSR of the first and second ring is 12.46 nm and 11.05 nm respectively. The quality factor of the resonances of the two rings are $Q_1 = 6.6\times10^3$ and $Q_2 = 6.8\times10^3$ from Lorentzian fit as shown in Figure 5.3(b) and (c).

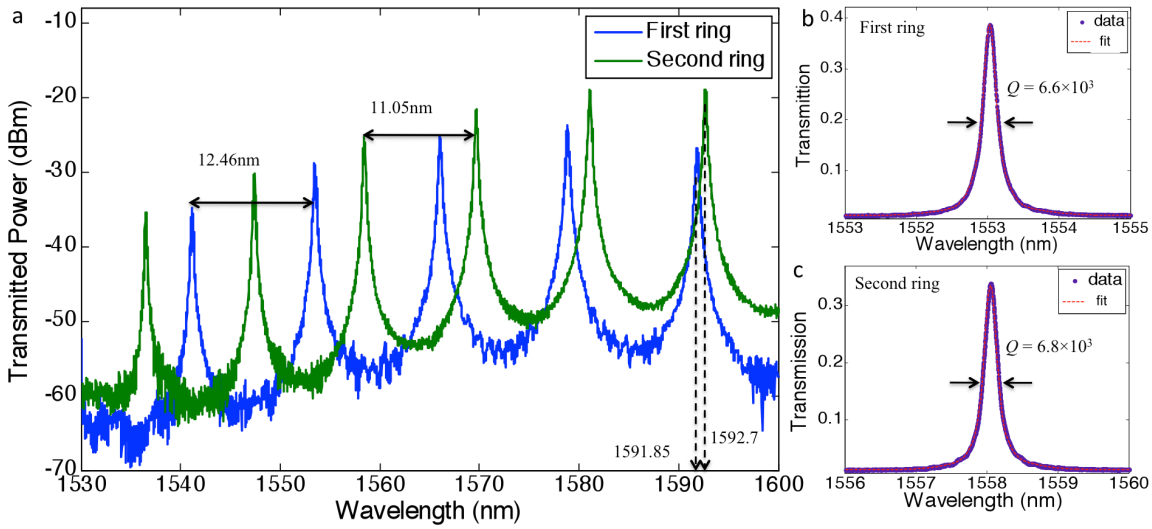

Figure 5.3 | Optical spectrum of each single ring. a, The optical spectrum of the first (blue line) and the second (green line) ring resonator. The FSR of the first ring is 12.46 nm and the FSR of the second ring is 11.05 nm. **b,** Lorentzian fit of one of the first ring's peaks. Optical qualify factor is $Q = 6.6\times10^3$. **c,** Lorentzian fit of one of the first ring's peaks. Optical qualify factor is $Q = 6.8\times10^3$.

Controlling the resonances precisely is crucial for realizing the spectrometer. Therefore, we first scanned the optical spectra of each ring with different voltages applied on the heaters. For the on-chip OSA, it was determined that a step size of 0.02 V is about a wavelength shift of 0.02 nm. For comparison purposes, then, the optical spectrum acquired by the commercial OSA was set to a resolution size of 0.02 nm. Then, a voltage scan of 0 V to 9.6 V, with a step of 0.02 V, was applied to the integrated heater. With this voltage scan it is shown that the tuning range of the resonant frequency is a little larger than its FSR.

Figure 5.4(a) and 5.4(b) are the 2D spectra scans of the first ring and the second ring. For the first ring, the resonance shift is about 12.5 nm, larger than its FSR of 12.46 nm when the voltage is adjusted from 0 V to 9.6 V. This shows that wavelengths in the range of 1530 nm to 1595 nm have a corresponding heater voltage value v_1 to tune the first ring's resonance to match the desired wavelength. Similarly, there will be a heater voltage value v_2, from within the range of 0 V to 9.6 V, which can exact the second ring's resonance to that of the same wavelength. From the Vernier effect, if we set the voltages as v_1 and v_2, there will only be a single peak that is transmitted through the two cascaded ring filters. Figure 5.4(c) shows the Vernier effect of the system. The applied heater voltages which garnered similar peak values are found to be $v_1 = 8.45$ V and $v_2 = 5.12$ V. Only one peak appears in the spectrum from 1530 nm to 1580 nm at 1565 nm, which is what we show in Figure 5.4(c). The FWHM of the peak is 0.17 nm, which determines the theoretical resolution limit of the on-chip OSA. One such voltage pair (v1, v2) determines a wavelength channel. The inserted plot in Figure 5.4(c) shows the

spectra of other 150 channels with wavelength from 1525 nm to 1580 nm. For this experiment, we identified 3700 voltage pairs, effectively defining 3700 channels. The wavelength range of these channels is from 1521 nm to 1595 nm. As mentioned previously, the channel spacing is 0.02 nm, which is decided by the spectra scan's wavelength resolution. Figure 5.4(d) shows the wavelength and heater voltage (v1, v2) mappings of all the channels.

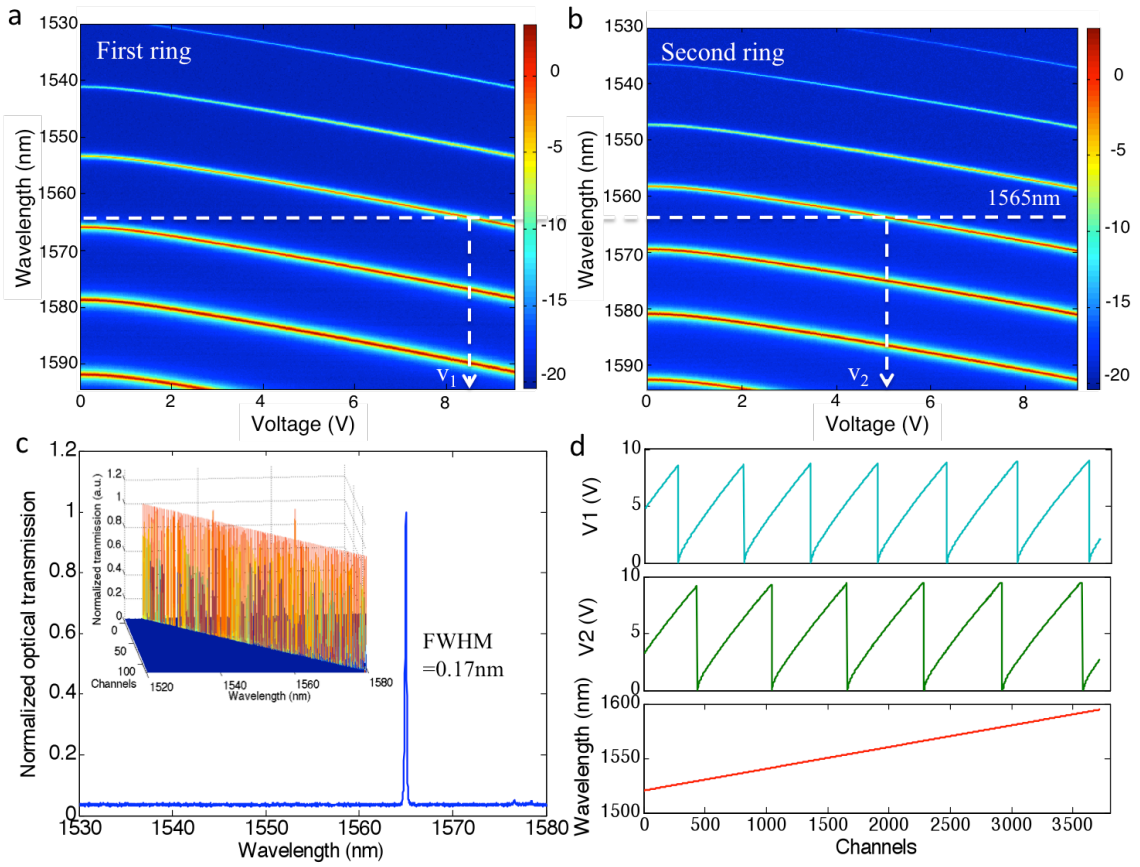

Figure 5.4 | The Vernier effect and spectrometer channels. a-b Optical spectra scans of the first and second ring with different voltages applied on the heater from 0 V to 9.6 V with a step of 20 mV. The wavelength of the resonator shifted about 12.5 nm in the voltage range, a little larger than its FSR. The optical spectrum resolution is 0.02 nm. The color bar represents the power in dBm. **c,** Spectrum of a channel at 1565 nm. The FWHM of the peak is 0.17 nm from Lorentzian fit. Inserted is an illustration of 150 such channels. Each channel corresponds to a voltage pair (V_1, V_2). **d,** The heater voltages (V_1, V_2) and wavelength of the total 3700 channels.

To demonstrate the functionality of the on-chip OSA, a reference spectrum was generated with a broadband light source, a passive micro-ring for reference and an EDFA. A commercial OSA was employed for comparison. The reference spectrum was measured by both the on-chip OSA and the commercial OSA. The results are shown in Figure 5.5. There are three major peaks of the reference spectrum located at 1529.56 nm, 1542.43 nm and 1555.56 nm. The spectrum was first measured by the on-chip OSA with only 370 channels and a channel spacing of 0.2 nm as shown in Figure 5.5(a-b). The wavelength range of the spectrum is from 1521 nm to 1595 nm and the sampling point is 1. For comparison, the reference spectrum was also measured by the on-chip OSA with 3700 channels, channel spacing of 0.02 nm and sampling point of 20. The result is shown in Figure 5.5(c-f). The spectral shape from the on-chip OSA agrees very well with the spectrum measured with commercial OSA. Figure 5.5(b) and figure 5.5(d) are the zoomed-in images taken of the second peak of the two spectra. By comparing the two curves in figure 5.5(b) and (d), the locations of their peaks differ by around 0.2 nm. Figure 5.5(d) fits better with the reference with the peak shifts about 0.03 nm. As expected, smaller channel spacing and larger sampling points will yield higher spectral accuracy. Figure 5.5(e-f) are the log plot of Figure 5.5(c-d) for finer granularity.

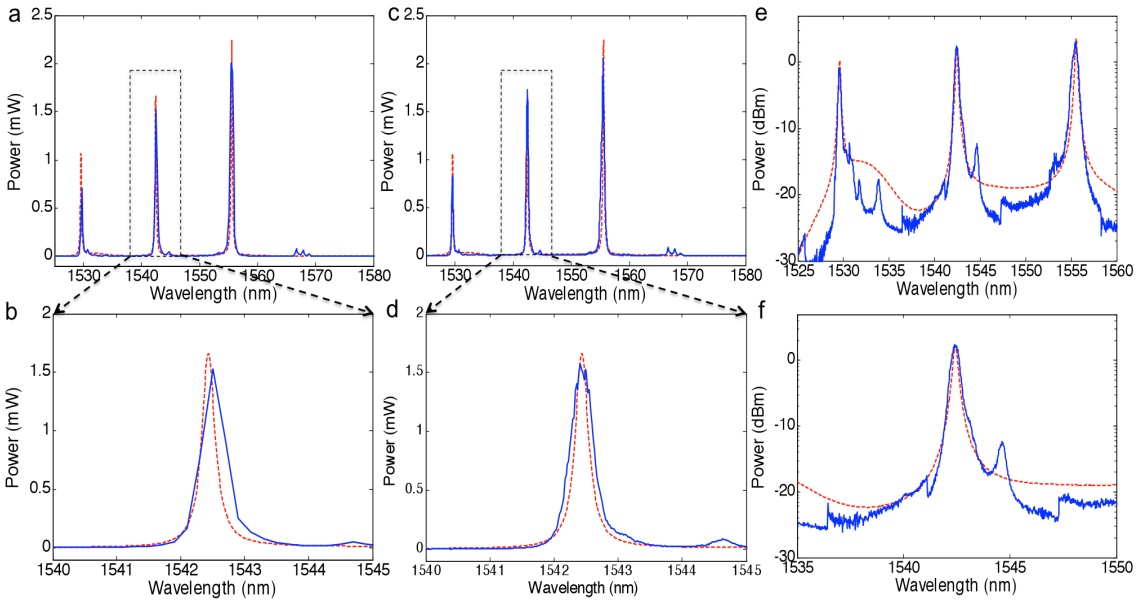

Figure 5.5 | Function demonstration. a, c, Optical spectrum measured with the on-chip OSA system. The reference spectrum is generated from a micro-ring with three major peaks at 1529.56 nm, 1542.43 nm and 1555.56 nm. The red dashed curve is the measurement from the commercial OSA. **a**, Spectrum measured using 370 channels, with channel spacing of 0.2 nm. **c**, Spectrum measured using 3700 channels, with channel spacing of 0.02 nm. (**b**) (**d**) is the zoomed in image of the second peak in (**a**) (**c**), respectively. (**e**) and (**f**) are the logarithmic plots of (**c**) and (**d**).

Both the wavelength and the power level of the on-chip OSA output signal have been calibrated. The wavelength of each channel is obtained from the 2D spectra scans. To test the wavelength accuracy, as illustrated in Figure 5.6(a), laser light at wavelength of 1535 nm, 1550 nm and 1575 nm was sent into the on-chip OSA. Its purpose was to serve as a calibration signal. The result shows that for all three spectra, the wavelength shift of the peak is less than 0.2 nm. A broadband light source (1520 nm-1590 nm) is employed to calibrate the power level and convert the output voltage from the lock-in amplifier to optical power. The light source is measured with both the commercial OSA and the on-chip OSA. Both spectra are shown in Figure 5.6(b), with the y-axes of the spectra corresponding to either the optical power as recorded from the commercial OSA (left axis) or the voltage value from the on-chip OSA (right axis). The ratio of the optical energy in the unit of milliwatt to the lock-in amplifier output in the unit of volt has been calculated. This number is not constant across different wavelengths due to the wavelength dependence of the photodetector, grating coupler, and waveguide design. Therefore, the ratio is also a function of wavelength, which we record to serve as a power calibration function. This function is used as part of the on-chip OSA functionality to calibrate the power level of the spectra. An example of a calibrated spectrum is shown in the broadband source illustrated as a blue curve in Figure 5.6(b).

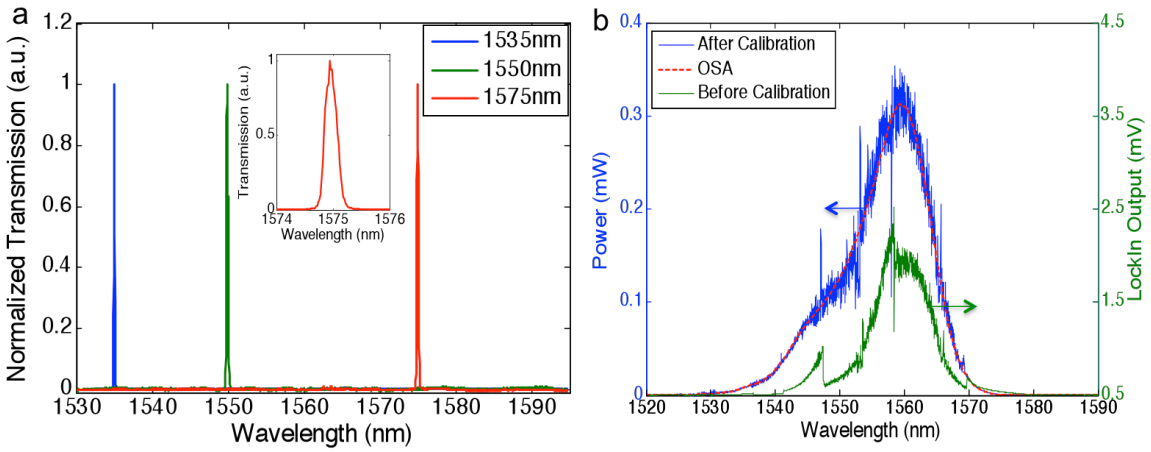

Figure 5.6 | Spectrum wavelength and power calibration. a, Wavelength accuracy test. Measured optical spectrum of monochromic light at wavelength of 1535 nm, 1550 nm and 1570 nm. Wavelength shifts of the three peaks are all less then 0.2 nm. Insert figure is the zoom in of the peak at 1569.85 nm. **b**, Power level calibration. The input signal is the broadband source. The green curve is the output in mV, measured from the lock-in amplifier. The red dash line is measured with the conventional OSA. The blue curve is the result from the on-chip OSA after calibration.

The on-chip modulator is a silicon traveling-wave MZM. By using the on-chip modulator, a phase sensitive detection with the lock-in amplifier is commonly implemented in communication systems for detecting small signals in the presence of overwhelming noise, thus minimizing the effect of electronic noise on the signal. In order to demonstrate the advantage of phase sensitive detection, we compared the optical spectrum measured directly from the on-chip detector to the one measured from the lock-in amplifier. The reference spectrum from the micro-ring resonator was used, but for the purpose of brevity, we will only focus on the third peak here. We first employed a source-meter (Keithley 2410) and the output current signal was the photodetector. The current output was converted to optical power using the same power calibration method as described above. Figure 5.7 shows that the measured spectrum deviates from the reference spectrum of the commercial OSA, and the noise level increases from -13 dBm to -5 dBm compared with the result acquired with the phase sensitive detection method.

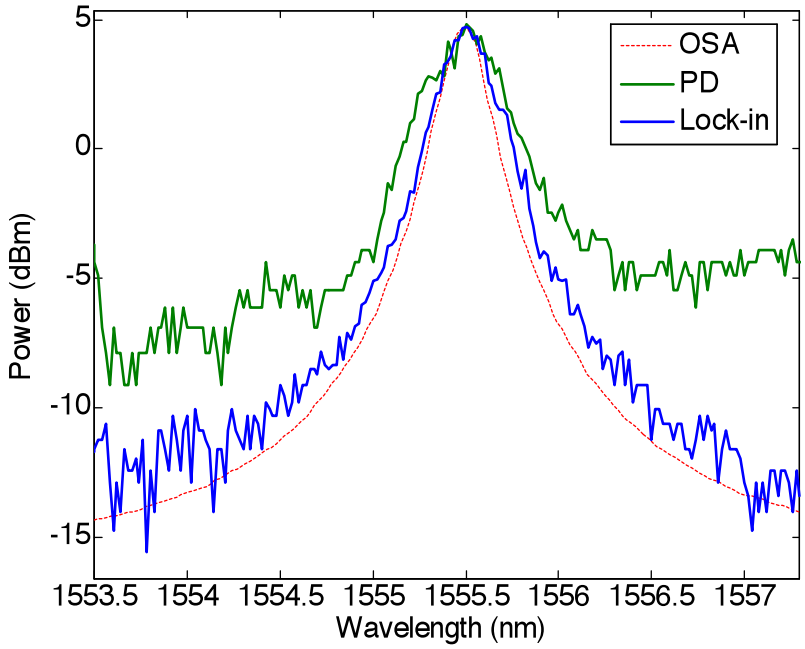

Figure 5.7 | Comparison of the spectrum noise level. The red dashed curve is measured from conventional OSA as a reference. For the green curve, the input light is not modulated and the output signal is collected directly from the on-chip Ge detector. The blue curve is obtained from a phase sensitive detection by using the on-chip modulator and a lock-in amplifier.

5.3.3 OSA specifications

The performance of an OSA is usually represented and limited by specifications such as measurement range, sensitivity, and resolution, which will be discussed in this section. The measurement range of our on-chip OSA system is given by the Vernier effect, which can be derived to be 11.05 nm times the integral part of [11.05 nm / (12.46 nm - 11.05 nm)], equivalent to 77.35 nm. To better quantify the performance of the on-chip OSA, the sensitivity of the OSA is attained. Sensitivity is defined as the minimum detectable signal or, more specifically, six times the root mean square (RMS) noise level of the instrument [19]. Thus, the sensitivity of the on-chip OSA is identified by gradually decreasing the signal level, until it is six times the RMS noise level. Figure 5.8(a) shows the displays of measured results of four signals with declining power levels. The curve with the lowest peak's amplitude is equal to the sensitivity of the on-chip OSA, which is -31.2 dBm. It can be noted that the sensitivity is limited by the dark current of the Ge photodetector and the insertion loss of the whole system including the loss from the grating couplers, waveguides, the modulator and the directional coupler. By optimizing the system design, for example through minimizing the length of the waveguides, the sensitivity can be improved. The ability of an OSA to display two signals closely spaced in the wavelength domain as two distinct responses is determined by the wavelength resolution. Wavelength resolution is, in turn, determined by the bandwidth of the optical filter. As shown in figure 5.4(c), the FWHM is 0.17 nm. An experiment method to

corroborate this conclusion is to measure the FWHM of a monochromatic light. Figure 5.8(b) shows the FWHM measured as 0.22 nm, 0.05 nm larger than expected. The result makes sense since 0.17 nm is the most optimal condition. For some measurements, the width of the filter is not the only concern. Filter shape (specified in terms of dynamic range) is also important. Dynamic range is commonly specified at 1 nm offsets from the main response [20]. Figure 5.8(c) illustrates that the on-chip OSA has a dynamic range of -31.7 dB at 1.0 nm, indicating that the OSA's response to a purely monochromatic signal will be -31.7 dBm or less at offsets of 1 nm and greater.

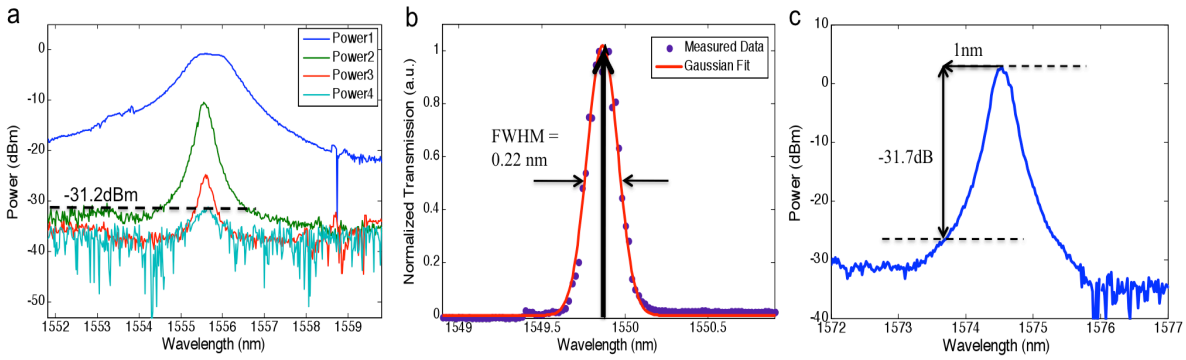

Figure 5.8 | Specification of the on-chip OSA. a, Sensitivity of the on-chip OSA. Input light power decreases from signal 1 to signal 4. The sensitivity of the system is -31.2 dBm. **b**, The resolution of the On-chip OSA measured here is 0.22 nm. **c**, Dynamic range for 1nm offset is -31.7 dB.

5.4 Discussion

In this chapter, we have experimentally demonstrated a compact broadband on-chip OSA based on the Vernier effect of two cascaded ring resonators. We showed that the FSR of the system has been extended to 77 nm due to the Vernier effect. Since the channel count is not limited by the optical elements, we have demonstrated support of up to 3700 channels, with channel spacing of 0.02 nm. To the best of our knowledge, this is the highest number of channels and smallest channel spacing for such small device integration size. We also showed that the on-chip OSA could measure an optical spectrum with a resolution of 0.22 nm and a wavelength range of 70 nm in the communication band. The sensitivity reaches -31.2 dBm by using the phase sensitive detection. The device including the on-chip photodetector and modulator is integrated in a 1.5 mm^2 area. If we only consider the area of the microrings and the photodetector, the footprint of the device is even less than 0.5 mm^2. We believe that the results presented here can be used in photonic integrated circuits (PICs) and optical communication systems.

Table 5. 1. Comparison of state-of-the-art microspectrometers

	Resolution (nm)	Footprint	Wavelength range (nm)	Channel counts	Channel spacing (nm)	Sensitivity /Crosstalk
Microdonut array [7]	0.6	$1mm^2$	50 (1550-1600nm)	81	0.6	
Grating with tunable ring [4]	-	$< 2mm^2$	10 (1483-1493nm)	100	0.1	Crosstalk -10dB
PhC cavity array [8]	0.3	$\sim 100um^2$	10 (833-843nm)	9	~1	
Filter array [5]	1.7-3.8	$<1cm^2$	158 (722-880nm)	128	1.2	
On-chip OSA	0.22	$<1.5mm^2$	74 (1526-1600nm)	3700	0.02	Sensitivity -31.2dBm

Bibliography

[1] S. Janz, A. Balakrishnan, S. Charbonneau, P. Cheben, M. Cloutier, A. Delage, K. Dossou, L. Erickson, M. Gao, P. A. Krug, B. Lamontagne, M. Packirisamy, M. Pearson, and D. -X. Xu, Planar Waveguide Echelle Gratings in Silica-On-Silicon, *IEEE Photon. Technol. Lett.* 16(2), 503 (2004).

[2] Y. Tanaka, Y. Itoh, K. Aizawa, T. Kurokawa, and H. Tsuda, Optical Spectrum Analyzer Based on Arrayed Waveguide Grating for High-Speed Optical Communication Systems, *IEEE Photon. Technol. Lett*. 17(2), 432 (2005).

[3] J. Brouckaert, W. Bogaerts, S. Selvaraja, P. Dumon, R. Baets, and V. Thourhout, Planar Concave Grating Demultiplexer With High Reflective Bragg Reflector Facets, *IEEE Photon. Technol. Lett*. 20, 309 (2008).

[4] B. B. C. Kyotoku, L. Chen, and M. Lipson, Sub-nm resolution cavity enhanced microspectrometer, *Opt. Express* 18(1), 102–107 (2010).

[5] S.-W Wang, C. Xia, X. Chen, and W. Lu, M. Li and H. Wang, W. Zheng and T. Zhang, Concept of a high-resolution miniature spectrometer using an integrated filter array, *Opt. Lett.* 32, 632 (2007).

[6] R.G. DeCorby, N. Ponnampalam, E. Epp, T. Allen, J.N. McMullin, Chip-scale spectrometry based on tapered hollow Bragg waveguides, *Opt. Express* 17(19), 16632 (2009).

[7] Z. Xia, A. A. Eftekhar, M. Soltani, B. Momeni, Q. Li, M. Chamanzar, S. Yegnanarayanan, and A. Adibi, High resolution on-chip spectroscopy based on miniaturized microdonut resonators, *Opt. Express* 19(13), 12356 (2011).

[8] X. Gan, N. Pervez, I. Kymissis, F. Hatami, and D. Englund, A high-resolution spectrometer based on a compact planar two dimensional photonic crystal cavity array, *Appl. Phys. Lett.* 100(23), 231104 (2012).

[9] B. Momeni, E. S. Hosseini, M. Askari, M. Soltani, and A. Adibi, Integrated photonic crystal spectrometers for sensing applications, *Opt. Commun*. 282(15), 3168 (2009).

[10] A. C. Liapis, Z. Shi, and R. W. Boyd, Optimizing photonic crystal waveguides for on-chip spectroscopic applications, *Opt. Express* 21(8), 10160 (2013).

[11] B. Momeni, M. Chamanzar, E. S. Hosseini, M. Askari, M. Soltani, and A. Adibi, Strong angular dispersion using higher bands of planar silicon photonic crystals, *Opt. Express* 16(18), 14213 (2008).

[12] S. Suzuki, K. Oda, and Y. Hibino, Integrated-Optic Double-Ring Resonators with a Wide Free Spectral Range of 100 GHz, *J. Lightwave Technol* 13(8), 1766 (1995).

[13] T. Claes, W. Bogaerts, and P. Bienstman, Experimental characterization of a silicon photonic biosensor consisting of two cascaded ring resonators based on the Vernier-effect and introduction of a curve fitting method for an improved detection limit, *Opt. Express* 18(22), 22747 (2010).

[14] K. Padmaraju, D. F. Logan, X. Zhu, J. J. Ackert, A. P. Knights and K. Bergman, Integrated thermal stabilization of a microring modulator, *Opt. Express* 21(12), 14342 (2013).

[15] C. K. Madsen and J. H. Zhao, Optical Filter Design and Analysis: A Signal Processing Approach, Wiley, New York, NY (1999).

[16] A. Novack, Y. Liu, R. Ding, M. Gould, T. Baehr-Jones, Q. Li, Y. Yang, Y. Ma, Y. Zhang, K. Padmaraju, K. Bergmen, A. E.-J. Lim, G.-Q. Lo and M. Hochberg, A 30 GHz Silicon Photonic Platform, *IEEE 10th International Conference on Group IV Photonics*, 7–8 (IEEE, Seoul, S. Korea, 2013).

[17] T. Baehr-Jones, R. Ding, Y. Liu, A. Ayazi, T. Pinguet, N. C. Harris, M. Streshinsky, P. Lee, Y. Zhang, A. Eu-Jin Lim, T.-Y. Liow, S. H-G Teo, G.-Q. Lo, and M. Hochberg, Ultralow drive voltage silicon traveling-wave modulator, *Opt. Express* 20(11), 12014 (2012).

[18] Y. Zhang, S. Yang, Y. Yang, M. Gould, N. Ophir, A. E.-J Lim, G.-Q Lo, P. Magill, K. Bergman, T. Baehr-Jones, and M. Hochberg, A high-responsivity photodetector absent metal-germanium direct contact, *Opt. Express* 22(9), 11367 (2014).

[19] Optical Spectrum Analysis Basics, Agilent Technologyies Application Note 1550-4

[20] R. Hui, M. O'Sullivan, Fiber Optic Measurement Techniques, Academic Press, Waltham, Massachusetts (2009).

Chapter 6

Future outlook

6.1 Future applications

As discussed in Chapter 4, the high sensitivity of the optical readout allows new integrated optomechanical platforms for acceleration sensing. Optomechanical cooling in combination with on-chip mechanical sensors has also been suggested to provide a reduction in thermal noise for the optical readout [1]. The combination with optomechanical preparation of squeezed mechanical states could lead to a new mechanical sensing technology with unprecedented levels of sensitivity due to the reduced position variance of the readout device.

Besides the sensing applications, other applications of cavity optomechanics have also been reported during the part few years. In laser sciences, these include tunable optical filters, based on the fact that optomechanical coupling can lead to extreme tuning of the mechanical frequency up to several octaves, as well as optomechanical implementations of laser stabilization [2]. Embedded optomechanical cavities have been shown to serve as an all-optical memory element [3, 4], or have been proposed as a new technology for single-photon detection [5].

From a quantum information processing perspective cavity optomechanics offers a new architecture for coherent light-matter interfaces in a solid-state implementation. Mechanical motion can serve as a universal transducer to mediate long-range interactions between stationary quantum systems. The specific trait of optomechanical systems is the interconversion between stationary qubits and flying qubits, which constitutes one of the main elements of long-distance quantum communication and a

future quantum internet [6-7].

Bibliography

[1] M. Winger, T. D. Blasius, T. P. Mayer Alegre, A. H. Safavi-Naeini, S. Meenehan, J. Cohen, S. Stobbe, and O. Painter, A chip-scale integrated cavity-electro-optomechanics platform, *Opt. Express* 19, 24905 (2011).

[2] T. P. M. Alegre, R. Perahia, and O. Painter, Optomechanical zipper cavity lasers: theoretical analysis of tuning range and stability, *Opt. Express* 18, 7872 (2010).

[3] M. Bagheri, M. Poot, M. Li, W. P. H. Pernice and H. X. Tang, Dynamic manipulation of nanomechanical resonators in the high-amplitude regime and non-volatile mechanical memory operation, *Nature Nanotechnology* 6, 726 (2011).

[4] G. D. Cole and M. Aspelmeyer, Cavity optomechanics: Mechanical memory sees the light, *Nature Nanotechnology* 6, 690 (2011).

[5] M. Ludwig, A. H. Safavi-Naeini, O. Painter, and Florian Marquardt, Enhanced Quantum Nonlinearities in a Two-Mode Optomechanical System, *Phys. Rev. Lett.* 109, 063601 (2012).

[6] H. J. Kimble, The quantum internet, *nature* (london) 453, 1023 (2008).

[7] M. Aspelmeyer, T. J. Kippenberg, F. Marquardt, Cavity optomechanics: nano- and micromechanical resonators interacting with light, Springer (2014).